THESIS

as partial fulfillment of the requirements of the
Degree of Master of Science
In
Mechanical Engineering

Development of digital holographic vibrometry methods for determination of mechanical properties of bioengineered tissues

Submitted by:

_____
Colin Hiscox

Submitted to:

_____
Professor Cosme Furlong, Major Advisor

_____
Professor Kristen Billiar, Thesis Committee

_____
Professor Dmitry Korkin, Thesis Committee

_____
Professor Zhu Mao, Thesis Committee

_____
Professor Yihao Zheng, Graduate Committee Representative

Mechanical Engineering Department
Worcester Polytechnic Institute
Worcester, MA 01609-2280

April 20, 2022

Abstract

Modern development of bioengineered tissues for therapeutic applications calls for the advancement of methodologies to increase the efficiency of the steps used in large-scale manufacturing. One of the steps in the manufacturing processes that requires further development is quality control where determination of physical properties is currently slow, labor intensive, destructive, and requiring improved precision.

This Thesis describes the creation, validation, and preliminary application of a digital holographic vibrometry (DHV) sensor to measure the mechanical properties of tissues. This sensor uses acoustic energy from a sound source to induce vibrations in tissue samples together with high-resolution digital holography methods. Full-field-of-view, real-time modes of vibration of samples are obtained with micrometer and nanometer spatial and displacement measurement resolutions, respectively. The mode shapes and the frequencies at which natural modes of vibration occur are correlated to the mechanical properties of tissue samples. The tissue used in this Thesis is Apligraf biofabricated skin, manufactured by Organogenesis Inc. Using Apligraf as an initial application, experimental modal analyses are conducted together with Finite Element (FE) simulations to train a machine learning algorithm. This Thesis demonstrates the capabilities of such approach to recover mechanical properties of intact packaged tissues noninvasively. Validation is supplemented by application of optical coherence tomography (OCT) and nanoindentation measurements.

Further, this Thesis discusses the application of the sensor to a string model. This serves as a proof of concept of the applicability of the sensor to noninvasively investigate bioengineered ligaments as well as potentially other bioengineered tissues. This Thesis finds the presented methodologies to successfully noninvasively measure vibrations in the two tissue models. However, complexities in the packaging make it difficult to identify mechanical properties from these vibrations using standard

analytical methods. As such a machine learning approach is under present development to interpret the collected data and relate vibration shape and frequency to the mechanical properties of the tissue. Future developments of the methodologies can enable the realization of instrumentation and algorithms for quality control of bioengineered tissues in large-scale manufacturing settings.

Acknowledgments

I would like to thank Professor Cosme Furlong for his support and guidance during this project. I would also like to thank the members of the Center for Holographic Studies and Laser micro-mechaTronics (CHSLT), particularly Mr. Daniel Ruiz-Cadalso and Dr. Haimi Tang. I am also thankful to Professor Kristen Billiar and Professor Dmitry Korkin for their guidance in this research and Juanyong Li and Ziyang Gao for their assistance in various parts of this project.

I am thankful to Dr. Adriana Hera, Mr. Peter Hefti, and Mr. Lucas Tendela for advice in creating a working method.

This research is funded by the NSF (CMMI 1761432) and BioFabUSA (T0137). I would like to thank these organizations as well as WPI and the CHSLT for funding. I would also like to thank Kate Faria and Organogenesis for supplying the Apligraf used in this project.

Table of Contents

List of Figures

List of tables

Nomenclature

AFM	Atomic Force Microscopy
AOM	Acousto-Optic Modulator
APFP	Air Puff Fringe Projection
Apligraf	A tissue created by Organogenesis
CCD	Charge Coupled Device
CHSLT	Center for Holographic Studies and Laser micro-mechaTronics
CPT	Classical Plate Theory
DHV	Digital Holographic Vibrometry
DHI	Digital Holographic Interferometry
EM	Extracellular Matrix
FE	Finite element
FEA	Finite Element Applications
FFT	Fast-Fourier Transform
Laserview	a program used by the CHSLT to coordinate multiple controlling devices
LDV	Laser Doppler Vibrometry
LVvid	a video file type
ML	Machine learning
MLP	Machine Learning Program
MRE	Magnetic Resonance Elastography
OCE	Optical Coherence Elastography
OCT	Optical Coherence Tomography
PS	Phase Shifting
PWV	Pulse Wave Velocity
QC	Quality Control
SAM	Scanning Acoustic Microscopy
UE	Ultrasonic Elastography

Objectives

The objective of this Thesis is to develop an optical tool and methodology to noninvasively and nondestructively measure the mechanical properties of bioengineered tissues. This requires the development of digital holographic vibrometry methodologies that can measure in full field-of-view and in real time the dynamic behavior of a tissue with intact-packaging. This behavior is related to the mechanical properties and the quality of the tissue. To extract the mechanical properties, finite element models are developed to train a neural network, which will be used in the future with experimental measurements to characterize the quality of tissues.

Impact

This Thesis discusses the creation of a holographic sensor. This sensor can be used to noninvasively measure the vibration of bioengineered tissues. This has an important impact on the quality control (QC) process of biomanufacturing. Current measurement methods such as uniaxial tensile tests or nanoindentation are invasive and destructive and can introduce bacteria or other contaminants to the tissue. This sensor, however, can measure vibrations within the tissue's packaging, preserving the tissue's integrity and sterility.

These bioengineered tissues are widely used for therapeutic applications which heal wounds or damaged tissues. As this technology might increase the ability to measure every single tissue, it is possible it could result in fewer mechanical failures of tissues. This would result in an overall higher level of care for patients. Second, the potential for this technology to measure tissues noninvasively means it can be used to measure tissues that are still in the growth process. Such monitoring of mechanical properties during growth can indicate the effectiveness or efficiency of manufacturing processes, allowing for optimization or identification of problems in manufacturing steps. As this technology has the potential to streamline the QC process for testing mechanical integrity of individual tissues, it could decrease the time necessary for the QC step. This would make the tissues more accessible to the general population, increasing the number of people to whom bioengineered tissues are a viable alternative. Overall, this technology has the potential to increase the health benefits of bioengineered tissues, allowing them to heal more people for longer times.

1. Introduction

1.1. Problem statement

Modern advancements in the field of bioengineering have paved the way for a variety of therapeutic applications for artificial tissues. This requires an upscaling of manufacturing processes that necessitate improvements to the efficiency and large-scale application of present manufacturing processes. Part of the manufacturing process to which this is applies is the quality control (QC) step. Tissues destined for therapeutic applications require appropriate QC to ensure they will not fail or otherwise harm a patient. This requires a number of QC tests, with biological and chemical tests to establish viability [1] being well established. Equally important, however, is the mechanical integrity of the tissue. This is connected to its ability to function and mimic the native tissue [2] and is intricately connected to the growth of the tissue and the manufacturing processes used to fabricate the tissue. Problems within manufacturing steps can harm the mechanical integrity or properties of the tissue but only measuring a tissue at the end of its growth phase does no identify such steps. Current tests to determine mechanical properties are either too slow, too destructive, or only provide information about a certain point instead of the full sample. These tests additionally tend to be specialized with specific sample preparation performed in small batches, adding more operator time requirement. As such they can not be effectively used within the growth phase of the manufacturing process without degrading the tissue.

There is thus a need for noninvasive and nondestructive methodologies to determine the mechanical properties of bioengineered tissues. A process that can measure the full field-of-view of a tissue quickly and with low operator time could help the QC step of manufacturing of bioengineered tissues. Of special value is a methodology that can measure properties in mid-fabrication steps to establish future feedback control.

1.2. Project scope

This Thesis is about the development of non-invasive optical methodologies to measure the mechanical properties of bioengineered tissues. Stroboscopic digital holography is combined with vibration techniques to create a digital holographic vibrometry (DHV) methodology. The vibrational modes of a tissue with applied acoustic energy are measured to be given to a supervised machine learning (ML) algorithm to classify these measurements and eventually output predicted mechanical properties. This Thesis discusses the creation of a finite element (FE) model and the training of the ML algorithm with the model for an application on the bioengineered skin tissue, Apligraf [3]. It discusses several complications and limitations of this technique as well as advantages and capabilities as applied to Apligraf, and a proof-of-concept for ligaments. It additionally analyzes the alternative method of Air Puffing Fringe Projection and high-speed holographic imaging of high-frequency wave propagation for the potential as an alternative, minimally invasive method.

2. Background

This Thesis makes use of holographic techniques and machine learning to model and measure biological tissues. For this purpose, it is important to have a solid understanding of these bioengineered tissues and the models used to estimate their properties. As non-invasive measurement is of critical importance for quality control in manufacturing of bioengineered tissues destined for therapeutic applications, this Section also discusses a brief background on noninvasive measurement.

2.1. Bioengineered tissues

Bioengineered tissues are biological tissues created or modified for a specific application. In modern medicine, there is a large push to create more tissues for therapeutic applications [4] in which these are used to heal human tissues. This comes with challenges starting at the beginning with the creation of an effective and functional tissue and going all the way to whether the tissue will be rejected by the patient's immune system. Such tissues can include comparatively simple skin tissues for applications such as ulcers or burn wounds or slightly more complex structures such as blood vessels. The general goal of many researchers in the field is to develop tissues complicated enough to operate within organs, but current successes have been most concentrated in the simpler tissues [5].

The first component of tissue manufacturing is cell sourcing. Bioengineered tissues are a collection of cells and their extracellular matrix, so finding an appropriate cell type to compose the tissue is important. Cells can be taken from the patient, or from a donor. Once the correct cell type is found, they are seeded into a desired location and grown. The cells interact with nearby cells to build an extracellular matrix (ECM) and develop connectivity, creating a tissue. Depending on the

cell type, different components of ECM may be formed around the tissue, and for some applications the ECM can even be taken from a separate source or replaced with a manufactured scaffold.

The way that a bioengineered tissue is created has a significant effect on its mechanical properties and thus its functionality [6]. The most common production method is cell-seeded scaffolding [7]. In this method a scaffold is created onto which cells can grow. The scaffold itself can be produced by chemical means for a porous material like tissue-destined hydrogels, or physical means like with 3D printing. Figure 1 shows an example of a scaffold with pores, into which stem cells are placed to grow into a tissue. The properties of this scaffold in turn affect the differentiation of the cells.

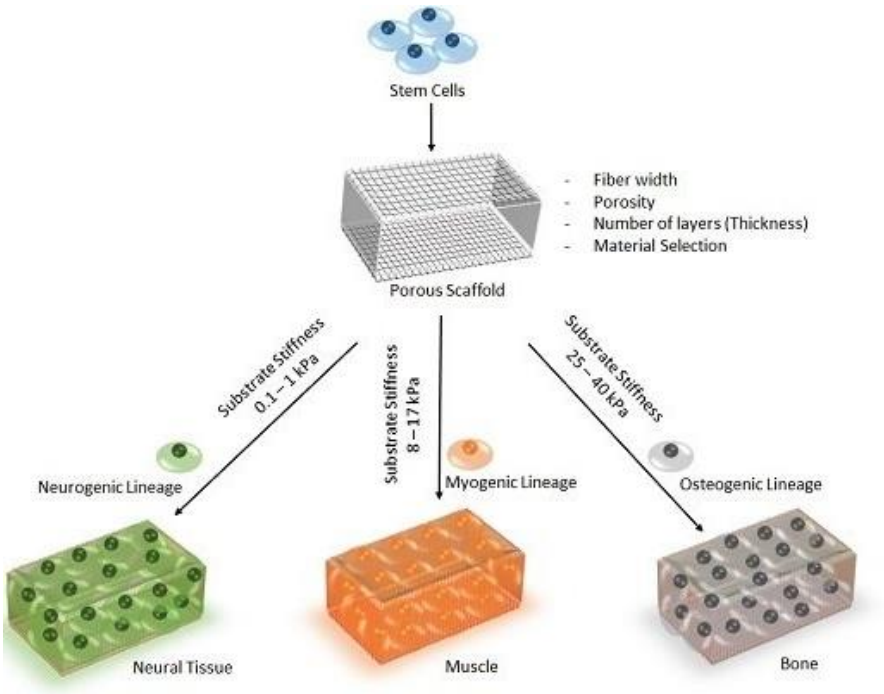

Fig. 1 Tissue development based off of scaffold properties. The scaffold is used to provide a structure to cells as a tissue forms, but its mechanical properties can help determine how the tissue grows. Figure reproduced from Vijayavenkataraman et al (2017) (CC BY) [8]

Any physical manufacturing process that creates a biocompatible and resorbable surface on which the cells can attach can create an appropriate scaffold and it is possible for 3D printed structures to serve as a scaffold. The critical component that makes a scaffold as opposed to a simple growth substrate is the shape, in which the cells growing on the scaffold have already been physically pushed by the scaffold into the desired shape of the tissue. An example of this is a polylactide scaffold in a tube shape to create a blood vessel. Sometimes the material chosen, such as with polylactide, dissolves as the cells grow and create a more cohesive structure so that no scaffold is left in a final product. It is also common to use decellularized tissues as a scaffold. In this process a normal tissue is stripped of cells, leaving only the ECM behind as a scaffold. The source for the decellularized tissue is often decellularized animal or human tissue, such as from a bone.

The benefit of using decellularized tissues is that the scaffold has already formed in complex shapes appropriate for biological processes, it has a higher biocompatibility than xenografts, and it is sometimes much cheaper and easier to source. However, such scaffolds are not always preferable and there are several concerns: decellularization methods can likely weaken the mechanical properties of the tissue, the tissue might not degrade within a patient as quickly as is sought for artificial scaffolds, and in some cases long term biocompatibility has not yet been established [9].

A similar manufacturing method to cell-seeded scaffolding is bioprinting. This is a replication of the 3d printing process but with cells instead of plastics. Bioprinting allows for individual placement of cells or small groups of cells. The cells still need to be fed nutrients and allowed to grow to form a cohesive tissue so they must be placed onto a substrate or placed with the substrate as part of the bioprinters extrusion. This leads to laser-based printing, extrusion, or

inkjet printing methods [10]. Some illustrations of such bioprinting processes can be seen reproduced in Fig. 2. These cell and substrate systems then have some sort of 3D shape, and mechanically act similarly to cell-scaffold systems. As the mechanical properties of the environment in which cells grow can affect the mechanical properties of the end-product tissue, the properties of the matrix used for bioprinting is important. The properties of this matrix and the matrix-cell ratio provide two areas that affect the tissue's properties and thus can be optimized by an advanced measurement method.

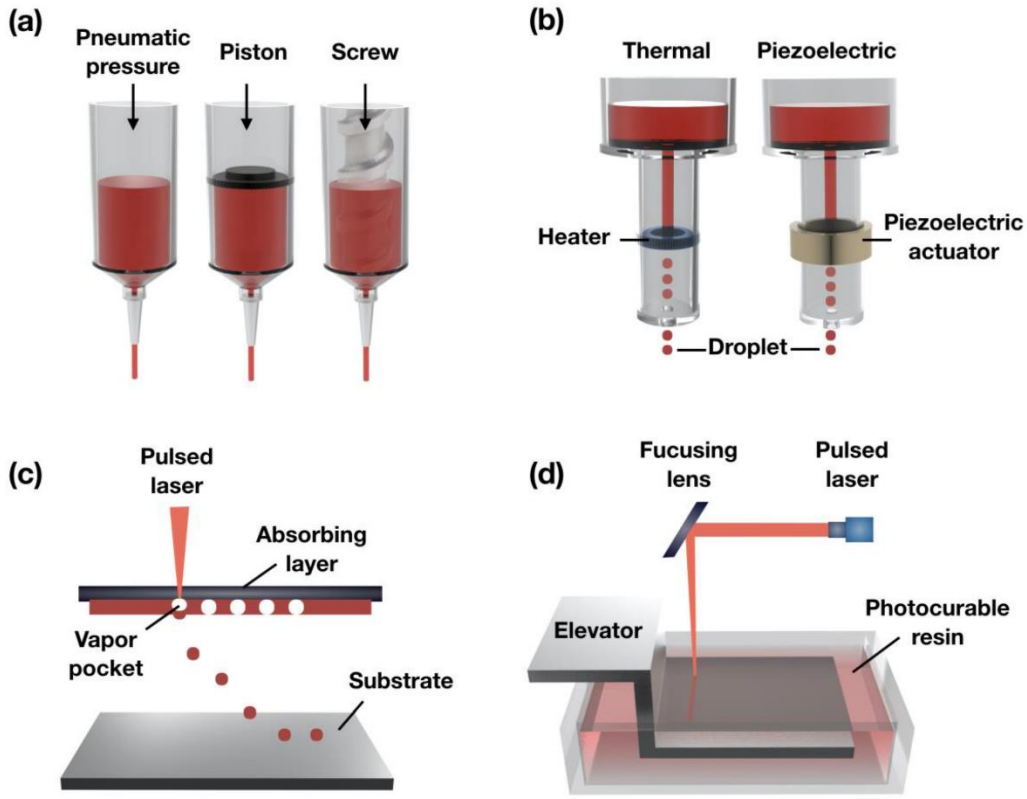

Fig. 2 Drawings of 4 variations of the bioprinting process: (a) extrusion bioprinting; (b) ink-jet bioprinting; (c) assistant laser bioprinting; and (d) stereolithography-based bioprinting. Figure reproduced from Jeong et al (2020) (CC BY) [11].

Creating a bioengineered tissue without a scaffold via traditional cell-sheet engineering relies on more human interaction with the tissue. The advantage of this method is that the cells can be grown on substrates like a nutritious agar, upon which growth characteristics are more stable and well known. However, creating complex tissues for this method requires layering of multiple cell types and creation of complex shapes requires manual manipulation. This method is advantageous for simple shapes like skin tissues, but blood vessels, esophagi, or other tubular structures need to be wrapped and stitched into shape. While simpler, less layered structures are much easier to produce, real tissues that the bioengineered tissues are designed to emulate are often much more complicated. Real tissues have multilayered cell compositions and can generally be described as having an epithelial, mesothelial, and endothelial layer, such as in Fig. 3. In skin this would form the epidermal, dermal, and hypodermal layers [12]. These each have different properties and functions. Emulating this layered property in a bioengineered tissue can be done by growing successive layers on top of each other but enhances the challenge of nutrition.

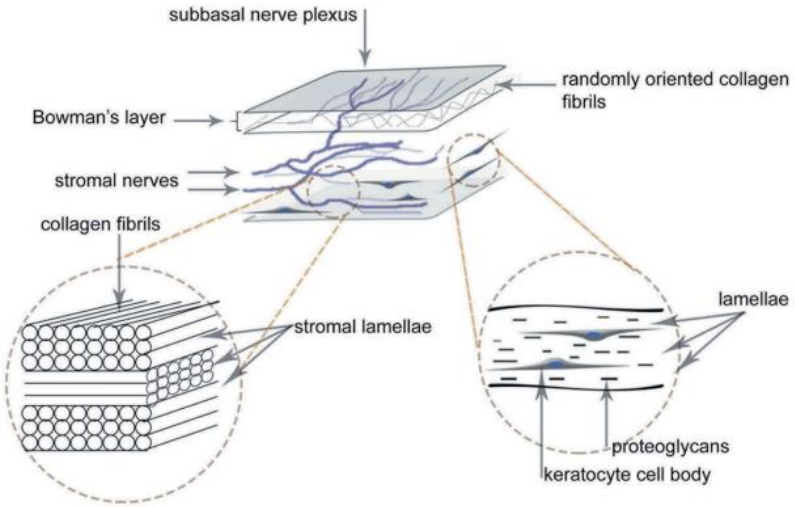

Fig. 3 Schematic of collagen alignment within layers of the cornea. Layers have different alignment of collagen fibrils and other tissue components which affect the properties and functions of the layer. Figure reproduced from Lagali (2019) (CC BY-NC-ND 4.0) [13]

Important to any tissue growth is ensuring cells are fed. The common petri dish growth method requires cells to receive nutrition from a layer below or from a growth media above the cell layers. This limits tissue thickness according to the diffusion of nutrients through the layers [14]. Real tissue has vascularization that feeds the cells, but is difficult to reproduce in engineered tissues due to the complex shape and fine features of vascular networks. Thus, attempts have been made to use decellularized plant vascularization as a scaffold [15]. Additionally, many tissues have layers of collagen integrated within the tissue, Fig. 3, that may be aligned within specific directions [16]. Application of forces during the growth process is the best way to get a tissue to naturally align the collagen fibers, while electrospinning is a common method to produce anisotropic collagen alignment [17].

All of these production components have an effect on the tissue's mechanical properties. A scaffold obviously affects bulk properties as many scaffold materials are much stiffer than cellular tissues. Meanwhile the mechanical properties of tissues can determine whether the tissue functions properly. Any location a tissue can be applied in a human body undergoes physical forces and the tissue must properly resist these forces. Skin is subjected to tearing, compression, and stretching forces as that body part is moved [18]. Blood vessels undergo a cycle of radial forces with each heartbeat applying pressure to the blood inside the vessels [19]. Ligaments and tendons operate completely under tensile forces as they hold muscles and/or bone together. Some tissues have even been found to grow significantly better under the appropriate mechanical force, as is particularly the case with aligned-collagen tissues [20].

2.2. Modeling

The construction of these bioengineered tissues can result in a complex structure. This can make a pure mechanical estimation of the tissues difficult. As the tissues present viscoelastic and linear elastic properties and may be direction dependent, much effort has been put into creating models and methodologies to estimate the properties of tissues.

2.2.1. Mathematical modeling

The simplest model used to understand the mechanical properties of tissues estimates movement of masses in general. This uses a spring to represent the linear elasticity of the material and a weight for the mass of the material, Fig. 4. Cells, however, contain over 70% water and thus also display a viscoelastic response. This viscous component is modeled as a dashpot, Fig. 4.

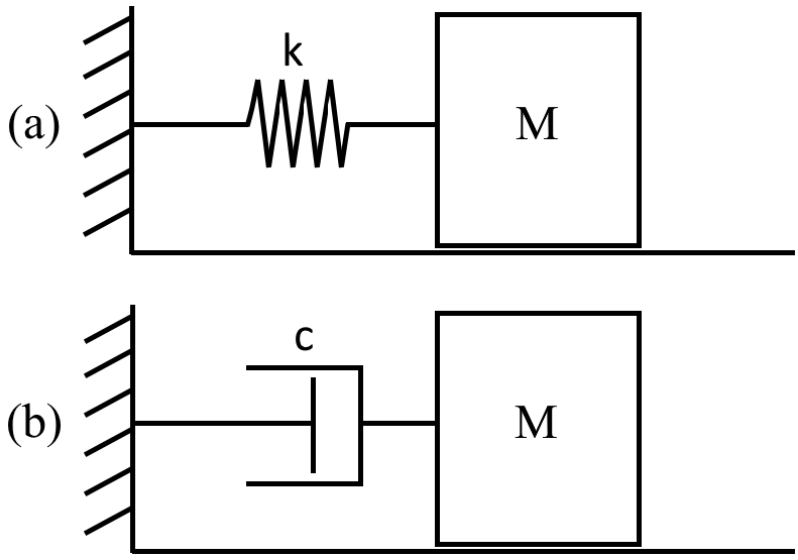

Fig. 4 Fundamental components used to construct mathematical models of viscoelastic materials: (a) spring with constant k; (b) dashpot with constant c.

More complex models can be used to analyze the motion of tissues and estimate their properties that use a combination of springs and dashpots, Fig. 5. These models all have an advantage to their simplicity, though this ends up decreasing their accuracy. For example, they are limited to only single axis motion. They can, however, be used as a rudimentary modeling tool to analyze the motion, stiffness and elasticity, or viscoelasticity, of the system [21]. Their main advantage is that they can be combined in similar ways to resistors and capacitors in electrical diagrams, allowing for mathematical representation of a more complex response.

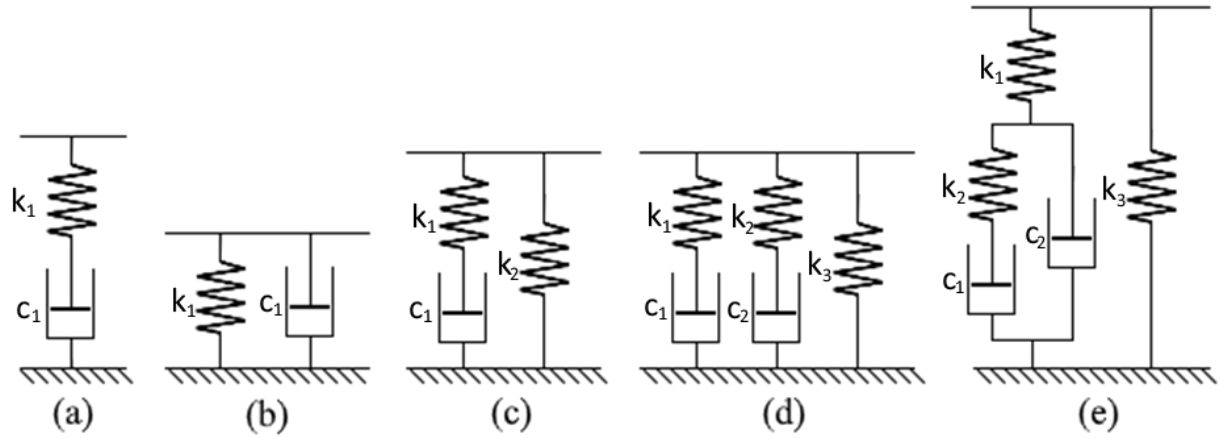

Fig. 5 Accepted mechanical lump models to study viscoelastic materials. (a) Linear Maxwell model; (b) Linear Kelvin-Voigt model; (c) standard linear solid model; (d) Wiechert model; and (e) Nafion model [21].

Adding more dimensions to the model quickly creates complicated analytical estimations with a high degree of geometric specificity. These models have limited applications, but they also can account for boundary conditions, which can significantly increase the accuracy of the models. For example, classical plate theory (CPT) can be used to model the properties of plates. Analyses have been developed for plates of many shapes, including circles, squares, and ellipses, and can relate thickness, density, stiffness, vibrational shape and frequency, displacement, and applied

forces [22]. This only works for thin plates, however, that are flat before application of pressure and consist of a single layer. It does not accurately model multi-component viscoelastic behavior shown in tissues. Alternative methods approximate such composite structures as a mixture or matrix and mathematically combine the properties of different components of the structure based off of their proportion within the composite.

A combination of these two models is the sandwich model, which accounts for multiple layers. It is similar in geometric application to classical plate theory, but generally creates a three-layered model in which the middle layer is viscoelastic or contains significantly less stiff properties such that it acts to dampen motion of the whole system [23]. The main downside of this model is its analytical complexity. Both CPT and the sandwich model tend to describe the motion of plates in waves as determined by Bessel functions. An example of the basic Bessel function for a function *y(x)* and constant *v* is shown in Eq. 1, but expansion of this to specific circumstances such as radial coordinates for a circle yield the mathematically relevant equations. In Eq. 1 the function *y(x)* defines a y-axis response to across the x-axis in accordance with time for a constant *v*.

$$x^2 \frac{\partial^2 y}{\partial t^2} + x \frac{\partial y}{\partial t} + (x^2 - v^2)y = 0 \quad (1)$$

Bessel functions require applications of specific geometries and other assumptions such as free or forced vibration to solve. Solving for an eigenvalue yields a constant which is well tabulated in Bessel function tables, allowing for relation of different waves through a few constants. Similarly, it is possible to model the properties of a material via the surface waves passing through the object. This is particularly valuable for viscoelastic materials, as more complex constants can estimate the viscoelastic properties, such as the Lame constants λ and μ in Eq. 2 [24] and thus analyze the degree of viscoelasticity of a material. Here ρ is the density of the material.

$$(\lambda + \mu)\nabla\nabla \cdot u + \mu\nabla^2 u = \rho\frac{\partial^2 u}{\partial t^2} \quad (2)$$

2.2.2. Computational modeling

Computational methods involve simulation analysis and machine learning methods. Simulation analysis, most commonly finite element analysis (FEA), is a well-developed tool that is commonly used by researchers to analyze biological tissues and non-biological components alike. FEA works by simplifying a system into a number of nodes and elements and assessing the relation between those elements. A very simple model, for example, might analyze the diffusion of a substance or property like heat through a material by sequentially calculating the transfer from one small element to another. It uses discretization of a large material into many smaller sections to make calculations easier. Spatial behavior of a material can be analyzed by analyzing the interaction of each node with the nodes around it. The underlying mathematics of the system follows simple models, like the lump models discussed in Section 2.2.1. Application of these simple models to each node can allow for a significantly more complex geometrical model to be analyzed.

A different approach, machine learning, can be used to measured data or observed results to desired properties according to complex connections that are difficult to see through normal methods. Machine learning falls into two general categories: supervised learning and unsupervised learning. Unsupervised learning uses data that has no labels or classification to identify patterns that may exist but are hidden [25]. An example of this method is a k-means algorithm which groups data into *k* clusters, assigning data points to the cluster with the closest centroid. The algorithm then optimizes centroid locations to produce the most distinct clusters with the smallest deviation values from the centroid, thereby grouping the data [26].

The alternative approach, supervised learning, is more applicable to mechanical properties of tissues. Supervised learning requires input of the labeled data to train the algorithm, and some instructions on the label of data. Two different types of supervised learning approaches are classification in which the algorithm puts data into different classes and regression in which the algorithm relates variables together. The easiest to understand regression example is linear regression in which an independent variable's value is used to predict the value of the dependent variable. More complicated models can be made, such as neural networks which are used for classification. Neural networks use a combination of nodes within several hidden layers which contain weighted functions and assigned thresholds, Fig. 6. When a node exceeds a threshold, it activates and passes information to the next layer, similar to neurons in a brain. This can allow for comparison of an increased complexity of outputs, but there is still a single target output that it targets.

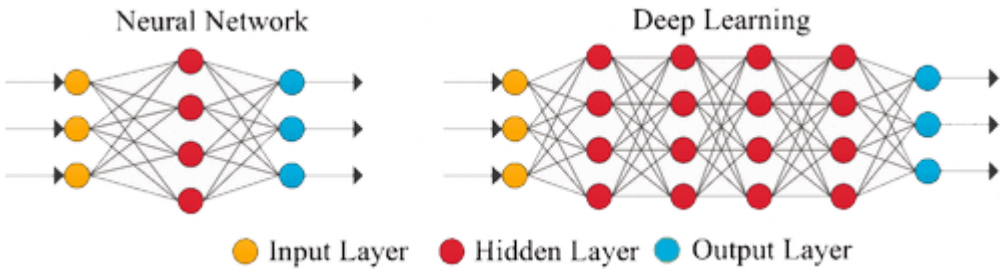

Fig. 6 Neural network structure [27]. Information is input and passed through several layers of weighted functions in the hidden layers to reach a single output. Deep learning models use a large number of hidden layers. Figure adapted from Xing and Du (2018) with permission from SAGE Publications [2019]

A family of learning algorithms within neural networks is deep learning. Deep learning has been applied to classification of handwritten digits, image recognition, acoustic modeling, and computational biology [28]. It has the distinction of being a neural network with many

hidden layers, Fig. 6. One such type of deep learning approach is the convolution method, Fig. 7, which identifies properties, or objects within the image and applies weights to them. It differentiates the components of the image, and then outputs desired information related to the information. In this way it requires less pre-processing than other classification methods [29].

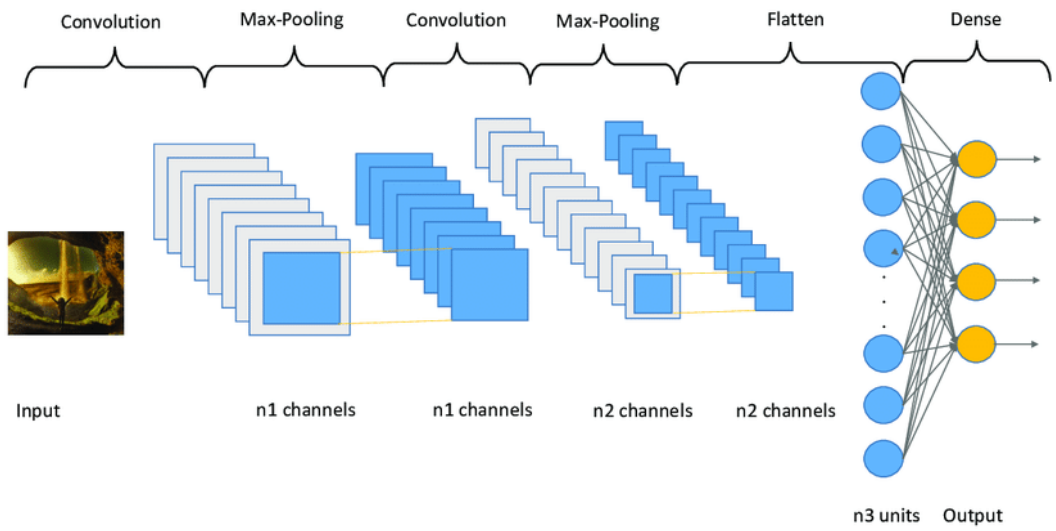

Fig. 7 Representation of the convolution neural network. An input image is separated into components and critical objects are identified, allowing for output of discrete variables or parameters. Reproduced from Garcia-Ordas et al (2020) (CC BY) [30]

These algorithms can be applied to determine mechanical properties by connecting the properties to observed results with classification, connection of one variable to another with regression, or finding the strongest correlation with neural networks. The advantage of these algorithms is that they can find relations that human researchers could not predict or could not pair a mathematical equation to. The downside, however, is that they require a two-step process in which the algorithm is trained with real data and then used to identify unknowns related to this original training. The training step requires a large amount of data with known values that are not

skewed and are well distributed. They are, therefore, appropriately specific to each type of material and after being retrained for a new material can bypass many other estimation steps.

2.3. Experimental investigation of mechanical properties

Experimental testing provides known ways to find various mechanical properties of a material. There are a variety of methods to measure the mechanical properties of materials. The most well used and developed methods tend to include the contact methods. For many measurement applications, contact and destructive methods are acceptable. This Section focuses on biological tissue-based measurement applications of these methods.

2.3.1. Contact methods

Contact methods to measure mechanical properties of a material are commonly used. These include tensile testing, indentation, and atomic force microscopy (AFM), among others. Other techniques do exist, such as analysis via compression or rheology, but this Section discusses the most common methods.

2.3.1.1. Tensile testing

One of the most common measurement methods is a tensile test, such as with an Instron. This device pulls a material and measures the strain resulting from the applied force, allowing for identification of the modulus of elasticity. Less common are biaxial tensile tests that operate the same way but in two directions at once. This can create an entire stress-strain curve such as seen in Fig. 8 with several notable points of information.

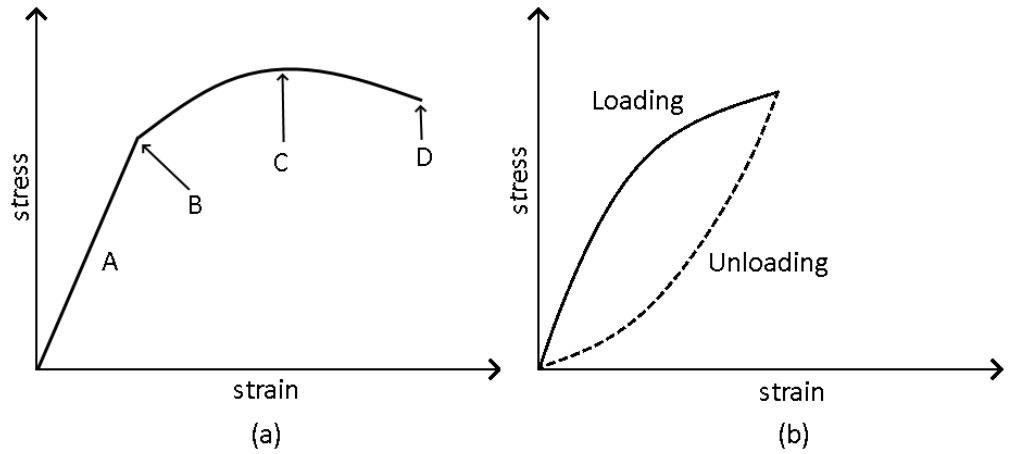

Fig. 8 Example of typical stress-strain curves: linear-elastic material. Measurements ideally occur in region A, well before significant strain is reached; (b) viscoelastic material [31].

The extent to which the initial slope is linear, Fig. 8a-A, indicates if the material behaves elastically during its return to zero or if there is fatigue or hysteresis. The nonlinear region also indicates the yield strength, Fig. 8a-B, at which the material deforms plastically such that it has been permanently damaged and cannot return to its original state of 0 strain. Some viscous materials may exhibit a non-linear relationship between stress and strain. This indicates some non-solid portion of the material, and these may be accompanied by a different stress-strain relationship while a force is being applied and removed, Fig. 8b. Finally, stress-strain graphs indicate the ultimate tensile strength, Fig. 8a-C, which is the maximum stress that can be applied, and the fracture point, Fig. 8a-D, where the material breaks. Both a uniaxial and biaxial tensile test may yield this information, but if a material is anisotropic such that it exhibits different properties in different directions, the biaxial tensile test provides more information via a second axis of measurement. Despite the extent to which this method is developed and the large amount of information it provides, it requires specific clamping patterns, Fig. 9, to hold the material and

damages the material. It can thus only be used on representative samples within a production batch of a material.

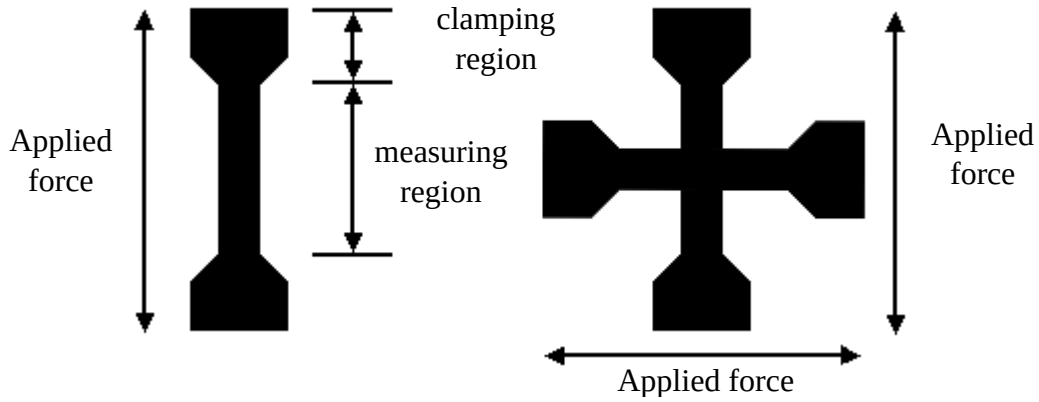

Fig. 9 Clamping and applied force for tensile testing:
(a) Uniaxial tensile testing; (b) biaxial tensile testing schematics.

2.3.1.2. Indentation and AFM

Another common test to determine mechanical properties is with a microindenter or nanoindenter. This technique uses a small tip with known properties and pushes it into the material. The relation between the movement into the material and the force applied can be used to extract the stiffness or the hardness of the material [32], Fig. 10. Indentation is significantly less invasive than axial testing as it indents a small spot but leaves the rest of the material untouched. However, it is still invasive and is prone to complications with wet materials where the adhesion of the indentation probe to water molecules or other polar surfaces may alter the results [33]. Several different mathematical models have been created to account for this occurrence such as the JKR model, as opposed to the standard Hertzian model which does not account for adhesion.

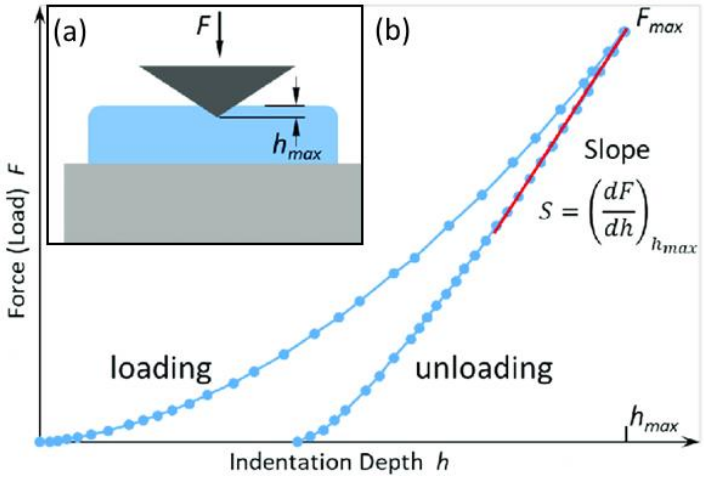

Fig. 10 Characterization of mechanical properties by nanoindentation: (a) Schematic of indenting a sample; (b) Representative measured loading and unloading curves. Properties are extracted from the slope at the beginning of the unloading curve. Reproduced from Utke et al (2020) (CC BY) [34]

Similar to indentation is atomic force microscopy (AFM). AFM uses a scanning probe microscope to measure the surface of a sample. Its solid tip, resting on a cantilever beam to make forces very small, interacts with the atoms on the surface of a sample, Fig. 11. It can measure friction, adhesion, or viscoelastic properties in addition to Young's modulus, all by the deflection of the cantilever beam that holds the tip. As it measures atomic interactions, it has a very high resolution and has even been used to study nanoscale structures such as DNA. It has also seen success in some dental applications [35]. Its greatest strength, its resolution, is also its greatest limitation, however. The fine tip can only measure a single point at a given time and while its measurement is real-time, it is inherently slow for a large surface and offers no depth measurement method. Additionally, it's fine and precise nature makes it a costly measurement method.

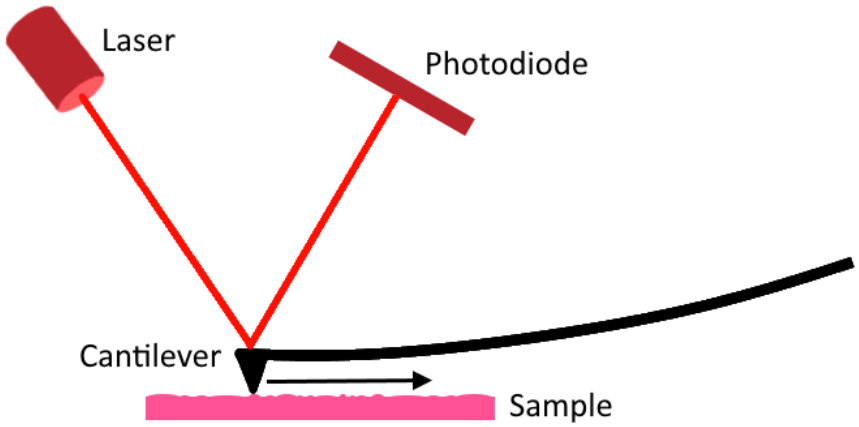

Fig. 11 Schematic of AFM measurement method. The cantilever moves across the sample and measures the surface roughness. The laser and photodiode measure the deflection of the cantilever.

2.3.2. Noninvasive methods

This paper discusses noninvasive characterization of the mechanical properties of bioengineered tissues. Tools related to such noninvasive development can be focused on three techniques: scanning acoustic microscopy, elastography, and optical methods.

2.3.2.1. Scanning Acoustic Microscopy

Scanning acoustic microscopy (SAM) measures ultrasonic waves travelling through an object. As the ultrasonic acoustic wave reflects off of a surface, it interferes with retransmission from surface acoustic waves, Fig. 12. This leads to the ability to calculate the stiffness of the material. This results in a high resolution down to a micrometer scale [36]. This technique does suffer significant attenuation in softer materials and is thus best used for harder materials, but it has been used to determine mechanical properties of vascular tissue *ex-vivo* [37]. A disadvantage of this technique is that the area between the ultrasonic acoustic lens and the sample must be filled

with water, making this only viable for measurement of substances that can be put in water such as *in-vitro* measurements.

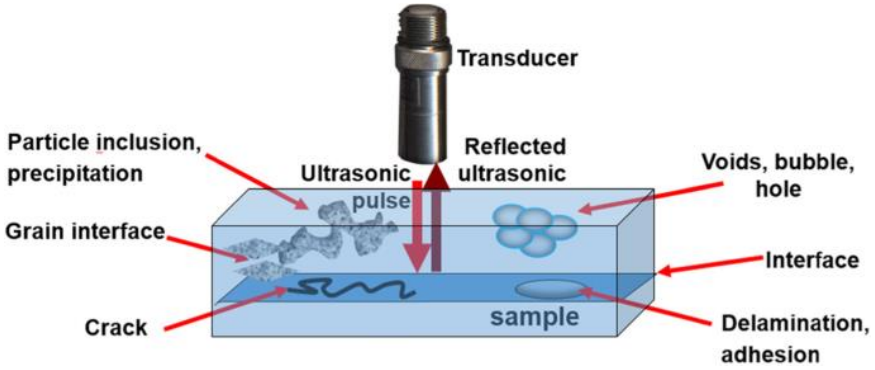

Fig. 12 Drawing of Scanning Acoustic Microscopy (SAM). Several non-uniformities are shown that SAM is used to detect. Reproduced from Yu (2020) (CC BY 4.0) [38]

2.3.2.2. Elastography

Elastography is a process which uses light, sound, or magnetic imaging that can pass through solid materials to image physical waves passing through a tissue. It thus allows for volumetric analysis of tissues but does require a physical force application. The technology started with the development of ultrasound into ultrasonic elastography (UE) and has since included magnetic resonance elastography (MRE) and optical coherence elastography (OCE), Fig. 13. Each has a different range of acceptable resolutions and speeds, Fig. 14, and as such each has been used for different applications towards measuring properties of tissues, particularly *in-vivo.*

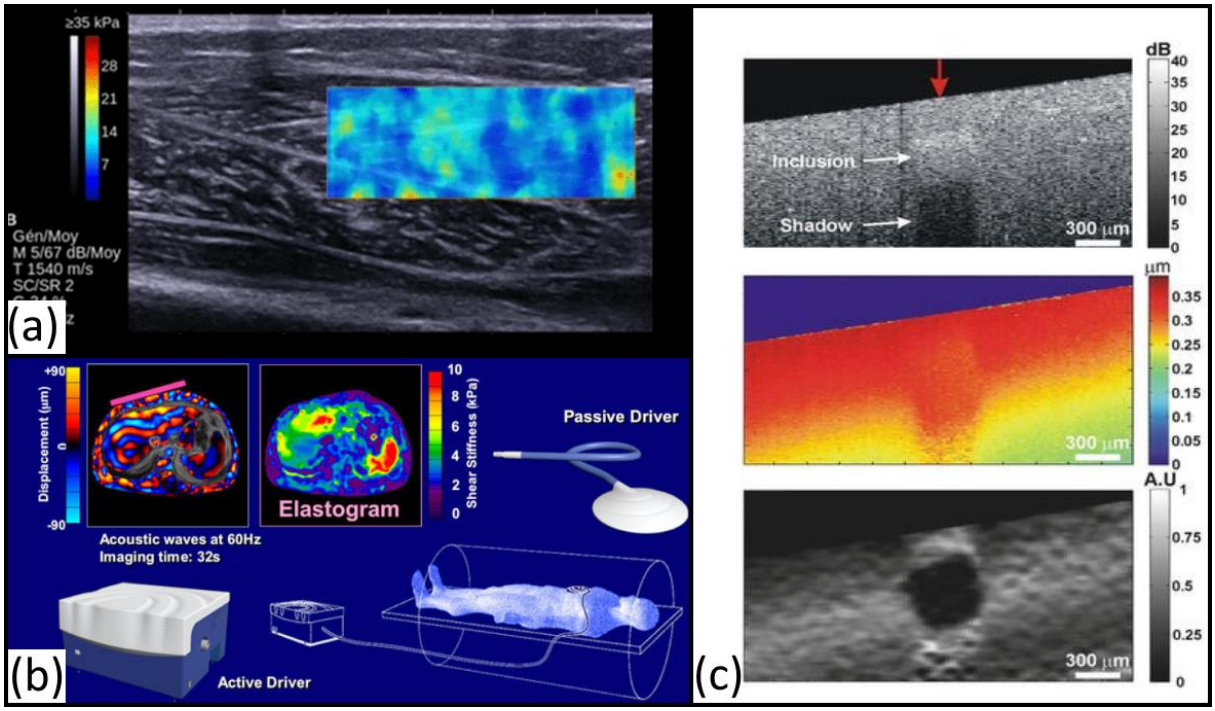

Fig. 13 Examples of elastography machines: (A) Ultrasonic elastography machine and examples measurements. Reproduced from Lallemant-Dudek et al (2021) (CC BY) [39]; (B) Magnetic resonance elastography schematic and example measurements [40]; (C) Optical coherence elastography example measurements. Reprinted by permission from Springer Nature: Springer eBook. Optical Coherence Elastography by Elastography by Brendan F. Kennedy, Kelsey M. Kennedy, Amy L. Oldenburg et al [2015].

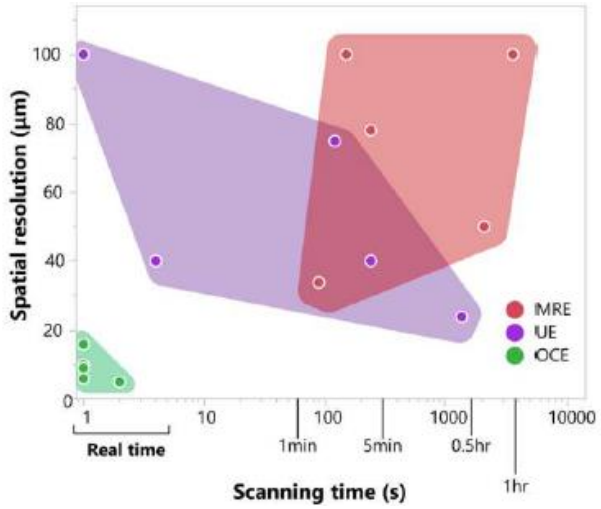

Fig. 14 Temporal and spatial resolution of elastography techniques. OCE has the smallest spatial resolution and can be applied in real time. UE is based on machines widely used for ultrasound imaging. MRE is used in hospitals via MRI machines. Reprinted by permission from Springer Nature: Springer Nature, Annals of Biomedical Engineering. [42] [2016].

UE and OCE work very similarly, measuring the time it takes for sound waves (UE) or light waves (OCE) to reflect and creating an intensity profile called an A-scan indicating where tissue boundaries are located. Applied spatially, these can make a 2D image called a B-scan, and a number of these can be put together to form a 3D image. Thus, to generate a volumetric image the measuring device is creating multiple 2D frames and putting them together, which increases the time for processing. MRE works slightly differently by using instead an MRI to measure the tissues in a patient's body. All of these methods, however, require application of a force to create waves through the tissue. Several methods are presented in Fig. 15.

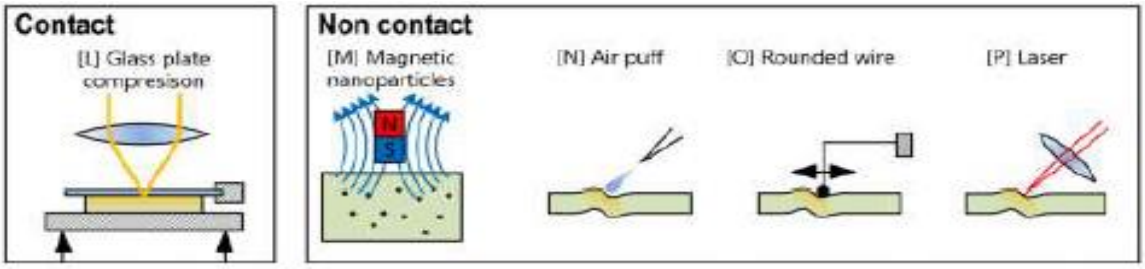

Fig. 15 Methods of wave induction for elastography measurement. Elastography measures the propagation of these waves through a tissue. Reprinted by permission from Springer Nature: Springer Nature, Annals of Biomedical Engineering [41]. [2016].

The mechanical properties of tissues have been known to change when in a diseased state, so the use of elastography typically is applied to identification of the elasticity of internal organs. UE has been used to identify liver fibrosis, chronic kidney disease, and many other diseases [42]. As OCE relies on penetration of infrared or near-infrared light [43], its application is limited to exterior components. Due to its high resolution, it has seen success with characterization of skin and breast tissues, near-surface blood vessels, and ocular components [44]. MRE, meanwhile, is primarily used to identify liver fibrosis [45].

OCE has the best resolution as OCT devices can image micron level morphology, it does have a downside when applied to elastography. It largely makes use of speckle tracking which limits its use with large speckle pattern shifts which result in a more noise and a large error margin [46]. Still, its application towards *in-vitro* bioengineered tissues is greater than either UE or MRE due to its resolution and speed.

2.3.2.3. Structured light techniques: fringe projection

Optical techniques can be used to image objects' morphology noninvasively. One such technique used to characterize properties of bioengineered tissues is structured light fringe projection [50]. A method developed by Castro [47] presents Air Puffing Fringe Projection (APFP) as a noncontact technique similar to indentation. This uses fringe projection via a Michelson-interferometer to project structured light onto a sample, Fig. 16, and a camera to image the fringes. Any deformation in the tissue induced by a puff of air from a pressurized nozzle bends the fringes, which is measured by the camera.

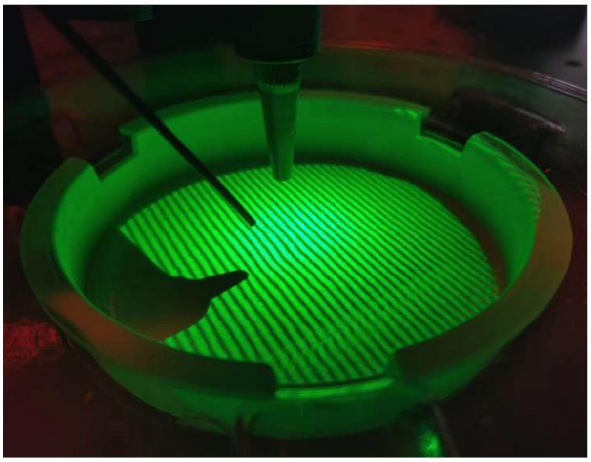

Fig. 16 Imaging of Apligraf tissue with APFP method. Green structured light displays fringes onto the tissue while a nozzle is lowered from the left to apply the air puff with a camera in the center directed normal to the tissue. Reproduced with permission from Castro (2020) [47]

Castro relates the deformation of the air puffed region to physical properties using this method by analyzing a curve fit of the displacement, Fig. 17. Measuring the same bioengineered tissue used in this Thesis, he calculated an elastic stiffness of 155 ± 5.2 kPa and reported a range of 200-250 kPa from literature. This method has been demonstrated on this tissue and a urethane sponge and has the potential to measure other soft materials.

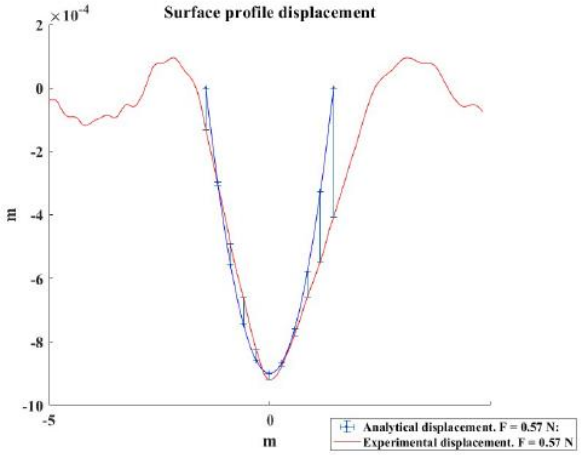

Fig. 17 Surface displacement profile from APFP measurement in a bioengineered tissue. The curve fit (blue) is used to calculate mechanical properties of the tissue. Reproduced with permission from Castro (2020) [47].

This APFP method has several limitations of note. Displacements from forces over certain limits produce saturated pixels and thus prevents recovery of the images needed to calculate the displacements. Additionally, it is possible that the force provided by the pressurized air exceeds the elastic limit of the bioengineered tissues, changing the assumptions of the calculations and altering measurements. The APFP method does not account for complex, multi-layered structures and calculates bulk properties that do estimate non-homogeneity or anisotropy within a material. Finally, the method is non-contact, but the application of an air puff requires separation of a sample's packaging to expose is to the environment. This has the potential to allow a bioengineered tissue to dry or be exposed to contaminants and is thus not completely non-invasive.

2.3.2.4 Holographic techniques

A second type of optical technique that can measure surface morphology is digital holography (DH). Such techniques have been used to image deformations within ear drums of chinchillas [51]. DH uses the interference of light between two beams with slightly different path lengths to measure deformations or surface characteristics of a sample. Like with structured light techniques, this imaging method is completely non-invasive and does not require opening a package to view a sample.

Deformations to be measured can instead be created by applying acoustic energy. An example of this was performed by Castro, who applied acoustical pressure to Apligraf biofabricated skin tissue at a frequency of 571, 834, and 1233 Hz, the latter of which is shown in Fig. 18. Such deformations measured by DH relate to the mechanical properties of tissues and can thus be used as a completely non-invasive method for determination of mechanical properties. Additionally, DH methods can image the full field-of-view of a sample and thus gather more information than single point methods such as indentation.

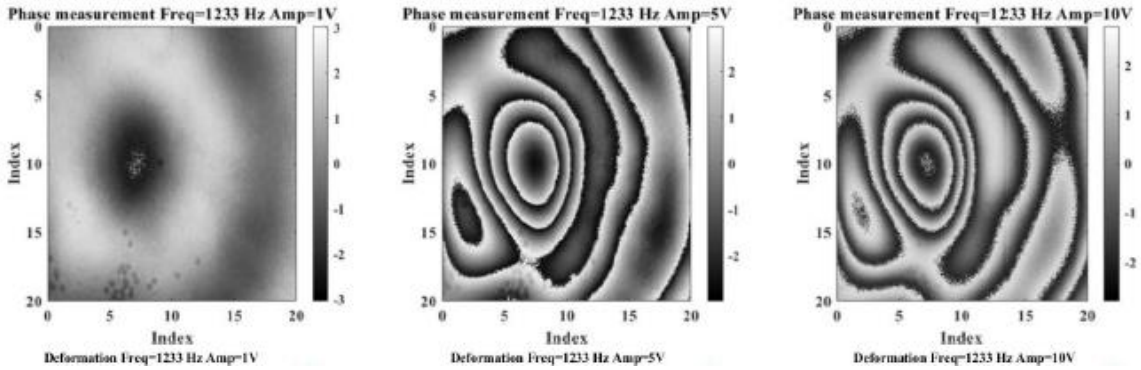

Fig. 18 Surface deformation measurements using DH on a bioengineered tissue. Deformation shows a primary displacement in the center of the tissue (image is offset from center) with waves propagating out radially. Reproduced with permission from Castro (2020) [47].

The advanced techniques can image either the interior of a tissue as in elastography, or the surface as with structured light and holography. These measurements, furthermore, are generally noninvasive and thus ideal for measuring bioengineered tissues. The issue comes with the application of a load. To create a displacement that the sensor will then measure requires some sort of excitation of the tissue. The use of acoustics and holography presents the best combination of noninvasive tools but there is still a need to establish that these holographic measurements can be used to identify the mechanical properties of the tissue. This method will be discussed in this thesis.

3. General methodology

The methodological objective of this Thesis is to create a noninvasive and nondestructive optical tool and method to measure the mechanical properties of bioengineered tissues. This Section describes the operative theory, construction, and validation of this tool.

The tool described in this Section is a digital holographic vibrometry (DHV) sensor. It uses acoustic energy from a speaker to vibrate a sample and stroboscopic digital holography to measure the out-of-plane displacement of the sample. A finite element (FE) analysis is created to model the sample and a parametric study is performed to generate a variety of models. These are used to train a machine learning (ML) algorithm. Post-processing of measured data on real samples in MATLAB creates pointclouds which are then passed to the ML algorithm for identification of properties. The outline of this process is shown in Fig. 19.

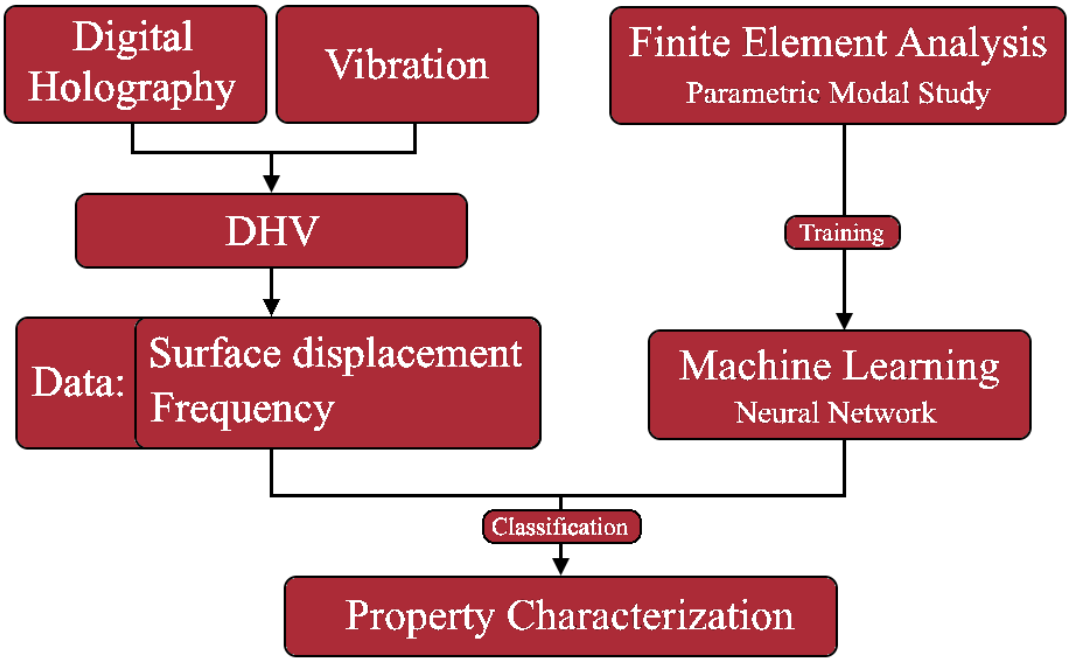

Fig. 19 Flowchart of general process in which DHV and machine learning are used in parallel to characterize a sample's mechanical properties.

3.1. Principles of methodology

The operation of the DHV sensor is dependent on two points of theory: acoustics and digital holography. These principles of theory are conducted through a CHSLT software called Laserview, but are still critical for analysis of measurements and will be discussed in this Section.

3.1.1. Holography

Holographic measurement has 4 primary phases: recording, reconstruction, analysis, and implementation. The first three will be discussed in this Section. The recording step of holography starts with the interference of light between two beams, one of which reflects off of the object that is measured. A laser outputs a beam which is split into a reference beam, Eq. 3, and an object beam, Eq. 4.

$$E_r(x,y,z,t) = A_r(x,y,z,t)e^{i\phi_r(x,y,z,t)} \tag{3}$$

$$E_o(x,y,z,t) = A_o(x,y,z,t)e^{i\phi_0(x,y,z,t)+i\Omega(x,y,z,t)} \tag{4}$$

So long as the path lengths are within the coherence length of the laser, interference between the two beams can extract differences in the path length travelled of the beams according to their interference at the sensor, Eq. 5.

$$I = \left|{E_o}^2\right| + \left|{E_r}^2\right| + {E_o}^* E_r + E_o\,{E_r}^* \tag{5}$$

As the object beam shines onto a moving object, the movement in the object can be measured. Taking a time averaged image results in an extraction of moving areas. In time-averaged imaging, the exposure time of the camera, *T,* is much larger than the period of the measured vibration, $1/\omega$. If the vibration is assumed to be sinusoidal, than the two-dimensional camera sensor image relates to the Z displacement according to Eq. 6.

$$z(x,y,t) = Z(x,y)sin(\omega t) \tag{6}$$

Then when the image is averaged across the exposure, the time averaged image can be described as Eq. 7.

$$\frac{1}{T}\int_0^T F_v dt = \frac{1}{T}\int_0^T a(x,y)exp\left[i\phi_0(x,y) + i\left(\frac{4\pi}{\lambda}\right)Z(x,y)sin(\omega t)\right]dt$$

$$= a(x,y)\exp\left[i\phi_0(x,y)\right]\frac{1}{T}\int_0^T exp\left[i\left(\frac{4\pi}{\lambda}\right)Z(x,y)sin(\omega t)\right]dt \tag{7}$$

In Eq. 7, the final integral is the characteristic equation as in Eq. 8, which can be defined in accordance with the Bessel function of the first kind, J_0.

$$M_T = \frac{1}{T}\int_0^T exp\left[i\left(\frac{4\pi}{\lambda}\right)Z(x,y)\right]dt = J_0\left(\left(\frac{4\pi}{\lambda}\right)Z(x,y)\right) \tag{8}$$

Using this Bessel function, the image intensity measured by the camera can be described by Eq. 9. In this image, dark fringes will appear when A_o is non-trivial and J_0 is zero. These fringes will thus occur in the direction of motion, orthogonal to the primary direction of displacement. By this means vibration patterns are identified with time averaged holography.

$$I_{im}(x,y,z) = \left[A_o(x,y,z)\right]^2[M_t]^2 = {A_o}^2\,{J_o}^2(|\Omega_t|) \tag{9}$$

Double exposure imaging methods are used to quantify these displacements in a vibrating object. In this method, two frames are imaged and compared. There are two phase stepped intensity patterns, recorded before and after a change in the object forming a reference image and a displacement image. The intensity patterns are described by Eqs 10 and 11 [61]

$$I'_n = I_B(x,y) + I_M(x,y)cos[\phi(x,y)] \tag{10}$$

$$I''_n = I_B(x,y) + I_M(x,y)cos[\phi(x,y) + \Delta\phi(x,y)] \tag{11}$$

Where I_B is the background irradiance and I_M is the modulation irradiance as determined by Eqs 12 and 13.

$$I_B(x,y) = I_o(x,y) + I_r(x,y) \tag{12}$$

$$I_M(x,y) = 2\sqrt{I_o(x,y) \cdot I_r(x,y)} \tag{13}$$

Here I_o is object beam irradiance and I_r is reference beam irradiance. $\Delta\phi$ is found by

$$\Delta\phi(x,y) = \phi_o(x,y) - \phi_r(x,y) \tag{14}$$

where ϕ_o is the phase distribution of the object beam and ϕ_r is the phase distribution from the reference beam. Most importantly, θ_n is the nth phase step. Each of the two frames that are compared require four images to be taken and put together with $\frac{\pi}{2}$ phase modulation. So, for I_1 $\theta = 0$, for I_2 $\theta = \frac{\pi}{2}$, for I_3 $\theta = \pi$, and for I_4 $\theta = \frac{3\pi}{2}$, as in Eq. 15.

$$\left.\begin{aligned} I_1(x,y) &= I'(x,y) + I''(x,y)\cos\big(\phi(x,y)\big) \\ I_2(x,y) &= I'(x,y) + I''(x,y)\cos\left(\phi(x,y) + \frac{\pi}{2}\right) \\ I_3(x,y) &= I'(x,y) + I''(x,y)\cos(\phi(x,y) + \pi) \\ I_4(x,y) &= I'(x,y) + I''(x,y)\cos\left(\phi(x,y) + \frac{3\pi}{2}\right) \end{aligned}\right\} \tag{15}$$

In the reconstruction phase, these are collated as in Eq. 16

$$I_{complex} = (I_3 - I_1) + i(I_4 - I_2) \tag{16}$$

Mathematically this equates to the arctan of the images:

$$\phi_o(x,y) = arctan\frac{I_4 - I_2}{I_3 - I_1} \tag{17}$$

This outputs a range of values from -π to π, with a fringe at every 2π jump. This inherently requires unwrapping to generate a continuous surface. The relation of this complex image with 2π jumps to the actual displacement of the object depends on the geometric implementation of the experimental setup. The path of the laser reflecting off of a mirror and onto the object forms a vector, $\overrightarrow{k_1}$, and the path of the camera's observation of the object forms a vector, $\overrightarrow{k_2}$. These vectors both have a magnitude of the wave number, Eq. 18, in which λ is the wavelength of the laser.

$$\left|\overrightarrow{k_1}\right| = \left|\overrightarrow{k_2}\right| = \frac{2\pi}{\lambda} \tag{18}$$

In the analysis phase of holography, these two vectors together form the sensitivity vector, Eq. 19. When the displacement vector, $\vec{L}$, is projected onto the sensitivity vector, Eq. 20, the phase, Ω, is achieved which can then be used to find the displacement of the recorded double exposure image.

$$\vec{k} = \overrightarrow{k_2} - \overrightarrow{k_1} \tag{19}$$

$$\Omega = \vec{L} \cdot \vec{k} \tag{20}$$

When the two vectors, $\overrightarrow{k_1}$ and $\overrightarrow{k_2}$, are parallel, the displacement measured by the double exposure image or time-averaged method will be out of plane. In this geometry, the out of plane displacement of the vibrating object, L_z, can be obtained by the magnitude of the sensitivity vector multiplied by the out of plane, *z*, component of the phase, Eq. 21.

$$L_z = \frac{\lambda}{4\pi} \times \Omega_z \tag{21}$$

3.1.2. Acoustics

The second component of DHV, the part that induces the change the holographic method measures, is acoustics. DHV uses a speaker to apply acoustic waves that can apply pressure to an object. A wave of sound can be pictured as a sinusoidal wave travelling through space. The wave has a wavelength, λ, and frequency, *f*, which together determine the wave speed, Eq. 22.

$$v = \lambda f \tag{22}$$

Within lower ranges of frequency, the wave creates an audible noise as it applied pressure to our eardrums and makes them vibrate at a similar frequency, which is then interpreted as a sound with relative pitch of *f*. The DHV sensor similarly makes the object being measured vibrate at the same frequency output by the speaker. This can be done with any type of speaker and frequency

range and has been done with acoustic chirps to measure vibration in chinchilla ears [48], but this Thesis uses a subwoofer that can operate within the lower hearing range of a human from about 30 Hz to 1 kHz. The pressure applied by the speaker is measured by a microphone, which converts the sound pressure into voltages that are related to the decibel sound pressure level (dBspl) according to the microphone's sensitivity. The dBspl level is then related to the sound pressure in pascals by Eq. 23, where the pressure is denoted by p and measured in pascals, and p_{ref} is the reference pressure usually set as $2x10^{-5}$ for 0 dB [49].

$$dB\ spl = 10\ log\left(\frac{p^2}{{p_{ref}}^2}\right) \tag{23}$$

In this way DHV applies a pressure to an entire sample at once, but with a small force equivalent to the amplitude of the acoustical energy. The object subjected to pressure from the speaker vibrates such that each point follows a sinusoidal curve similar to the sound wave. The period of the sound wave is equivalent to the period of the objects vibration cycle unless the object shows significant damped characteristics.

3.2. Practical implementation of theory

This Section discusses the implementation of the theory described in previous Sections to realize a digital holographic sensor with sample excitation by acoustical methods.

3.2.1. Experimental Setup

To minimize environmental disturbance, the entire DHV system is setup on a Newport Photonics optical table with active damping. The DHV sensor, Figs 20 - 22, uses a laser with a 532 nm wavelength, Oxxius, $L1C^{+}$-AOM-532 [50], which has a coherence length over 50m and an integrated acousto-optic modulator (AOM) to reduce the output laser beam to the first order of

diffraction. The beam is separated by a 90/10 beam splitter, with the 90% beam from here on referred to as the object beam and the 10% beam referred to as the reference beam. The reference beam bounces off of a piezo electric mirror that is used for phase shifting and is then coupled into an optical fiber. The other end of the optical fiber is on an elevated platform where the beam naturally expands exiting the fiber, passes through a ground glass beam diffuser to eliminate an interference carrier in the reference beam, then shines into a beam combiner. The object beam shines straight from the beam splitter to a 60x objective lens which expands the beam. This reflects off a mirror onto the table where a sample can be placed and screwed into the table for stability, Fig. 22. A mirror hangs directly above the sample area to redirect an image into a beam extender after which it bounces off of the previously mentioned beam joiner. At this point both beams together reach a CCD camera, Allied Vision, Stringray f504-b [51]. A data acquisition device, National Instruments, USB 6343 [52], controls the phase shifter and the camera trigger while a function generator, Tektronix, AFG 3102 [53], controls the AOM and a speaker.

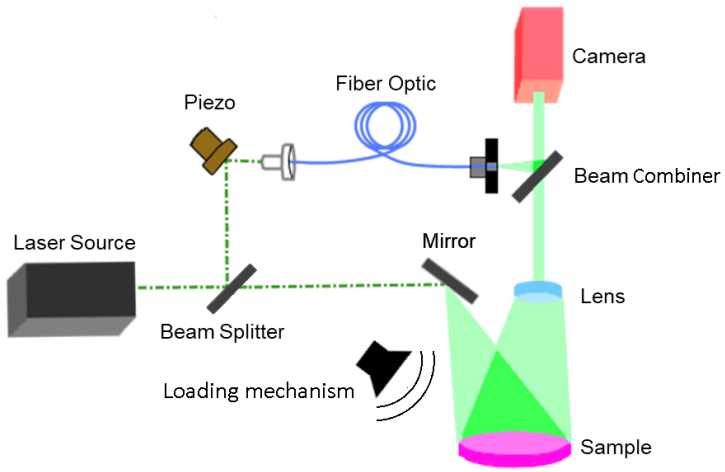

Fig. 20 A simplified schematic of the implemented digital holographic setup: a coherent light source is divided into two beams. One beam is used for illumination of the sample and the second beam is used as reference. Holographic image acquisition is synchronized with sample excitation via acoustics.

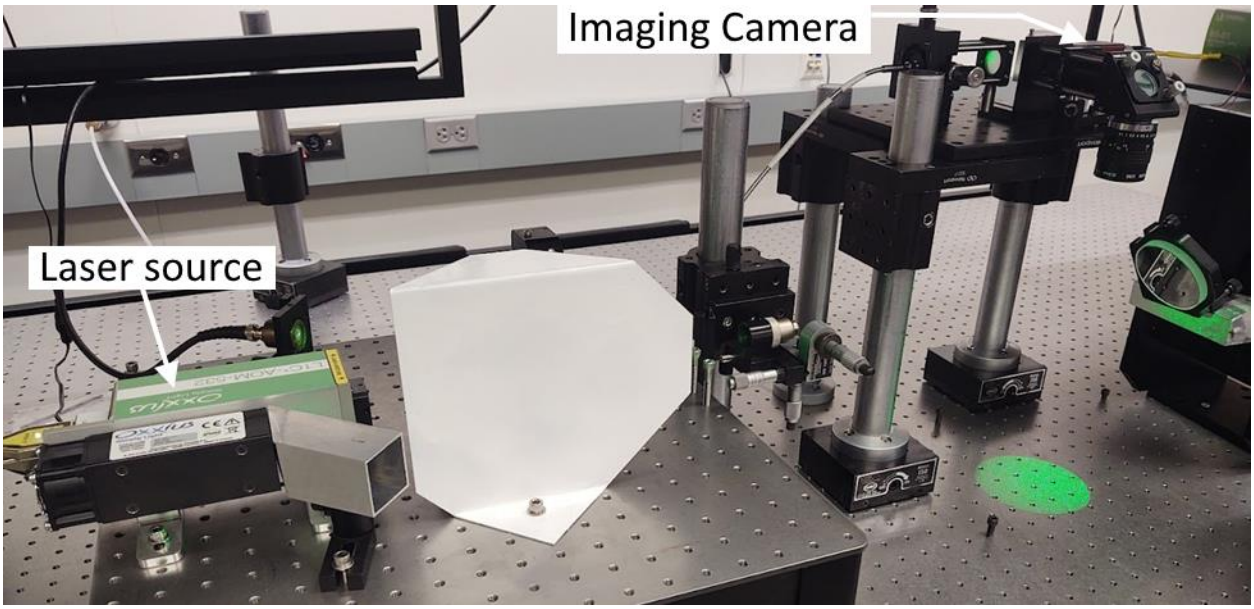

Fig. 21 Implementation of DHV sensor: laser is 532 nm wavelength source, 200 mW power. Reference beam is coupled through a single mode optical fiber. Illumination is conducted through refractive optics.

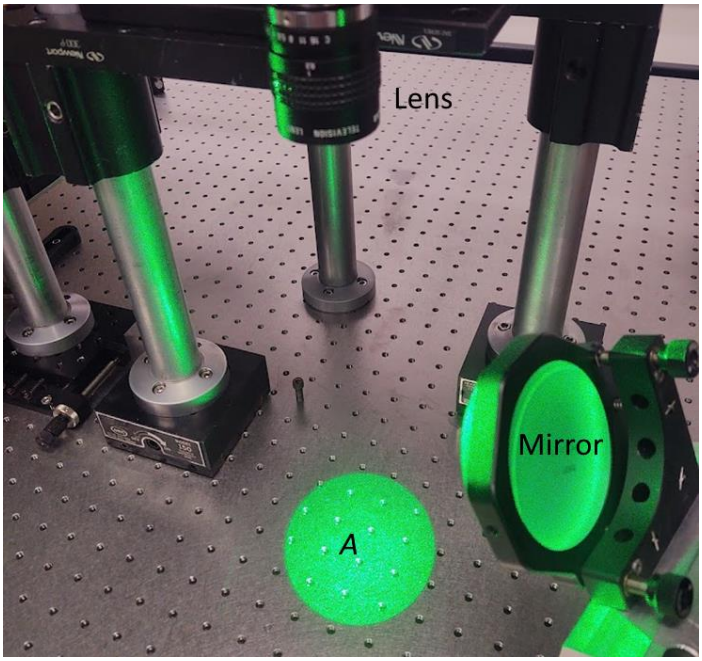

Fig. 22 Sample placement area for DHV sensor. Shown is the area, *A*, a 30° mirror that reflects the object beam to illuminate the sample and the imaging lens.

Attached to the lean bar of the optical table to isolate its vibrations from the damped table is a speaker, Fig. 23, Jensen, C8R [54]. This speaker is controlled by the frequency generator which outputs a single tone frequency, transmitted through an amplifier, Crown, XLi 800 [55].

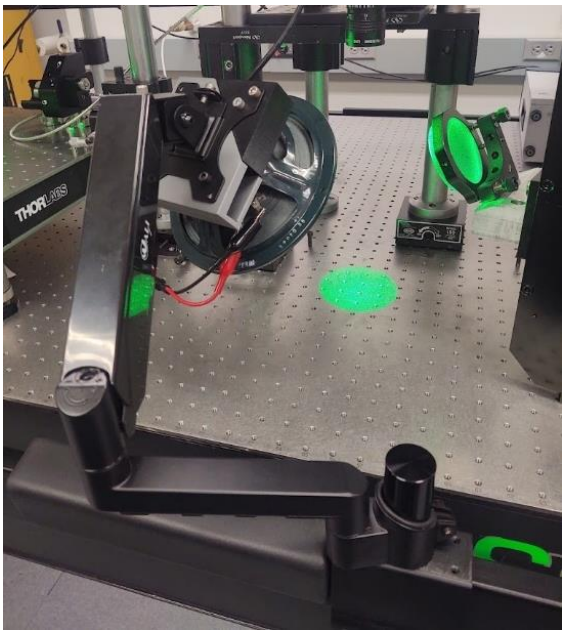

Fig. 23 Placement of the speaker within the DHV configuration. Distance between the speaker and the sample is selected to minimize acoustical interference.

With a sample placed into the lighting area, the camera is focused, and the reference/object beam ratio is calibrated to be as close to 2.1 as possible. Imaging is conducted through an inhouse software caller Laserview which can coordinate the camera shutter with the piezoelectric mirror and the AOM in the laser as well as control the frequency of the speaker, imaging mode, and camera exposure.

3.2.2. Vibration measurements

The process of taking a single measurement occurs in two phases: mode identification and imaging. Before any images are taken place, the camera is focused onto the object and a scale is imaged to determine an accurate pixel to millimeter ratio for later processing. The laser is then turned on and lights in the room are turned off, a single tone frequency is output by the speaker. The sample is viewed in time average mode which allows for rapid identification of fringe locations. The speaker frequency is manually controlled to start as low as the speaker is audible, around 40 Hz, and increase slowly until the desired vibrational pattern is obtained. The exact frequency is found by moving the frequency until the greatest number of fringes is located for the desired pattern, and then the frequency is marked down. This is repeated for subsequent vibrational patterns that can be found. Eventually the frequency reaches a high enough level that the measured fringes are too small, too many, or too chaotic and no longer reaching meaningful patterns, such that the frequency sweep is terminated.

Through Laserview, the camera and AOM strobe is then turned on, to ensure they both strobe simultaneously with a 10% duty cycle, and the camera exposure is automatically adjusted to maximize imaging quality. The strobe allows for imaging of the sample during just the duty cycle to approximate one point within the sample's excited vibration cycle. Modification of the phase between the frequency and the strobe results in imaging of different points within the vibration cycle, Fig. 24. The imaging mode is switched to optical phase mode and the frequency is adjusted. At each marked frequency a reference is taken before the speaker is turned on, and then the speaker is turned on as images are taken in an LVvid video format. This setting automatically takes the 4 images necessary to create a complex image, then modifies the optical phase by 30 degrees, and takes another image. It does this a total of 12 times resulting in 12 images

representing points spread evenly across the vibrational cycle. The process may be repeated multiple times to determine consistency and may be repeated at different speaker volumes depending on the time and objective of a particular experiment. The speaker volume is changed by increasing the voltage applied to the amplifier and results in a direct change to the pressure applied by the corresponding sound wave.

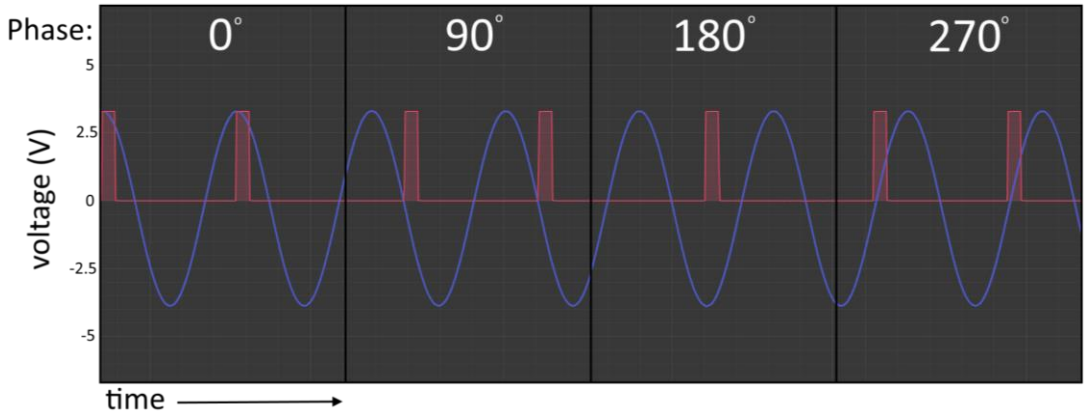

Fig. 24 Overlay of laser strobing (red) with frequency output for speaker (blue). The phase, controlled by Laserview, modifies image acquisition compared to the frequency curve. The time axis is dependent on the frequency of excitation.

3.2.3. Post-imaging processing

LVvid files are read by a lab MATLAB program, so once the Laserview program outputs the LVvid file, all following image processing is performed in MATLAB. The video files are separated by extracting 4 frames at a time and combining them into a complex image using Eq. 16. All non-sample parts of the image are then masked so that all data points in the image not representing the desired sample are removed. The remaining image is unwrapped with the Goldstein unwrapping algorithm [56], a process which modifies an image such that any jump with a value of 2π between two points is modified to be a smooth contour. This transforms an image from a series of $-\pi$ to π segments into a smooth surface. A reference point for this algorithm is

selected automatically by locating a point with at least 90% intensity. At this point in the process, data consists of a matrix where rows and columns relate to *x* and *y* pixels and values in each cell indicate *z*-displacement values. The matrices are then scaled as in Eq. 21 to change z values to accurate nanometer measurements. Finally, z values are referenced by selecting a known zero value area of the sample, such as next to a fixed boundary condition, and then the z-value of this data point is subtracted from all data points.

In a second MATLAB program, images are collated such that the 12 images taken within 1 vibration cycle are laid out horizontally. Multiple trials are then laid out vertically so that all images taken of a single vibrational mode can be visualized at once to aid in mode identification. Figure 25 shows an example of this while Appendix A shows a set of real measurements. In the same program, the matrices are converted to point clouds which consist of a $n \times 3$ matrix where each column is the *x, y,* and *z* value respectively, over n data points. At this point all x and *y* values are multiplied by the pixel-to-millimeter ratio found in earlier steps. This pointcloud now contains real values of displacement for the entire structure. Pointcloud files are the passed to the data science lab to be integrated with a machine learning algorithm.

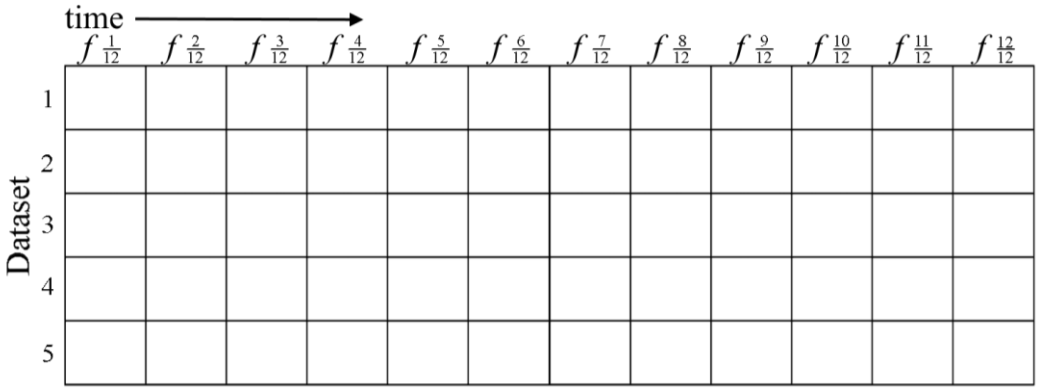

Fig. 25 Composite of measured images. Each box correlates to a single image. Horizontal axis shows multiple images taken within one cycle of vibration with frequency *f*. Vertical axis shows multiple data sets taken for reproducibility. Sample matrices are included in Appendix A.

3.2.4. Optical Coherence Tomography and nanoindentation

To support measurements made with the digital holography setup, an OCT, Thorlabs, Tel-321 [57], and nanoindenter, Optics-11, Chiaro [58], are used as supplementary tools.

The OCT has the capability to image geometry of tissues in 3D as well as movement of tissues in 2D through doppler acquisition mode. A summary of its capabilities is shown below in Table 1. In this Thesis the OCT is used primarily to verify the thicknesses of layers of the tissue. This identifies some unknowns that can be fed to the machine learning algorithm to increase accuracy.

Table 1 Specifications of the OCT used in this work [60].

Wavelength	1300 nm
Max 2D FOV	1.4 cm
Max 3D FOV	1 cm × 1 cm
Sampling rate	146 kHz
Max depth in air	3.5 mm
Resolution in air	5.5 um

The nanoindentation in this Thesis is used to identify stiffness values of tissues using the JKR model [59]. For each measurement, a hole is cut in the packaging of the desired sample to limit tissue exposure to typically drier environmental air. The tissue is measured in 4 locations to measure an average and standard deviation.

Table 2 Specifications of the nanoindenter used in this work [61].

Probe force range	20 pN – 2 mN
Stiffness range	5 Pa – 1 GPa
Indentation stroke	Up to 100 μm
Probe radius	Approx. 50 μm
Test environments	Air or liquid
Experimental speed	~ 10 μm /s
Experimental depth	~ 50 μm

3.2.5. Finite element (FE) simulation and Machine Learning (ML) integration

The machine learning integration requires two steps: training and prediction. The training step requires generating and using as much data as is feasible as larger amounts of data typically increase accuracy of classification. This can be done by measuring many samples and recording all necessary input information, which is time consuming and is not always possible given the expensive nature of bioengineered tissue prototypes. Instead, an FEA simulation is used to generate many data points across a range of possible inputs.

To create an FEA simulation an FE model is created as in Fig. 26. Geometry and boundary conditions are reproduced and material properties including stiffness, density, and Poisson's ratio. For layered structures, these material properties are reproduced for each layer. To generate large amounts of data a parametric study is performed in which the study is performed multiple times. The stiffness, in addition to other variable properties, is changed within each run of the study so that models are produced representing the range of values expected of the real sample. In this way the ML algorithm is trained to classify each type of model expected to occur within the sample.

The study performed is a modal analysis which outputs mode shapes and frequencies for each model.

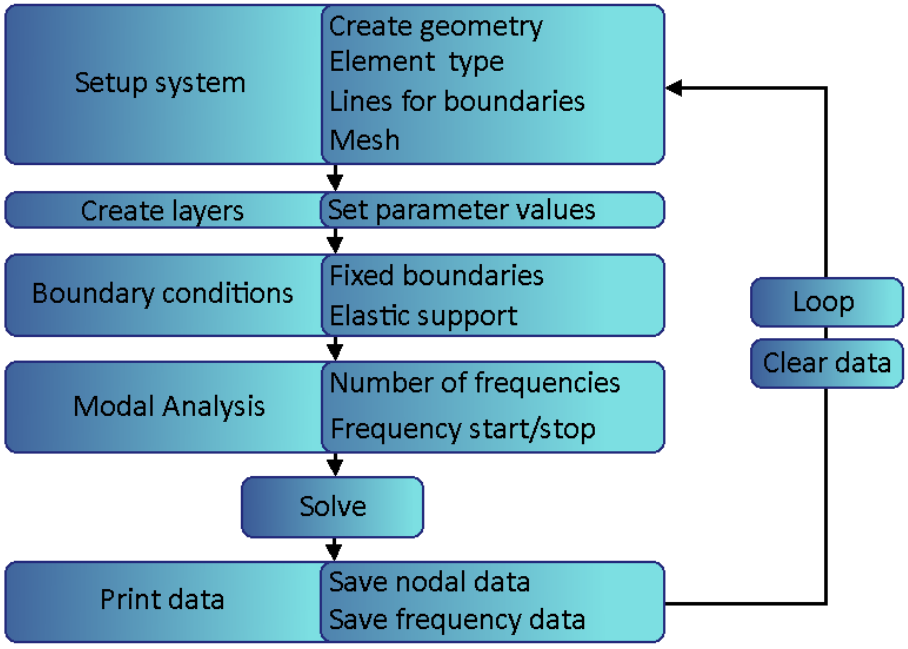

Fig. 26 Critical steps to create the parametric FE simulation.

A neural network deep learning algorithm then classifies the properties input by this parametric FE analysis and predicts the properties for future data sets. This can then be fed real data to train the algorithm to connect the simulated classifications to real data. At this point the algorithm is ready to predict the mechanical properties with a reduced input.

3.3. Validation of DHV

Several validation tests were performed to determine if the DHV system performed as expected. The laser strobing, the microphone, and the speaker were all assessed by secondary

equipment as is discussed in this Section. Finally, the total system was validated using a cantilever beam to compare measurements of the holographic sensor to the measurements made by an LDV.

3.3.1. Strobing of AOM

The primary component with a critical effect on strobing is the AOM integrated into the laser. The effectiveness was validated by measuring the strobe signal sent into the AOM to the laser intensity output after the AOM. A high speed photosensor measured the laser intensity after strobing, which was overlaid by an oscilloscope, Liquid Instruments, Moku:Lab [60] onto the original strobe signal, Fig. 27.

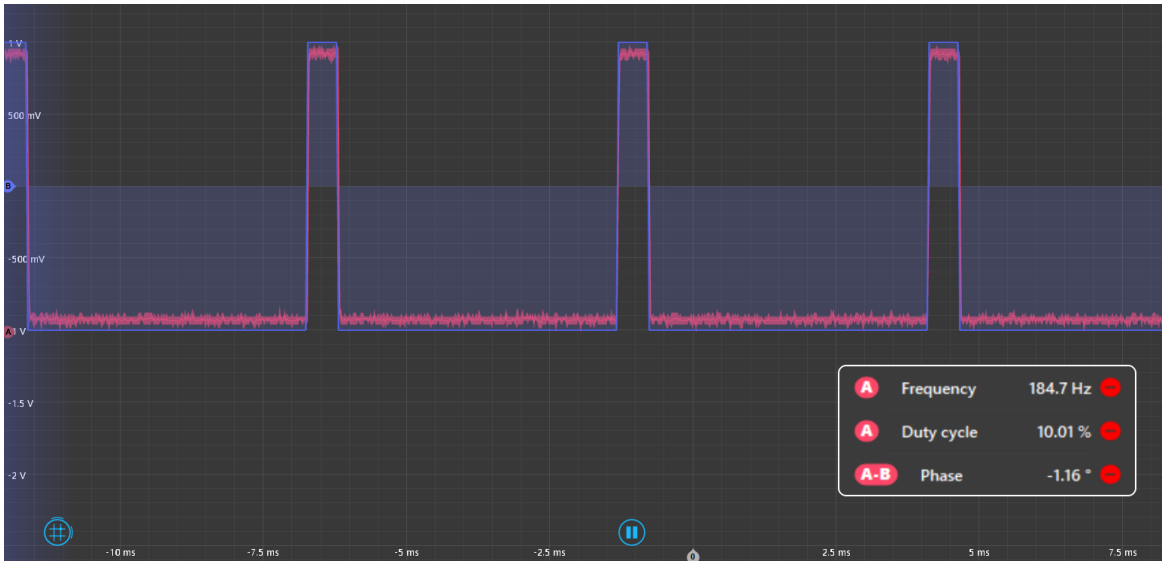

Fig. 27 Oscilloscope data showing AOM strobe input (blue) and the laser output (red) operating at the frequency of 184.4 Hz.

The difference between the strobing input and the laser output is dependent on the desired frequency. When set to 184.4 Hz, Fig. 27, the phase difference was -1.16° but at 1kHz, Fig. 28, the phase increased to -6.49° and the duty cycle decreased from 10% as input down to 9.7%. This

difference is miniscule, as at 194.4 Hz, the phase difference corresponds to 17µs, and at 1kHz the phase difference corresponds to 18µs. Furthermore, the duty cycle decrease of 0.3% relates to 30 µs when the period is 1ms. This relates to a 3% decrease to the effective light intensity leaving the laser, which may be significant for a sample that reflects only a little light and thus requires a higher camera exposure.

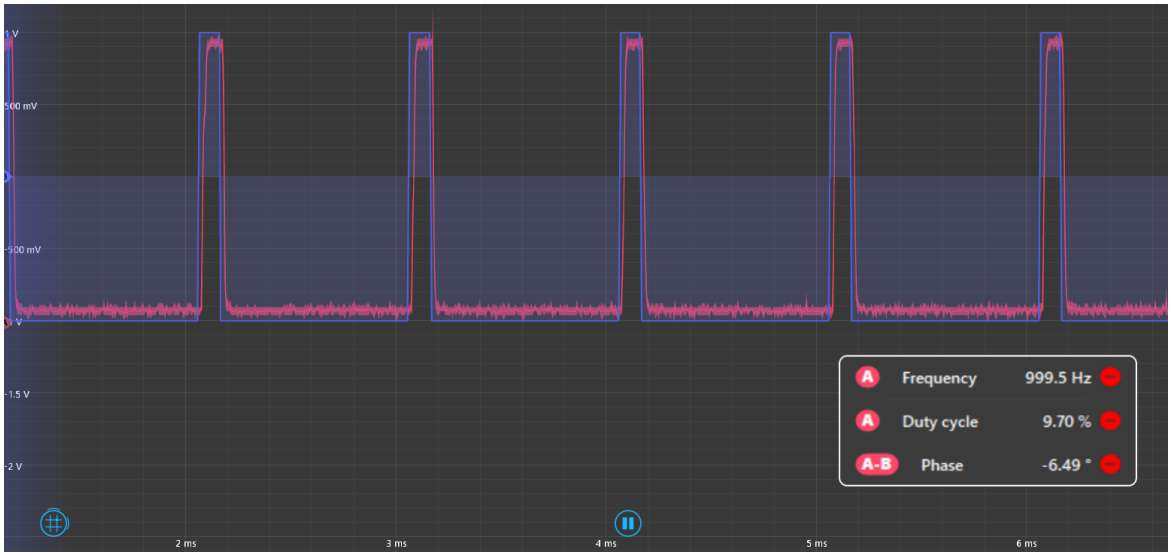

Fig. 28 Oscilloscope data showing AOM strobe input (blue) and the laser output (red) operating at the frequency of 1 kHz.

Ultimately this strobing is validated for the presented methods. Measurement of vibrating tissues using DHV in this thesis demonstrate critical vibrational patterns at lower frequencies not surpassing 500 Hz. At this range, the strobing phase offset is small and found to be unlikely to have a noticeable effect on the measurement. At higher frequencies, should DHV analysis be expanded to higher frequency ranges, the phase offset is larger. The loss of light from the reduced duty cycle can be supplemented by an increased camera exposure time. Further, it is found that the

phase offset of the AOM strobing is consistent, so imaged points will maintain a similar phase difference relative to the vibration. Thus this phase offset will not modify the quality of data.

3.3.2. Microphone

The microphone validation was conducted via calibration to an external device and confirmation of frequency measurement. When measuring the frequency, the microphone outputs a sine wave with a voltage that has an amplitude related to the sound pressure. The peak to peak (*PTP*) value of this sine wave is multiplied in Eq. 24.

$$\mathrm{dB}_{\mathrm{raw}} = 20 * \log\left(\frac{\mathrm{PTP}}{\mathrm{tf}}\right) \tag{24}$$

Where *tf* is the transfer factor of the microphone as reported by the manufacturer. This outputs the raw uncalibrated decibel level. Several different frequencies and speaker volumes were recorded by the microphone and a decibel reader in a calibrated microphone. The linear regression was formed, Fig. 29, and all decibel values are multiplied by the line of best fit to produce a calibrated decibel level.

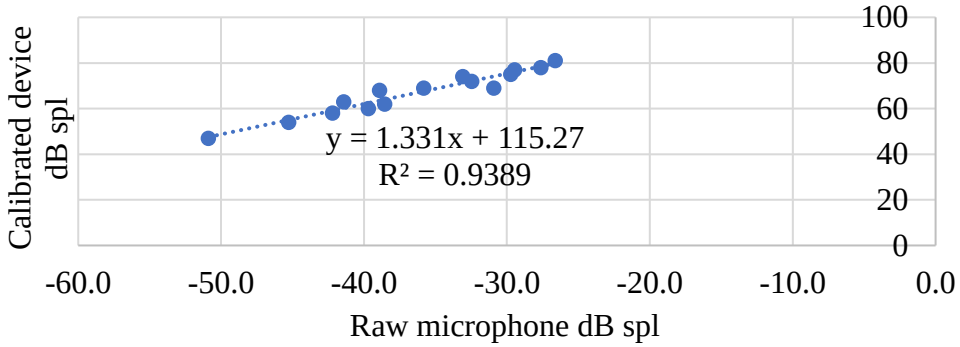

Fig. 29 Calibration of microphone used to determine acoustical pressure reaching the sample. Calibrated microphone reading as a function of measured microphone signal is represented with a linear model.

This decibel level is then converted to a pressure according to Eq. 24, with a reference pressure of $2x10^{-5}$ as this reference pressure is the standard reference related to human hearing as is used for the calibration microphone. The standard deviation of the microphone reading was measured by repeating measurements multiple times at different frequencies and pressures and finding the average and standard deviation at each. The standard deviation of the voltage peak to peak value was found to be 0.99 mV, but this is converted to pressure through several log functions so a curve was found to relate the voltage reading to the standard deviation of the pressure. This was done by taking several voltage measurements, adding, and subtracting the voltage deviation converting these values to pressure, then finding the deviation of the two pressure values from the original. The corresponding standard deviation curve is shown in Fig. 30.

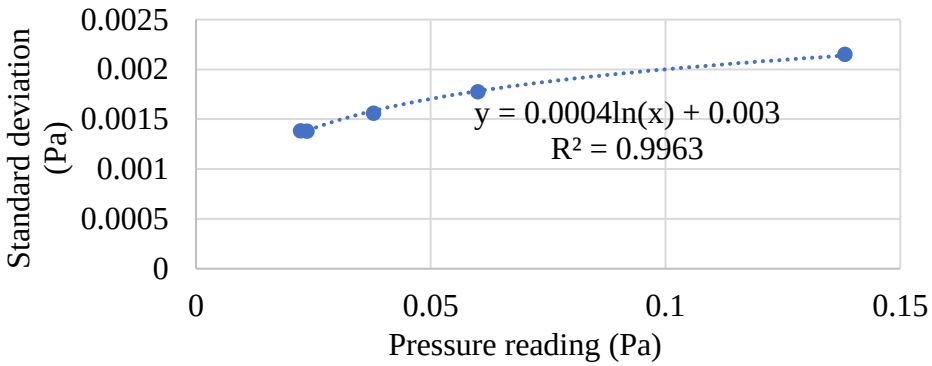

Fig. 30 Determination of standard deviation of microphone used to determine acoustical pressure. Standard deviation as a function of calibrated pressure is presented by a natural log model.

It was then noted that for the application of this microphone to in-package bioengineered tissues, the desired sound pressure has to be recorded inside of a package which creates a higher sound pressure than outside of the package. However, for the method to remain non-invasive, the microphone must remain on the outside of the package, so a secondary calibration was performed in which the relation of interior to exterior pressure was calculated. For such applications, the

microphone can then be placed outside of the package and when multiplied by the line of best fit, Fig. 31, calculate the corresponding pressure inside of the package.

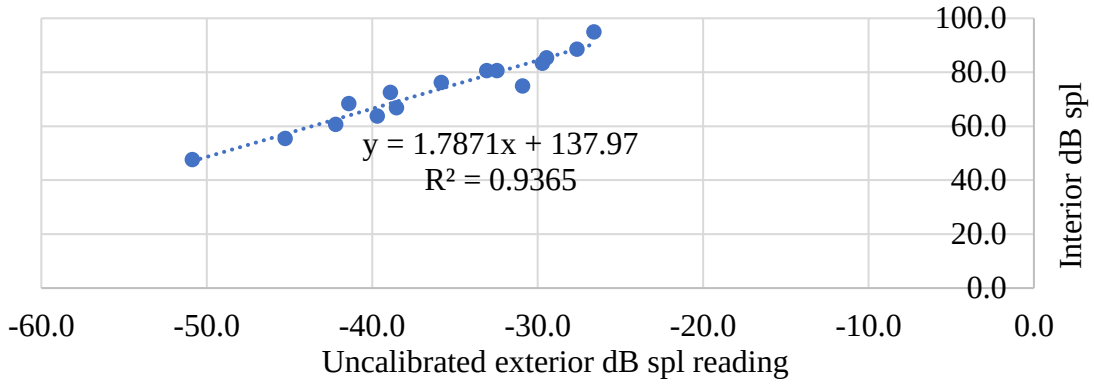

Fig. 31 Calibration of microphone used to determine acoustical pressure reaching the sample inside of packaging. Final calibrated microphone reading inside the package as a function of measured microphone signal outside of the package is represented with a linear model. The package is a hollow plastic container characteristic of one used for cell growth.

3.3.3. Speaker

The primary component of the speaker that needed to be validated was the single tone frequency output. To do this a microphone was placed under the speaker and its output was measured by a spectrum analyzer. At most frequencies, some harmonics were noted in which a frequency was detected at the input frequency but also whole multiples of that frequency. Figure 32 shows two measurements for 180 Hz, with notable peaks at 180, 360, 540, etc. It is important to note the magnitude of these frequencies, however. As more voltage is added to the speaker, the volume and sound pressure increase, and so does the prominence of the harmonics. At 2V, the difference in the main frequency and the first harmonic is 30 decibels/mW (dBm) while at 1V the difference is 42 dBm. It is important to note the decibel readings have not gone through the calibration step for this measurement, so this is a raw signal difference. A difference of 6 decibels

results in double the sound pressure, so a difference of 30 decibels has a 32 times weaker harmonic pressure and a difference of 42 decibels has a corresponding 128 times weaker harmonic pressure.

Fig. 32 Speaker's frequency FFT at 180 Hz at 2V and 1 V with 18x averaging.

Also of note is that both measurements in Fig. 33 have averaging performed to the spectrum measurements. Figure 33 shows a similar measurement at 150 Hz and 0.3 mV, corresponding to 22.3 ± 1.4 mPa, with no averaging. At low volumes, typically occurring around 40 mPa, the harmonics become negligible. Simultaneously, when no averaging is performed, most harmonics appear as random noise.

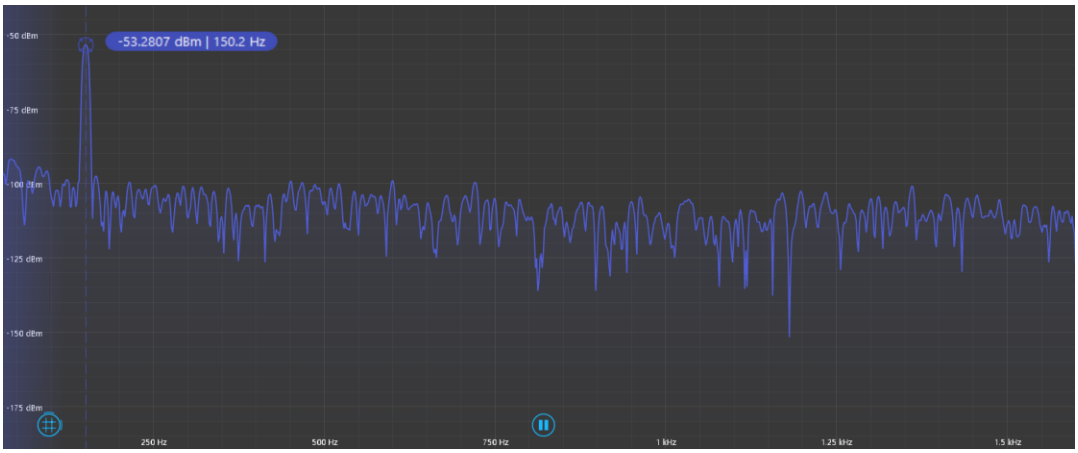

Fig. 33 Speaker's frequency FFT at 150 Hz at 0.3 V with no averaging.

All together the presence of harmonics created by the speaker are minimal and should not have the ability to affect the sample in any meaningful way. Lower voltage inputs to the speaker produce cleaner frequency outputs, but for any frequency and voltage input that is sufficiently small, the applied acoustical force to the sample can be assumed to be single tone.

3.3.4. Digital holography vibrometry (DHV) validation

A validation test was performed using the DHV sensor. It was determined that the critical part of DHV that needed to be validated was the optical measuring methodology that used digital holography. If this part was found to work as expected, then its measurements would validate the vibrometry component on a real tissue, as is discussed in the next Section. Thus, a suitable component was found to validate the system using a cantilever beam, Fig. 34.

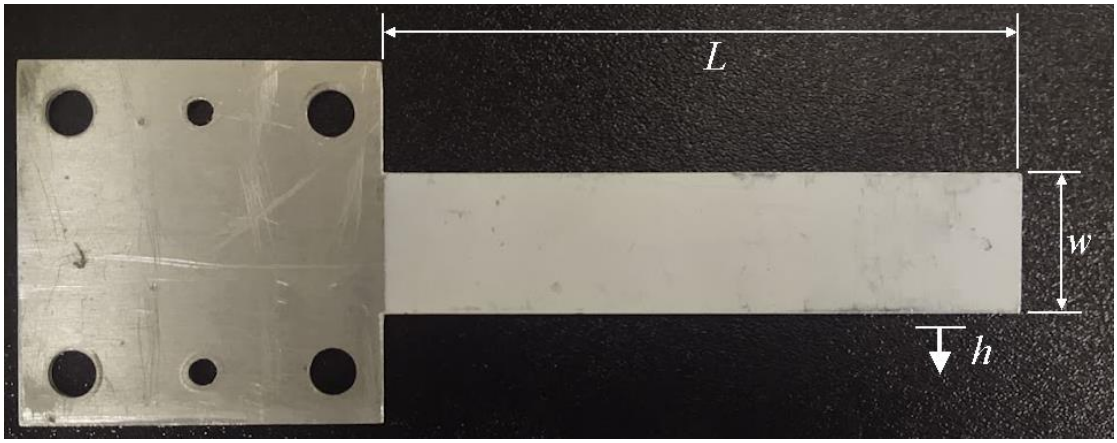

Fig. 34 Cantilever beam with dimensions used for validation of holographic measurements. *L* is the active length of 90 mm, *w* is the width of 20 mm, and *h* is the height of 2 mm.

The cantilever beam was attached to a shaker that can vibrate the beam at high frequencies, then suspended within the measurement area of the setup via a post attached to a magnetic base, Fig. 35. Previous work performed within the CHSLT lab used such cantilever beams to verify holographic methods [61] and the mathematical analysis of a vibrating cantilever beam is simple, thus it makes an ideal verification object. A frequency sweep was performed with the shaker and digital holography setup until mode shapes were identified. The frequencies of the identified 2nd and 3rd bending moment and 1st and 2nd torque moment were noted and the beams vibration was measured at the 2nd bending moment.

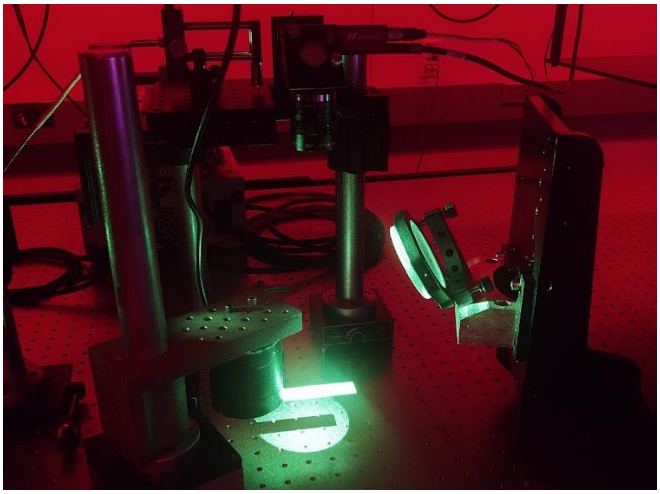

Fig. 35 Cantilever beam being tested in DHV.

The vibration of a beam is determined by a simple equation which relates the frequency of vibration [62], the stiffness, and several geometrical parameters as shown in Eq. 25

$$f_n = \frac{{\omega_n}^2}{2\pi}\sqrt{\frac{EI}{mL^4}} \tag{25}$$

Here E is young's modulus of the material, I is the bending moment, L is the length and m is the mass per unit length. The symbol ω_n is a constant related to which mode the relevant frequency is at. For the first, second and third modes, this constant is 1.875, 4.694, and 7.854. For a beam of thickness h, length L, and width w, the moment for a beam is

$$I = \frac{wh^3}{12} \tag{26}$$

And the mass per unit length is

$$m = \rho wh \tag{27}$$

Where ρ is the density of the material. Altogether, the frequency can be determined by a simplified equation

$$f_n = \frac{{\omega_n}^2}{2\pi}\sqrt{\frac{Eh^2}{12\rho L^4}} \tag{28}$$

The cantilever beam measured had a length, width, and thickness of 0.09, 0.02, and 0.002 meters respectively. It was made of aluminum, so material properties can vary widely but will be estimate to be around 6.9×10^{10} Pa for E, and 2700 kg/m^3 for ρ [63]. Thus, for the second bending moment, the predicted frequency is 1.264 kHz. Experimentally, this frequency was found at 1.217 kHz, which is a relative error of 3.7%. For the second mode, the predicted frequency is 3.566 kHz, and the experimentally determined frequency is 3.422 kHz with a relative error of 4.0%. This indicates the DHV system has the ability to locate modes and that the measured values are the vibration of the cantilever beam. The aluminum cantilever beam can have a range of values and the engineering database used to find the stiffness reported a normal range of $6.9 \times 10^{10} - 7.5 \times 10^{10}$ Pa, and even this assumes the beam is pure aluminum and not an alloy. Thus, the low relative error is excellent given that the used stiffness was arbitrarily chosen from a range of possibilities.

Further validation was taken using a laser doppler vibrometry (LDV) system, Polytec, Vibroflex [64]. The second bending moment of the beam was measured with the digital holographic setup at 12 points in the vibration cycle of the beam and unwrapped to find the displacement. The cantilever did not fit in the full display of the camera and 1.7 cm were not visible, so the displacement of the beam measured by holography was fit to 2nd order polynomial and zeroed such that the true displacement of the tip of the beam was known. The maximum velocity of the beam was then calculated by finding the displacement in-between each set of images and dividing the period by 12 to find the time in-between each set of images. The beam was then removed from the holographic setup and the probe-arm of the LDV was placed over the tip of the beam, Fig. 36.

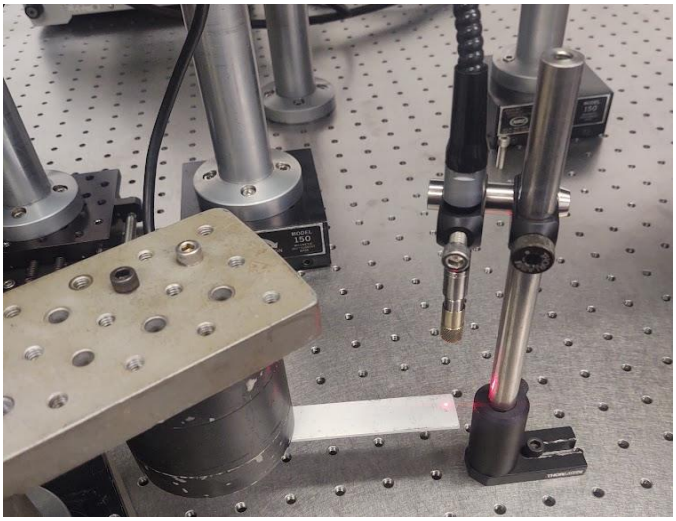

Fig. 36 Cantilever beam as measured by the probe-arm of the LDV.

The beam was set to vibrate at the same exact frequency and shaker amplitude, and the velocity measurement of the LDV was recorded. The holography and LDV measurements are shown below in table 2. Thus, the LDV validates the holographic measurements made by the DHV sensor.

Table 3 Maximum velocity measurements of the cantilever beam by DHV and LDV. The relative error is mostly due to alignment of the LDV, and the resolution of the oscilloscope used in the DHV.

	Holography	LDV	Relative error
Maximum velocity	12.2 mm/s	12.3 mm/s	0.5%

4. Application

The overall goal of this Thesis is to create a tool and methodology that can measure the mechanical properties of a bioengineered tissue. The tool has been created and it is demonstrated to work on a vibrating cantilever beam. This Section discusses the application of the tool to two bioengineered tissues: Apligraf and ligaments. Apligraf is a bioengineered skin tissue created by Organogenesis Inc. [65]. The ligament in question is a bone-on-bone ligament. However, the process for this is less developed and this Section only discusses the proof of concept applied to a ligament-like string.

4.1. Apligraf

Apligraf is a bioengineered tissues created by Organogenesis, Fig. 37. It is one of the first FDA approved tissue engineered products with live cells and is still within common use for treatment of venous ulcers. The Apligraf used in this research is manufactured by Organogenesis Inc. As part of the cost sharing funding of this research, Apligraf produced in excess of demand is provided to this lab upon request. Due to this ease of access to Apligraf, it stands as the primary initial application for this research. This Section discusses its construction as well as methodology and results related to application of the DHV sensor to the Apligraf.

The presented methodologies were applied to Apligraf as shown in Fig. 38. OCT, Nanoindentation, and DHV were used to perform several experiments. These established capabilities and limitations of the DHV method as applied to Apligraf. FEA models were made to imitate Apligraf to train the ML neural network. Future work will integrate the neural network with actual measurements.

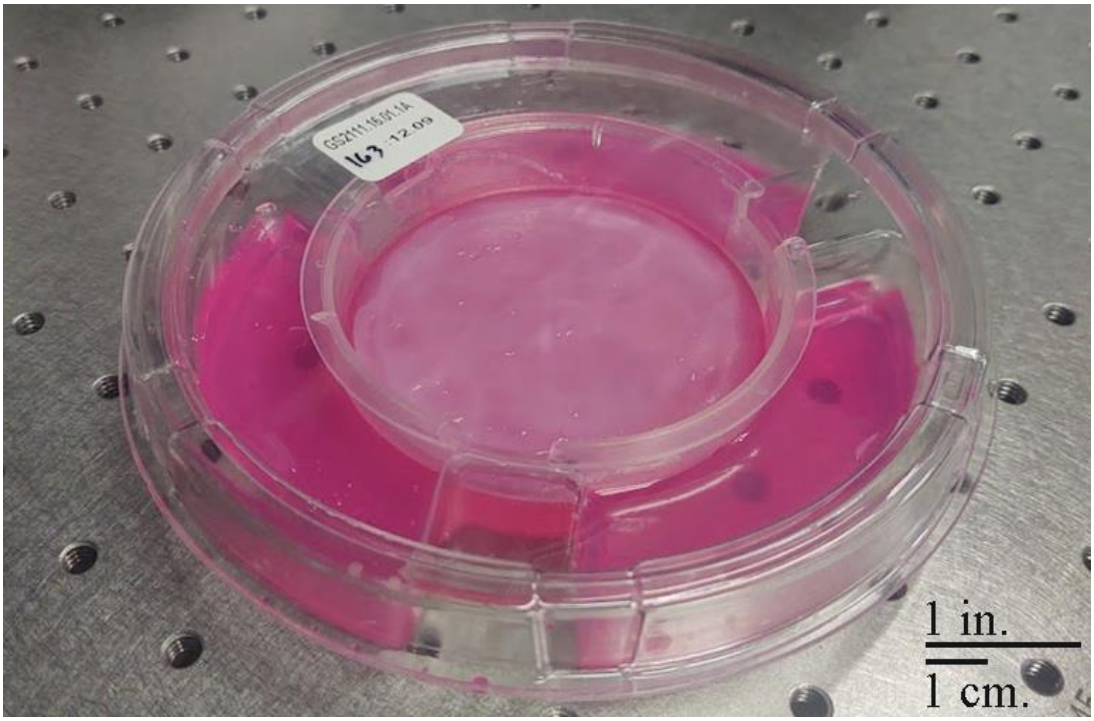

Fig. 37 Apligraf in its packaging. The pink substrate is the agar that hydrates and nourishes the Apligraf while the white film appearing in the center is the Apligraf tissue.

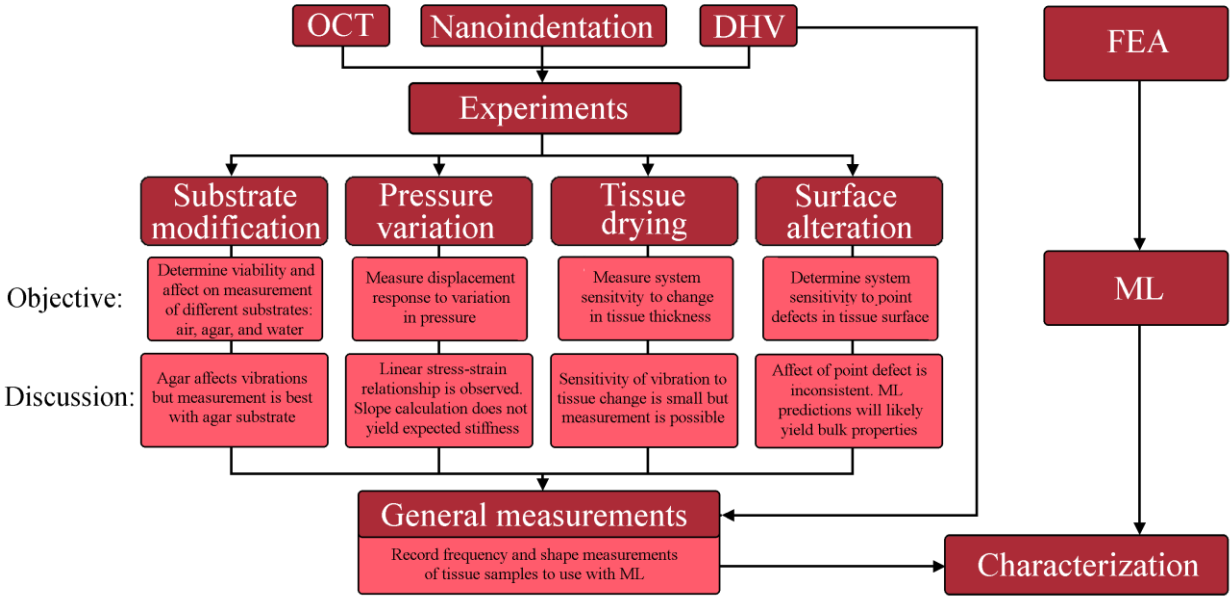

Fig. 38 Flowchart of methodologies and experiments performed for application of DHV and supporting methodologies to Apligraf.

4.1.1. Apligraf construction

Apligraf was created to be a living skin-substitute for application to surface wounds. Its cells are harvested from donated circumcisions. It works by being applied to an ulcer, where it provides some protection to the open wound and releases growth hormones that encourage the growth and healing of the native tissue around the wound. By the end of the healing process, none of the Apligraf tissue remains.

Skin has many layers and Apligraf does imitate this to some extent, Fig. 39. It has an epidermal and dermal layer, Fig. 40 but consists of only major cell types in these layers. The hypodermal layer below this as well as many of the other types of cells, such as glands, Langerhans cells, or dendritic cells are not present in Apligraf. The epidermis forms the outer layer of Apligraf and is made of human keratinocytes. The dermis forms the bottom layer of Apligraf and is made of human fibroblasts in a bovine type 1 collagen matrix [66].

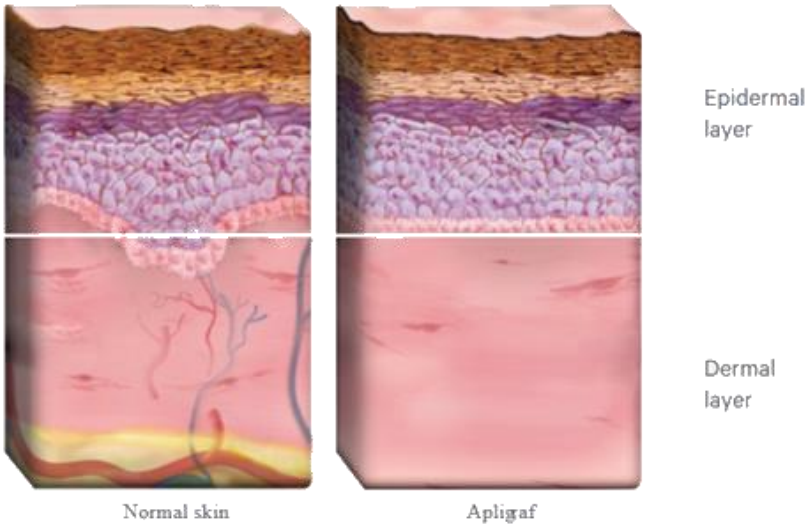

Fig. 39 Comparison of layers of normal skin and Apligraf [67].

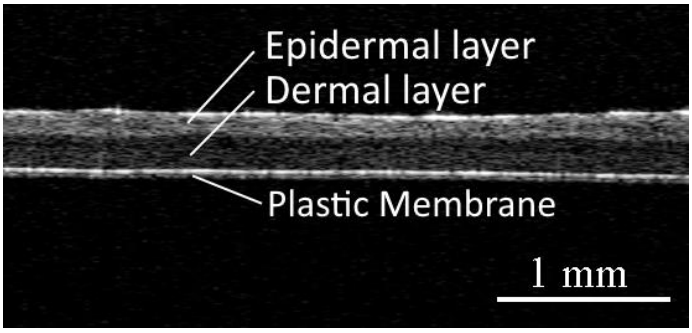

Fig. 40 OCT image showing layers in Apligraf.

Apligraf is produced by seeding dermal fibroblasts into a bovine type-1 collagen matrix. This grows in liquid growth media and shrinks as the cells remodel the matrix. Keratinocytes are then seeded across the top layer of the tissue to form the epidermal layer. When they have spread to cover the entire surface, the liquid media is removed from the top of the tissue, remaining underneath, leaving a liquid-air interface at the same level as the tissue. When the tissue is done growing, after a total of around 2 weeks, the liquid is removed and replaced with agar for packaging.

The component of Apligraf that is delivered in a package forms a thin disc with a radius averaging about 3.75 cm. This sits on top of a plastic membrane with a thickness of 20 μm. This tissue and plastic assembly, Fig. 41, is hereby called the transwell disc. This sits on top of an agar bed that is approximately 1 cm in thickness.

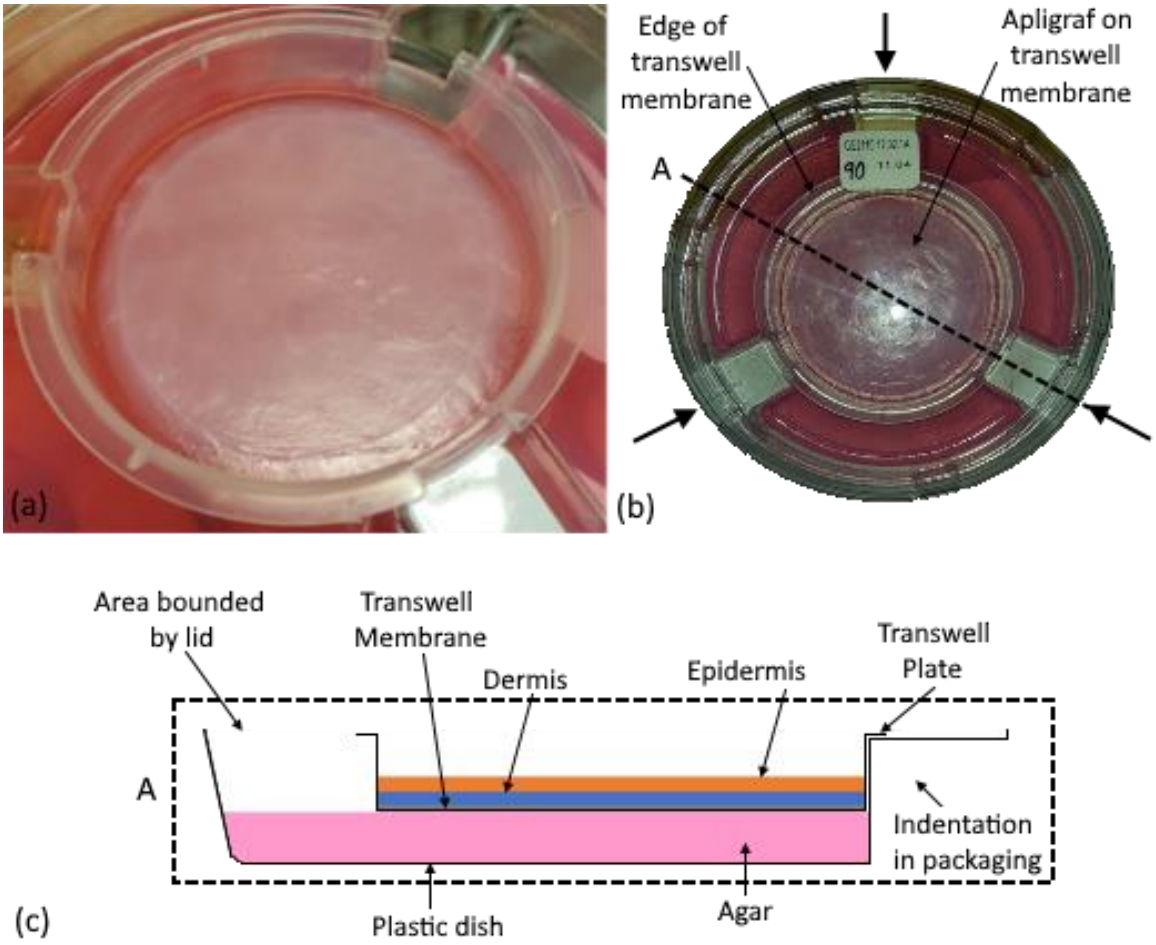

Fig. 41 Apligraf packaging: (a) transwell plate with Apligraf; (b) entire package with arrows indicating three characteristic indents; (c) cross section area, A, of entire package with labels indicating critical components.

As can be seen in Fig. 41, the packaging has a distinct formation of 3 indentations upon which a lip on the top of the transwell disc rests. This entire assembly then in turn has a lid placed on top which can be easily removed. It is important that this lid remains on the packaging at all times as it allows for retention of moisture so that the tissue does not dry out.

4.1.1. Theory and simulation

As Apligraf forms a circular disc, its vibration should primarily display characteristics in line with circular plate theory (CPT). A thin plate which has a radius that is much larger than its thickness vibrates harmonically at frequencies dependent on its physical properties. Analytically, the vibration of the thin tissue should follow principles of CPT, though the CPT models assume particular boundary conditions, normally with free upper and lower surfaces As such, Eq. 29 presents the displacement, *w*, of a thin plate [23].

$$D\nabla^4 w + \rho \frac{\partial^2 w}{\partial t^2} = 0 \tag{29}$$

For free vibrations,

$$w = W cos\omega t \tag{30}$$

Where *w* is the transverse displacement, *W* is a function of position coordinates and ω is the circular frequency. Or for complex displacements [68],

$$w(r, \varphi, t) = W(r, \varphi) e^{i\omega t} \tag{31}$$

These equations yield a position function as in Eq. 32,

$$W(r, \varphi) = \sum_{m=0}^{\infty} \left\{ A_m J_m \left(\lambda \frac{r}{a} \right) + C_m I_m \left(\lambda \frac{r}{a} \right) \right\} \begin{Bmatrix} cos\, m\varphi \\ sin\, m\varphi \end{Bmatrix} \tag{32}$$

where,

$$\lambda^2 = \omega a^2 \sqrt{\frac{\rho}{D}} \tag{33}$$

ω is the natural frequency, in radians, and *a* is the radius of the plate. and D is the flexular rigidity coefficient determined by:

$$D = \frac{Eh^3}{12(1-\nu^2)} \tag{34}$$

Thus, through the flexular rigidity, the vibrational frequency is related to the mechanical properties. For example, for the fundamental mode of the 0^{th} order, which is the first mode to naturally occur and generally the most prominently assessed, $\lambda^2 = 4.977$ [69] as calculated for a plate with Poisson's ratio of 0.3. For the second mode it equals 13.94.

To calculate the stiffness of the Apligraf tissue, the density is assumed to be constant around 997 kg/m^3 and Poisson's ratio to hold around 0.48 [70], as these are values that are adopted estimates for engineered tissues as they are primarily water. Using measured data in which the fundamental mode was measured at 147 Hz, assuming a thickness of 400 μm, the calculated modulus is 203 GPa. This value is unreasonably high as indentation of Apligraf typically yields a stiffness between 20 and 40 kPa for the epidermal layer. Clearly, the constants and boundary conditions used for this analytical model do not perform under the complex, multilayer, viscoelastic system presented by Apligraf, thus a computational model incorporating the layered structure shown in Fig. 41c is required to extract more reasonable estimates of the mechanical properties.

The real tissue is a multilayered structure whereas CPT assumes a single layer of homogenous properties. This problem is made more complex with the consideration of the mechanical properties of the tissues. A simple sandwich model [71] can describe a multilayered structure, but the approximate stiffness of the epidermis is 36 kPa +/- 26 kPa, the approximate stiffness of the dermis is 26+/- 4 kPa, and the approximate stiffness of the plastic membrane is 2.3 MPa. The large disparity of the modulus between the tissue layers and the plastic layer, which is also vibrating suggests that a more accurate model is one which accounts for the vibration of the plastic membrane, dampened by the tissue layers. Analytical estimation of this model could serve as its own Thesis and would thus require a considerable amount of time to expand this method to

other types of tissues or packaging in the future. This Thesis thus seeks to use machine learning to estimate the mechanical properties such that a perfect analytical model is not required for every new tissue.

To train a machine learning algorithm, a model was created in Ansys APDL as guided by the flowchart in Fig. 26 and detailed in Appendix B. This model is a circle of 3.75 cm radius that uses thin shell elements. Each element has three layers, one for the epidermis, one for the dermis, and one for the plastic. The properties of each layer are shown in Table 4, where *par.* indicates a parameterized value. To imitate the agar properties, an elastic support [72] was added to the bottom of the entire layer. The result is a fundamental mode shape expected of 0^{th} order vibration of circular plates shown in Fig. 42a.

Table 4 Parameters of each layer input for FEA simulation.

	Poisson's Ratio	Density	Stiffness	Thickness
Epidermis	0.48	997	*par.*	*par.*
Dermis	0.48	997	*par.*	*par.*
Plastic	0.33	1000	2.3 MPa	20 μm

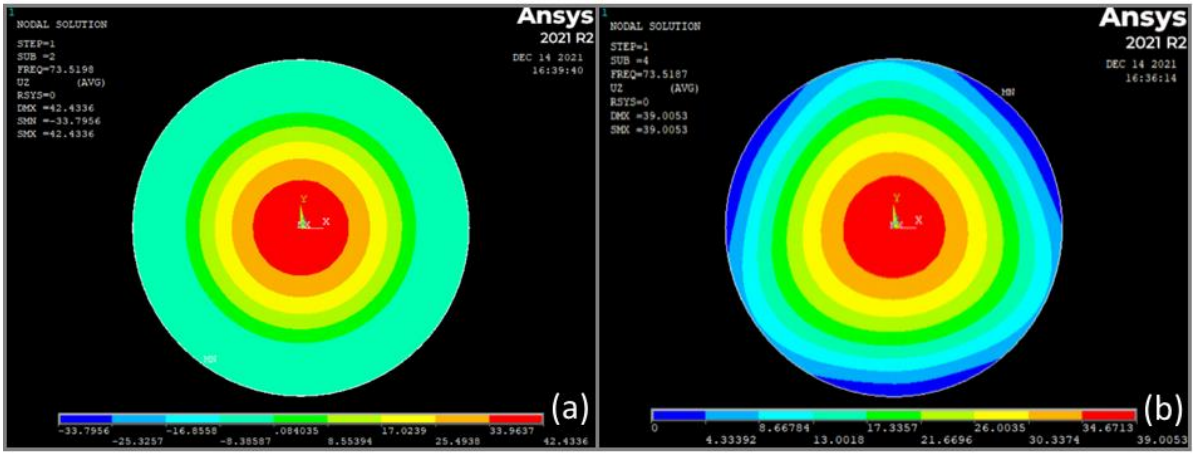

Fig. 42 FEA images of fundamental modes: (a) completely free boundary conditions; (b) fixed boundary conditions in 3 segments each encompassing 30 degree arcs.

Experimentally it has been determined that the real vibration measurement does not perfectly match the circular vibration patterns. Instead, there is a distinct triangular pattern present, Fig. 43, which is most notable in the fundamental mode. Figure 43 shows a time average image and double exposure image of the system vibrating in its fundamental mode. In this image, the packaging has been rotated relative to the camera, indicated by the position of a screwdriver marked with white arrows. As the triangular pattern rotates with the packaging, it must be concluded that the triangular pattern has resulted from the 3 notches in the packaging.

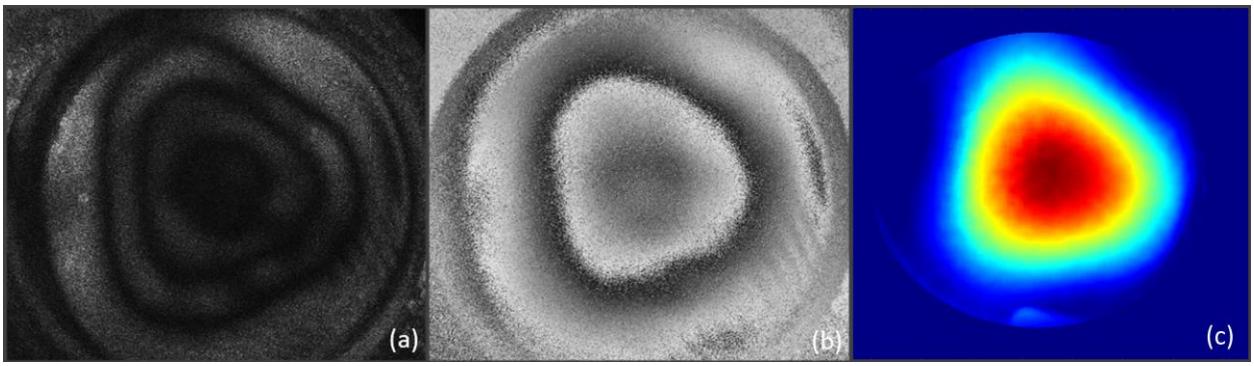

Fig. 43 DHV measured images of the fundamental mode of vibration in Apligraf: (a) Time average image; (b) double exposure images; (c) displacement heat map after unwrapping.

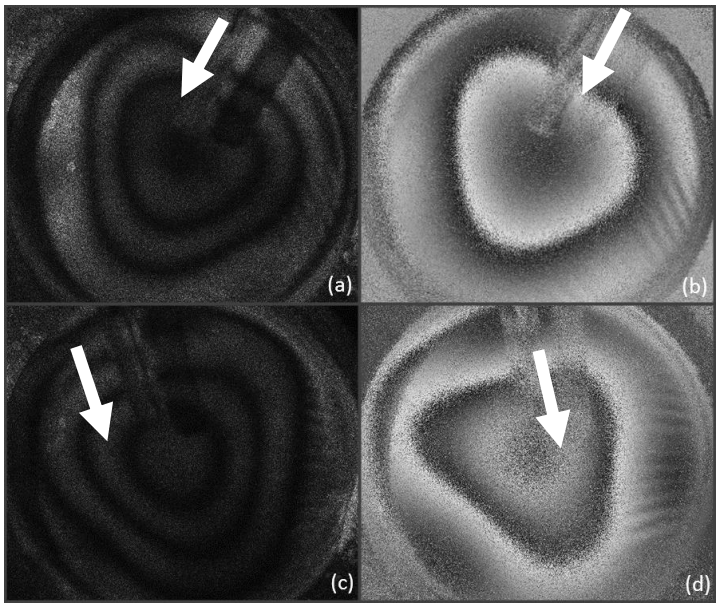

Fig. 44 Time average and double exposure images of fringes with 2 different rotations of the packaging. A screwdriver, marked with a white arrow, indicates a common point on the packaging.

These notches encompass 30-degree angles, so the simulation boundary conditions were modified such that the simulation now outputs images with a more triangular shape like in Fig. 44. To do this, fixed boundary conditions were applied in three 30-degree segments where the Apligraf packaging's indents are located. The boundary conditions, layers, and mesh are shown in Fig. 45.

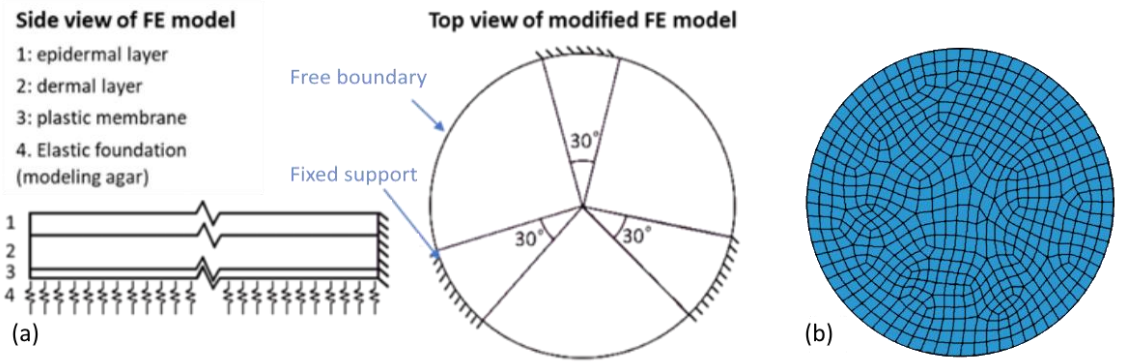

Fig. 45 FE model schematics: (a) Geometrical characterization (b) Mesh pattern

A modal study was conducted in which the natural vibration was calculated. The vibrational pattern and frequencies of each calculated mode were saved. Then one parameter value was changed, and the simulation was conducted again. This way all combinations of the values within selected ranges, table 5, for the epidermis and dermis stiffness and thickness were modeled. This data was then passed to Ziyang Gao, a PhD candidate from the Korkin lab, for training the machine learning algorithm. Specific methodology related to machine learning is discussed in Section 4.1.4.

Table 5 Parameterization of epidermis and dermis thickness for FEA simulation

	Stiffness (kPa)	Step (kPa)	Thickness (μm)	Step (μm)
Epidermis	20-60	5	50-200	50
Dermis	2-20	3	50-200	50

4.1.2. Apligraf metrology

The Apligraf is imaged by the DHV sensor by placing it on the optical table below the camera. A variety of clamping methods have been used to hold the Apligraf sample in place through the development of this DHV tool. The development of these clamps is the result of an attempt to increase the stability of the tissue and reduce environmental vibrations. All original clamps were 3D printed, with a final variation machined from aluminum, Fig. 46. The speaker is suspended just above the sample. As the sample vibrates from the speaker, it is imaged by the DHV sensor and files are saved as LVvid video files. A MATLAB program reads the LVvid files and creates 12 complex images. These are unwrapped by the Goldstein algorithm and then converted to point clouds. These point clouds have a real *x*-y scale, and the *z* scale has also been modified to the correct values for 432 nm light.

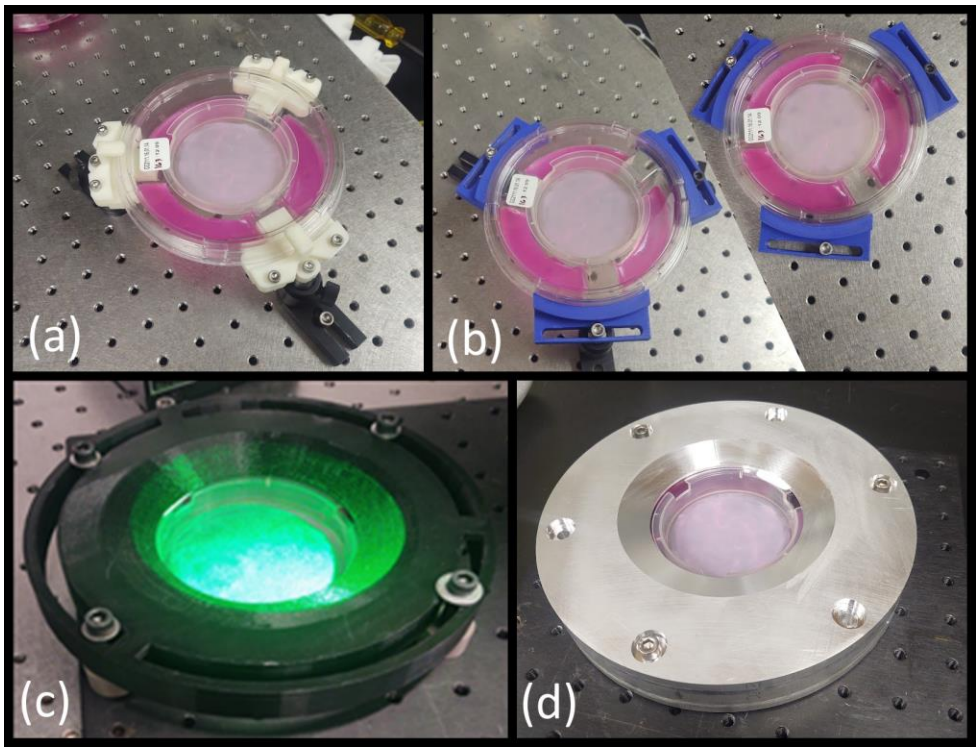

Fig. 46 Clamps developed to hold the Apligraf tissue to the table in chronological order. Each set of clamps reduced environmental vibrations and increase reliability of the clamping process: (a) 3-point pronged clamps using screwed attachments on the top to hold lid down; (b) 3-point clamps holding the top and bottom of the package together along the arc where they meet; (c) full-radius clamp screwed into movable breadboard; and (d) full-radius metal clamp with top and bottom component. Bottom component is not removed for each sample, increasing reliability of sample placement. All samples shown are still in their original packaging.

4.1.3. Experiments

Experiments were developed to establish whether the system can measure vibration dependent on the properties of the tissue, whether the system can measure the full field-of-view as sections of tissue with various properties rather than a homogeneous membrane, and what the limitations of measurement are. From this comes the goal to determine the mechanical properties or confirm that such determination requires more than just experimental measurements. The following experiments establish that the DHV sensor is able to measure the vibration of Apligraf tissue.

The first necessary experiment towards any new object is to establish that a measurement can be made. It was first established that using the speaker induced fringes at various frequencies in the Apligraf tissue. These fringes appear at a variety of locations but often appear in chaotic and ununiform patterns from which no useful meaning and no consistency can be drawn. At certain frequencies patterns consistent with modes of vibration for circular plates appear. This established that DHV is both inducing and measuring deformations in the tissue. However, to be able to measure a maximum displacement and to make calculations easier, the 0^{th} order is optimal as these modes contain a maximum displacement ideally in the center of the sample.

All samples were measured at room temperature to prevent condensation on the lid as it interferes with measurement capabilities, and all measurements were performed with as little removal of the lid as possible. Ideally samples were taken out of the bag in which they were delivered and immediately measured, but some experiments required modification of the surface which required opening the lid.

4.1.3.1. Frequency variation

The first important assurance is that the DHV measurements can detect changes to the sample. The first way to do this is to see if there is consistency between samples. According to contacts from Organogenesis, samples produced with the same batch should have similar properties as they are grown from the same set of cells with the same times, methods, growth media, etc. Thus, it is expected that many samples should have similar results, but individual samples should not grant identical results. Additionally, Apligraf tissues have been found to be sensitive to humidity and aging as a variation in either produces a change to both thickness and stiffness of the Apligraf. Thus, any variation to either of these changes the tissue slightly.

Such variations should not affect the plastic packaging, the plastic membrane in the transwell disc, or the agar. These components should also not vary significantly over time, barring the agar which could dry if left exposed for a very long time, though no experiments were performed at such an age. All changes to the modal frequency thus should be the result of changes to the tissue's physical and mechanical properties. Figure 47 shows 6 months of measured samples and frequencies of observed modes. Figure 48 shows the same but for the samples measured on air and not on agar, for which there is even less possibility of changes from a component other than the Apligraf tissue.

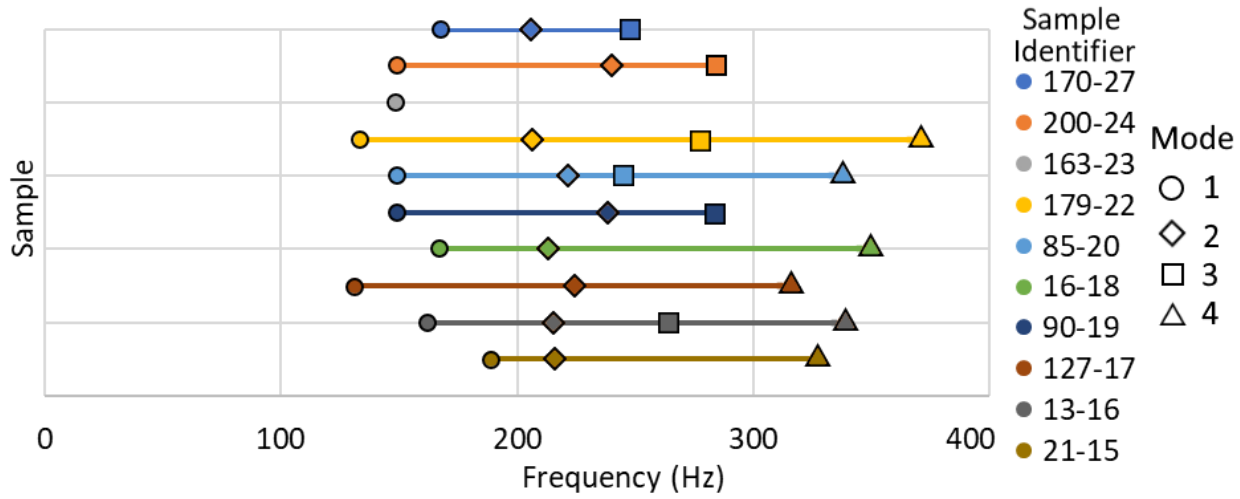

Fig. 47 Frequencies of observed modes for tissue samples resting on agar. Each point represents the location of another mode. Each sample may have modes missing.

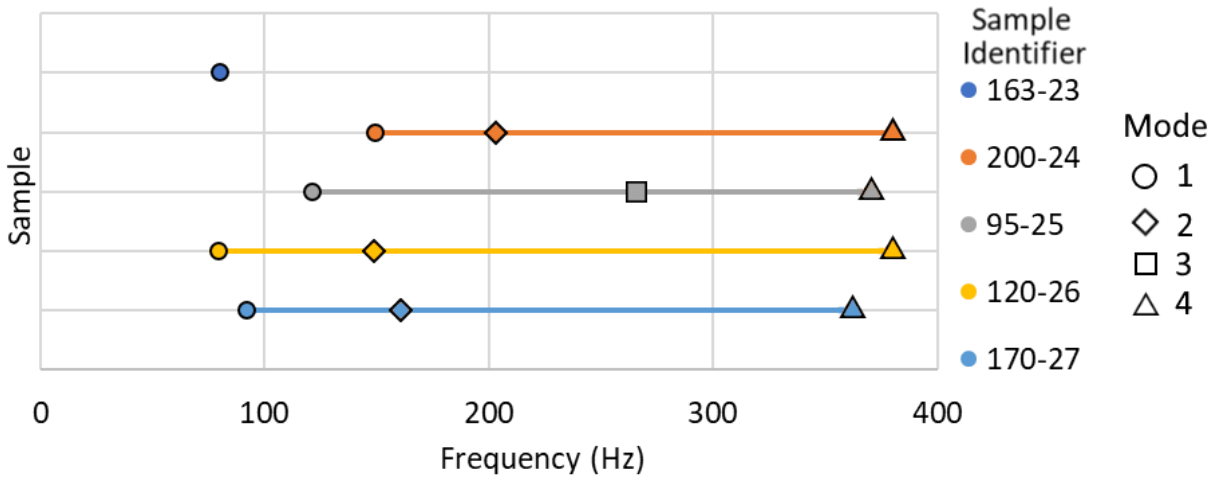

Fig. 48 Frequencies of observed modes for tissue samples surrounded by air with no agar. Each point represents the frequency of another mode.

If the DHV measurements were affected by properties of the plastic membrane or the Agar but not the tissue, there would not be this much variation between measurements of different samples as the properties of the agar and plastic will not change drastically between every package. While the agar itself could form with slightly different thicknesses for each sample, changes between samples were observed for the vibrations in which agar was not present. Thus, the DHV method does measure vibrations as affected by the tissue. This establishes that the DHV method does measure differences in the physical and mechanical properties of the tissues, as these properties of the tissues are how it modified the vibrations of the entire system to create the variation between different samples. The following steps seek to discover more information about the vibration of Apligraf.

4.1.3.2. Apligraf on air

To simplify the influencing structure, Apligraf was measured on open air. Instead of the transwell disc resting on a bed of agar, the disc was suspended in midair. First a special clamping method was created to just hold the disc, Fig. 49, then fringe and vibration quality was compared

to when the transwell disc was left inside of the original packaging but with the Apligraf removed from underneath it.

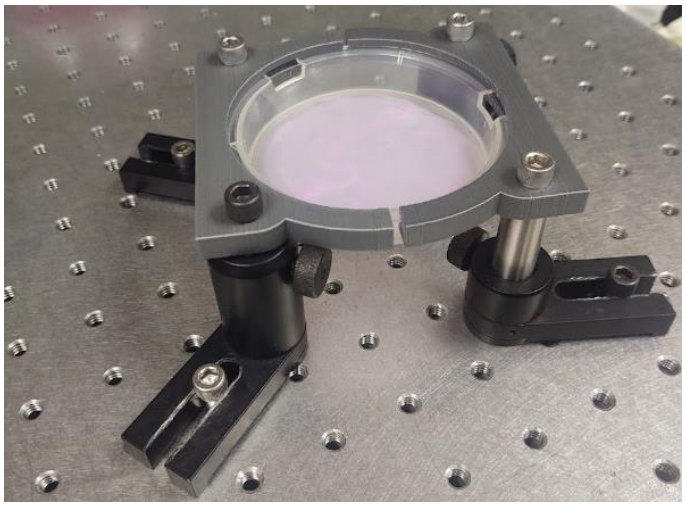

Fig. 49 Holding method for the transwell disc in open air. For measurements taken with this method, there is no influence of agar underneath the sample.

The vibration of the Apligraf, plastic layered structure was difficult to measure in open air. The fringes were not steady, moved a lot, and contained a significant amount of noise such that it was difficult to visually locate vibration modes. The two best modes located were the first mode of the 0^{th} and 1^{st} order, shown left and right in Fig. 50. It is possible that a more powerful laser could make up for the low signal-to-noise ratio by increasing the amount of light scattering back into the camera, but it was not possible to obtain a fringe quality that could be unwrapped into a displacement profile when the transwell disc was in open air. The most significant reason is that the disc's vibration is susceptible to environmental disturbance and a simple finger snap from across the room can be detected as a slight disturbance. This, combined with the constant noise output of the building's temperature control fans makes it impossible for the disc to remain still. Meanwhile, the same transwell disc when placed into the packaging and thus isolated from the

general environment showed a significant improvement to fringe quality, Fig. 50. There was a slight change to the frequencies measured, but it is unknown if this is due to the tissue drying as it was sitting out in the open air. Moreover, the transwell disc while sitting in air inside the package is stable enough such that a full cycle of data can be taken without significant noise or destabilization of the reference.

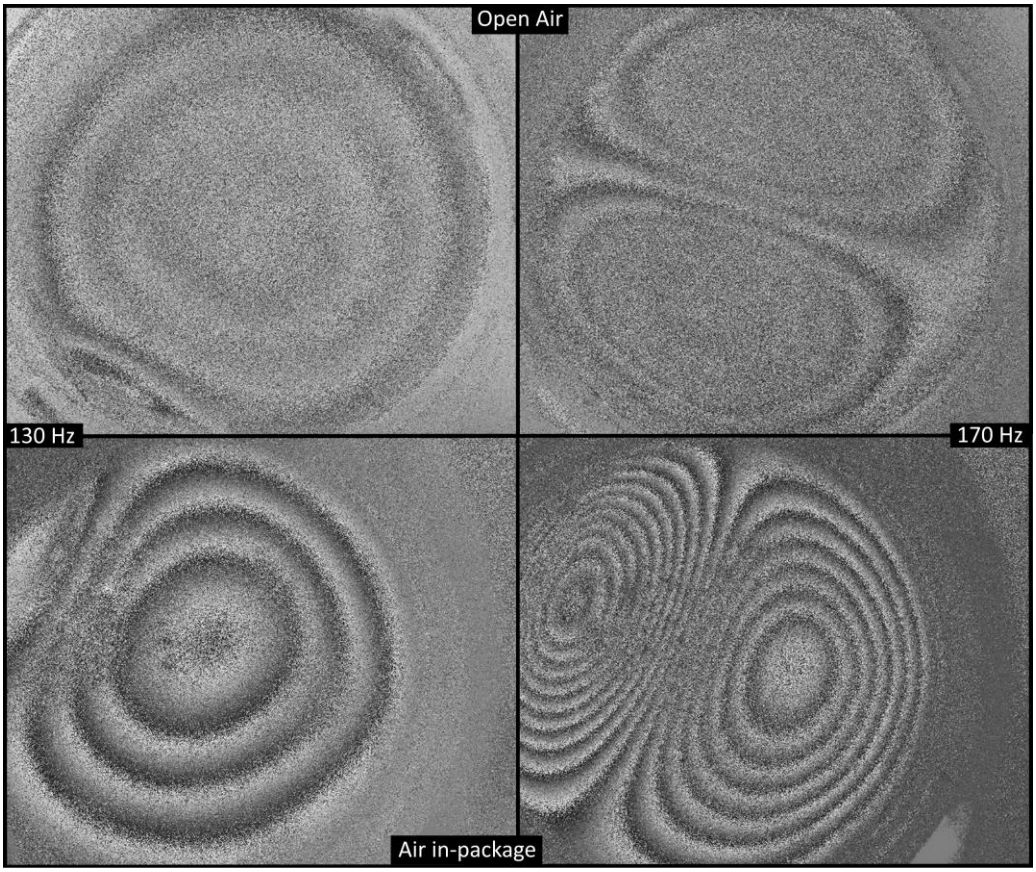

Fig. 50 Fringe quality for two modes within open air (top) and in air inside the package (bottom). Fringes are more distinct within the package for both pictured modes.

It is difficult to measure Apligraf in air exposed to the environment but feasible when in air that is protected from the environment such as in the packaging. However, simply adding the packaging into the equation without the full contact of the agar is able to add enough pre-tensions

to the plastic membrane and tissue that there is a visible non-continuity between the associated images in Fig. 50. The circularity of the top of Fig. 50 contrasting to the slight deformations to the circle in the bottom images indicates the bottom image has slightly different boundary conditions. This is attributed to increased force from the top of the package in one section limiting free movement of the transwell disc and creating a small section of a fixed boundary condition. It is important to note, however, that the fringe patterns do indicate displacements in-line with standard circular vibrations.

4.1.3.3. Apligraf with fluid boundaries

It is ideal to use DHV to measure a tissue such as Apligraf as it is still growing. As tissues are often grown in liquid growth media, it is thus important to see if DHV can measure vibrations of Apligraf in a liquid. An experiment was performed with a goal to identify vibrational modes as the tissue laid fist on water, then submerged within water. First the agar underneath the sample was removed and replaced with dpbs, a saline solution often used in cell culturing [73]. The sample was then placed under a speaker and calibrated to optimize fringe visibility. The normal frequency sweep was performed, but a shape indicating the fundamental mode was not observed. The frequency sweep was then lowered as low as the speaker could go, and a shape similar to the fundamental mode was seen around 43 Hz. Figure 51a shows a typical fringe quality on water. Figure 51b shows an example of the highest found fringe quality found for Apligraf on water, though it is clearly not the fundamental mode. It was observed that there was no stability and an image clear enough to be accurately processed by the unwrapping algorithms cannot be obtained

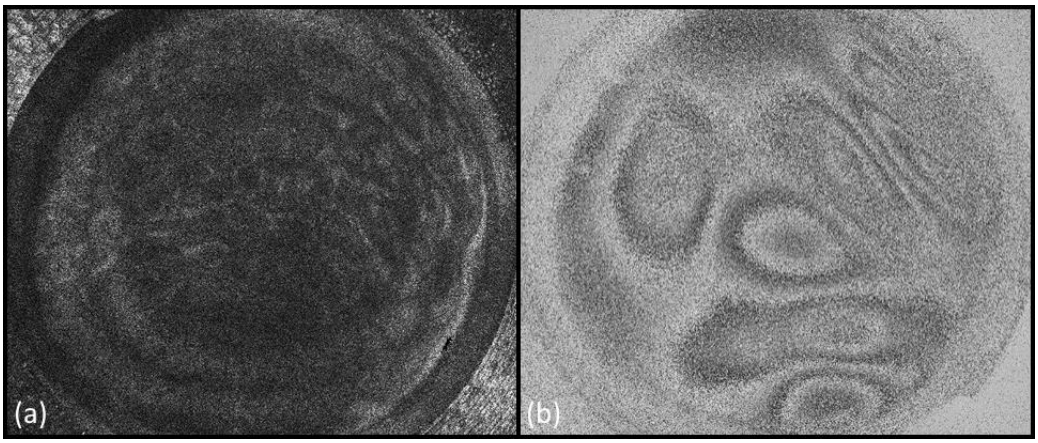

Fig. 51 Images of vibration of Apligraf tissue on water: (a) time average image at a frequency of 88 Hz; (b) optical phase image of vibration at a frequency of 69 Hz.

The frequency sweep was then performed again with a slight alteration where more dpbs was added such that the tissue was completely submerged in liquid. The same instability was seen. It is theorized that the water is susceptible to vibration by the sound waves and that these waves reverberate around the package. As the water has enough inertia to move the tissue and plastic membrane, the instability from the water is greater than the instability caused by the bed of air. This was visually supported when the Apligraf tissue embedded on water was imaged by the OCT as the lines marking the bottom and top of the Apligraf layers were significantly blurred and precise location of boundaries was more difficult to determine, indicating a higher level of passive vibration.

It is also possible that there are potentially multiple modes of vibrations superimposed upon each other. Figure 52 shows markings where there appears to be multiple separate fringe patterns. One follows an expected fundamental mode shape, and the other shows highly chaotic fringes with no discernible meaning. Though this image was taken to maximize the clarity of the orange-marked fringes, the green-marked fringes were more prominent and visible most of the time. If this is true that there are multiple vibration patterns overlaid on each other, it makes extraction of

vibration modes particularly difficult as it is impossible to identify which vibrations occur from the water and which vibrations naturally occur in the tissue. Thus, the conclusion is that vibrational mode data is not obtainable when the Apligraf tissue is in a liquid system.

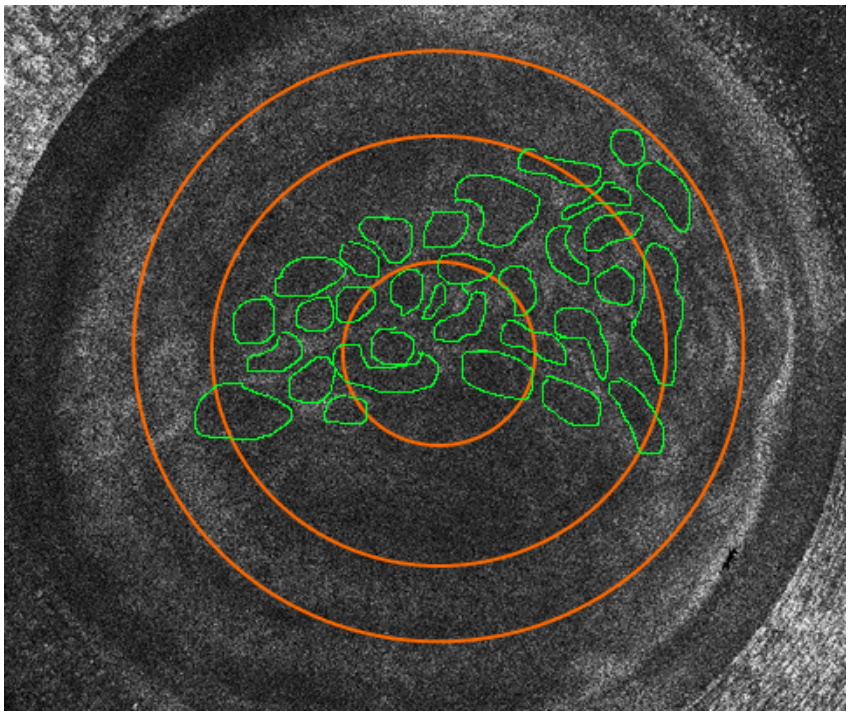

Fig. 52 Time average image of vibrations for tissue on water with two apparent fringe patterns marked with overlaid lines. Orange lines are caused by the water movement while green lines are present in the tissue itself.

4.1.3.4. Drying experiment

Considering the complexity of the entire Apligraf system, it is necessary to establish that the observed measurements are affected by the Apligraf tissue itself. Initial observations showed that the agar and plastic have a significant effect on the vibration of the tissue, so it is most reasonable to model the vibration of the system as a vibrating plastic layer dampened by the more viscoelastic tissue above it. To establish this, an experiment was devised to modify the vibrational frequency by changing only the properties of the tissue. The tissue sample was subjected to

controlled drying to change the thickness and/or stiffness of the sample without modifying the properties of the plastic membrane or the agar.

Due to the destructive nature of the drying, two different samples from the same production batch were used for nanoindentation and DHV. Each sample was dried for 90 minutes in a 23 °C oven, Fisher Scientific, Isotemp [74] for controlled humidity and temperature, and measured at several time points: 0, 3, 6, 10, 15, 30, 60 and 90 minutes. Each sample was put back into the oven with an open lid after measurement until the next time interval was reached. The DHV measured sample was also measured by an OCT at each time interval to determine the thickness of each layer.

OCT measurements of thickness for both epidermal and dermal layers of the Apligraf tissue decreased with drying time, Fig. 53, establishing a change to the tissue and physical properties for the DHV sensor to measure. Stiffness measurements on a similar sample dried under identical conditions showed a steady increase in the stiffness of the epidermal layer up to 35 minutes, a slight drop until 75 minutes, then a sharp increase to the stiffness, Fig. 54.

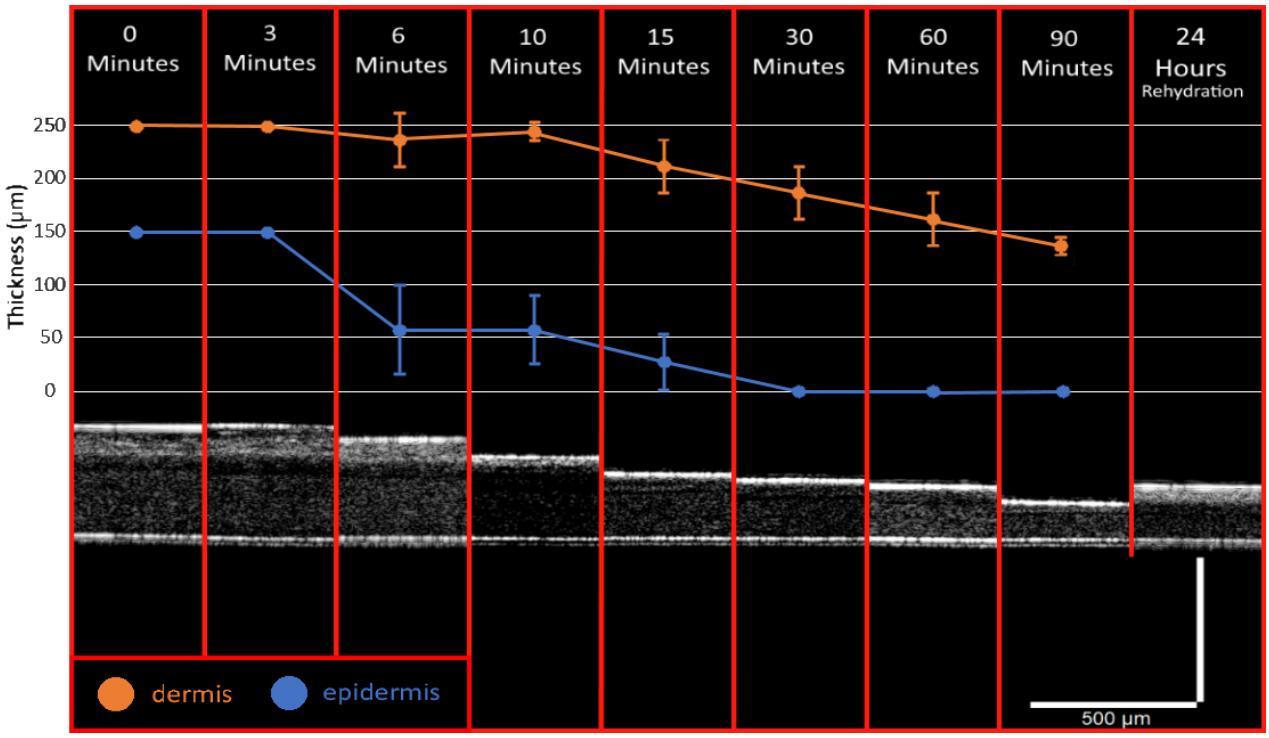

Fig. 53 OCT image of tissue thickness during drying with a numerical representation of thickness measurements for the epidermal and dermal layers. Each dot indicates the numerical value of the thickness of each layer at that given time point.

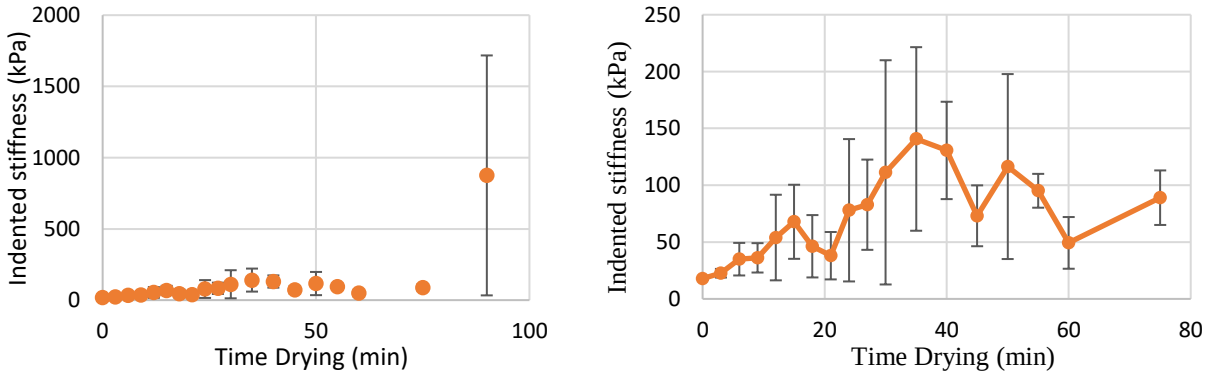

Fig. 54 Epidermis stiffness measured by a nanoindenter while drying [Billiar's group]. Full data set over 90-minute drying period (left) and zoomed in data set (right) with 90-minute data point removed

The frequencies at which each of the 1st four modes of vibration occur decrease monotonically with drying, Fig. 55. The modal FEA in which the layer thickness was decreased to match the measured data shows the opposite trend in frequency of the fundamental mode, Fig.

55. This result indicates that it is more likely that the increase on modulus with drying dominates the vibratory behavior. Figure 55 supports this hypothesis as there is a relatively steady increase to the stiffness of the epidermal layer during drying. Though the standard deviation is high, this result is consistent with previous observations and the largest contributor to the high deviation is spots of water that inhibit accurate indentation measurement but also decrease the effect of the drying in that spot. As such, the average indentation value is expected to be slightly higher within the standard deviation if accounting for such droplets.

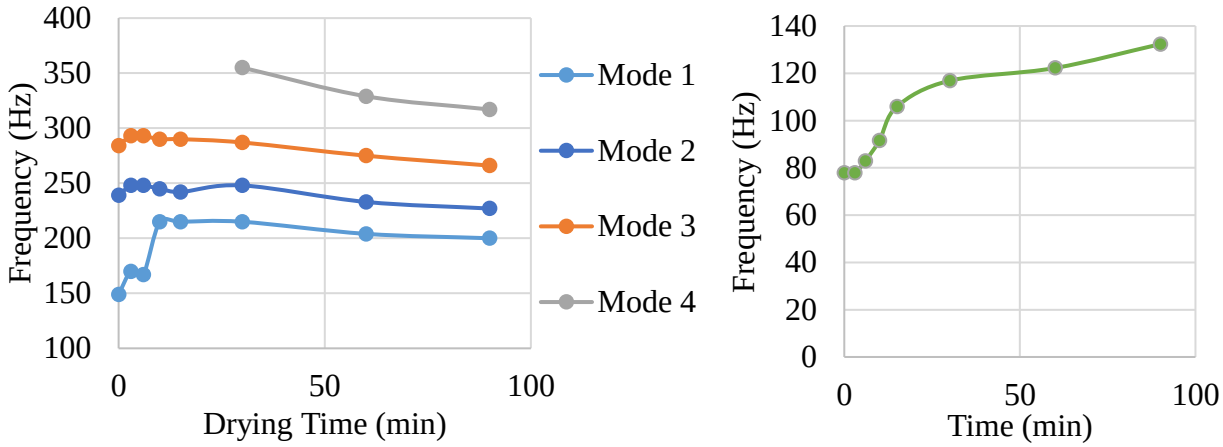

Fig. 55 Frequency of vibration for Apligraf during drying. Experimental data measured with DHV (left) versus simulated data with FE model using thicknesses experimentall determined by OCT during drying (right)

A further analysis was performed, however, in which only the thickness of one layer was modified while the stiffness was held constant, and the other thickness was held constant. The change to frequency as the thickness of each layer decreased was marked down and a line of best fit was calculated, Fig. 56. Both lines had identical slopes, indicating that according to the FE models, a decrease in thickness to both layers should have an equal effect on the frequency.

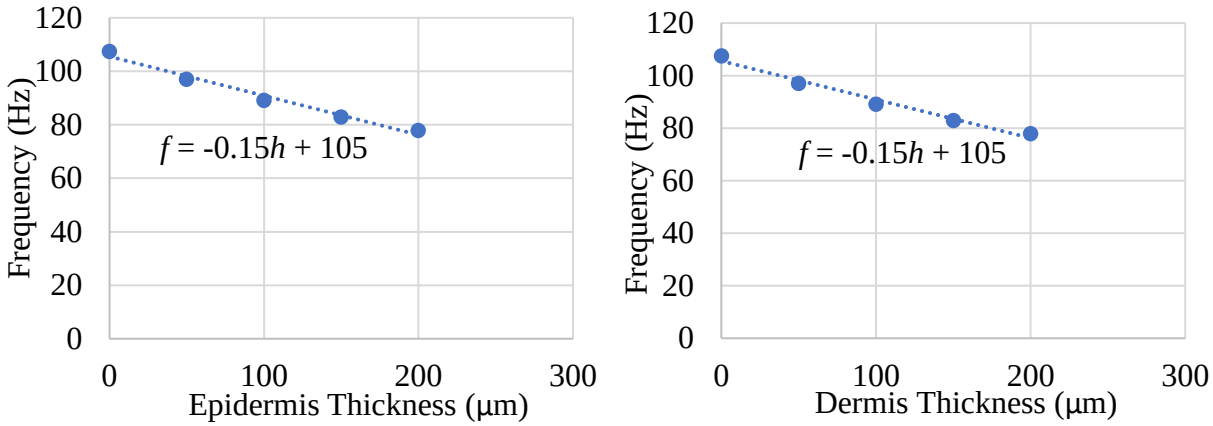

Fig. 56 FEA prediction of fundamental frequency, *f*, response to a change in Thickness, *h*, in the epidermal (left) and dermal (right) layers.

This experiment was repeated with slight modifications with the tissue and plastic membrane sitting on air with no agar underneath. As this was done much later, the oven used to dry the samples was no longer available so drying was done by exposing the tissue, uncovered, to room temperature and humidity. Additionally, measurements were only made at 0, 20, 40, 60, and 90 minutes.

As in the original drying experiment, a consistent decrease was measured in the thickness of both the dermis and epidermis, Fig. 57. The drying was a bit slower and there was a more equal decline in the thickness of both layers at the same time but at 0 minutes the epidermis had once again reached near-zero thickness. In contrast to the original experiment, a relatively consistent increase to frequency of vibration was found as the tissue thinned, Fig. 58. This was also noticeably greater than the original drying experiment, Fig. 59. This is consistent with the simulated results. The disparity between the frequencies of tissue and plastic increasing versus the frequencies of tissue with plastic and agar decreasing is due to the presence of the agar. The change in the system when the agar is introduced likely changes the driving factor of the vibration. When no agar is present the system likely acts as a vibrating plastic membrane dampened by the tissue so when the

tissue thins it dampens the vibrations less. When the agar is present, however, the driving factor of the vibration is a mixture of the agar and plastic system such that the tissue increases the natural frequency from the agar-plastic system's natural frequency. Thus, as the tissue thins, the frequency decreases towards the natural frequency of the agar-plastic system.

It is also worth noting that two separate displacement patterns consistent with the fundamental mode of vibration were found. The lower one pulsed over time and it is likely this is vibration consistent with reverberations of air within the container as they were similar to the reverberations of water. The higher frequency fundamental mode, however, was consistent with fundamental modes observed in other tissues while placed on agar.

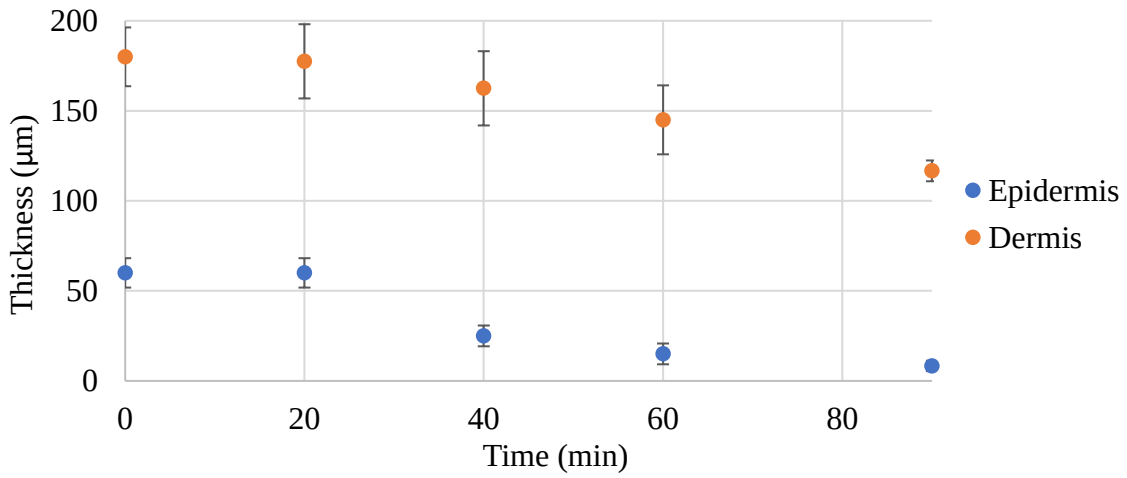

Fig. 57 Tissue thickness measured by OCT during drying via open air.

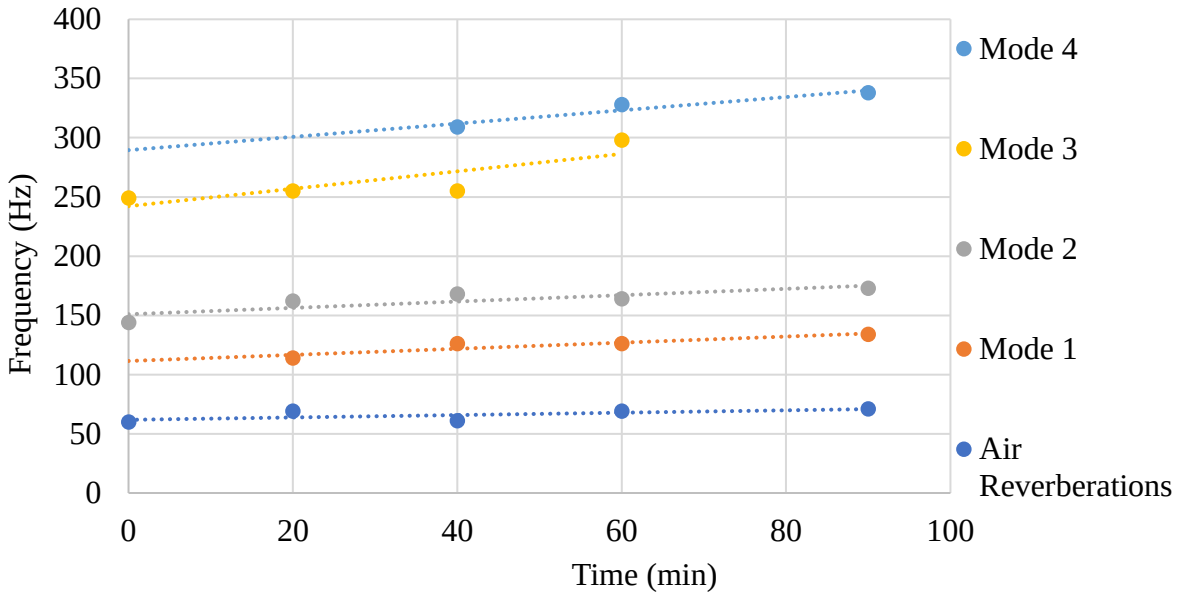

Fig. 58 Measured frequencies of modes of vibration for the tissue on open air.

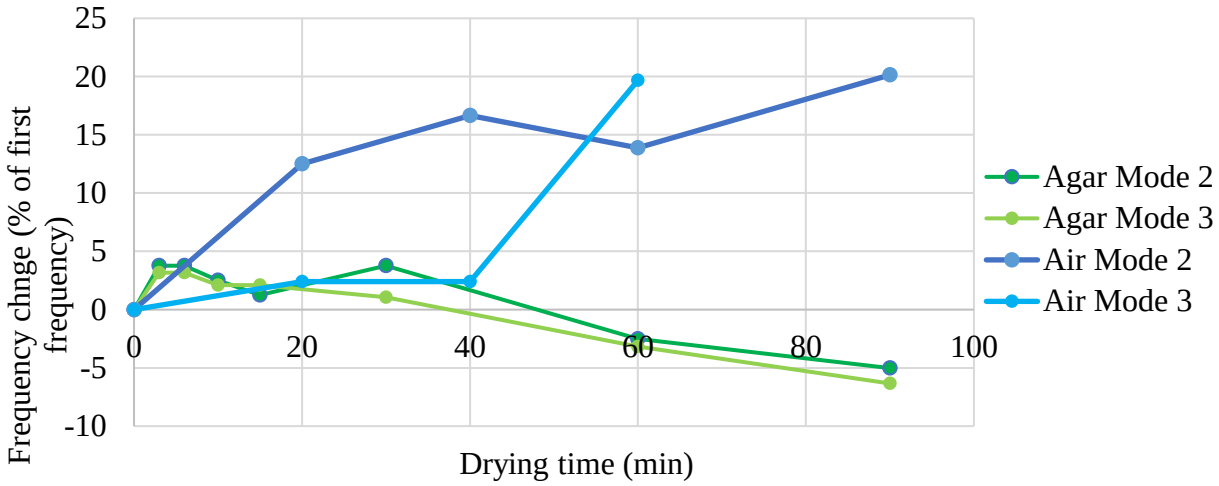

Fig. 59 Percent change to frequency for Apligraf during drying. The 2nd and 3rd mode frequencies are shown for Apligraf that is resting on a bed of agar and Apligraf that is surrounded by air with no agar.

The vibration measured by DHV is clearly dependent on the properties of the tissue. The sensitivity, however, is much lower than desired. The changes observed in the vibrational frequencies are too dependent on the properties of the plastic membrane or agar and a relatively significant change to the tissue is necessary to produce a small difference in the frequency of

vibration. For such a complex system as Apligraf, the DHV method thus appears non-ideal compared to methods that can measure the surface and guarantee that it is the tissue that is being measured. With machine learning, however, it is still possible that observed changes are significant enough. Future work will thus determine whether DHV is viable for such a complex system.

4.1.3.5. Pressure variation

Under the theory that DHV alone can be used to find the mechanical properties of bioengineered tissues, modification of the amplitude of the acoustic pressure applied by the speaker should directly relate to the properties of the tissue. As with a tensile test, increasing the force applied should result in a different displacement of the sample. This could then be related to a stress-strain relationship that should have a direct relation to the stiffness of the tissue.

An experiment was performed in which a tissue sample was measured at the first 4 modes of vibration. Measurements were taken at 4 different pressure amplitudes for each mode. As all selected modes were of the 0^{th} order where the primary displacement is in the center of the sample, the displacement of the sample was interpreted as the maximum *z*-displacement reached by the center point of the tissue during its vibration cycle, Fig. 60.

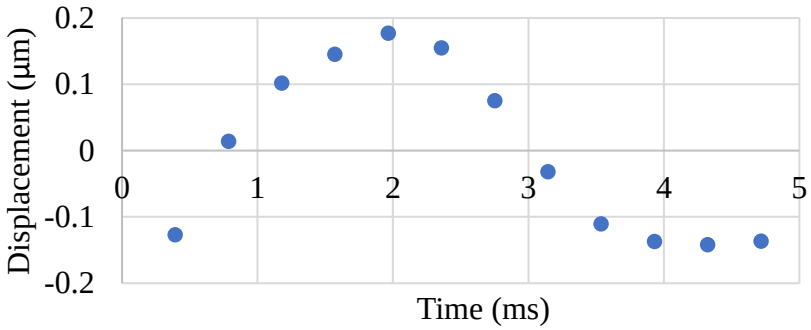

Fig. 60 Displacement of a single point plotted over each of the images taken in one data set.

Plotting the data in reverse of the normal independent-dependent variable axis order results in a graph that imitates a stress-strain graph, Fig. 61, and for calculations, a simple conversion strain can be performed by dividing the displacement by the thickness of 400µm.

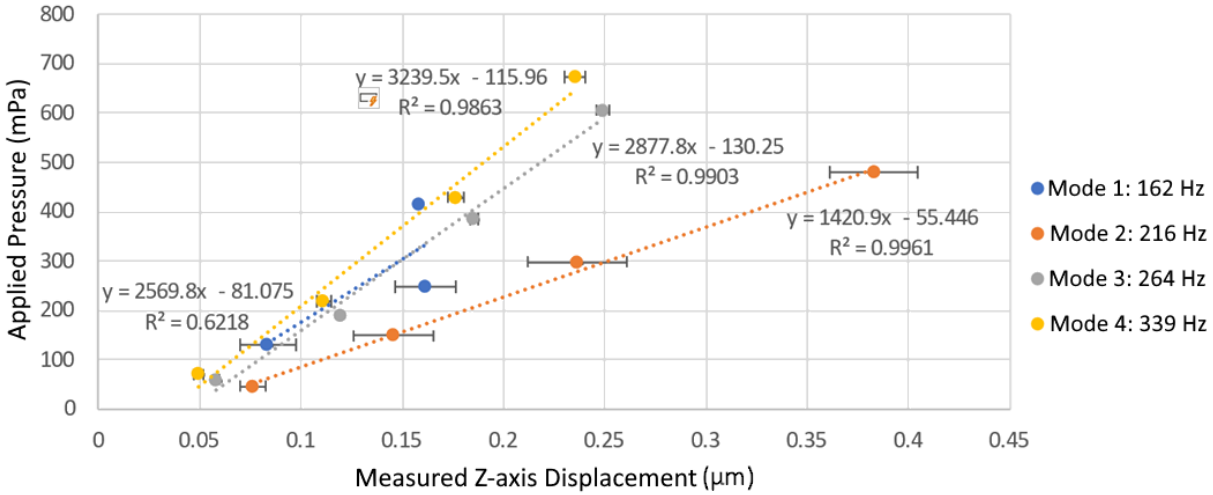

Fig. 61 Amplitude of tissue displacement for 4 modes of one tissue with multiple applied pressures for each mode.

Figure 61 shows a linear best fit model for each mode. In a typical stress-strain graph the slope of this model is the stiffness of the material, so multiplying the displacement by 400µm achieves the stiffness. The equations for the linear regressions of each mode are shown. Assuming a relation of $E = \frac{\sigma}{\varepsilon} = \frac{P}{d}h$ treats the applied pressure as the stress and the displacement divided by the thickness, *h*, as the strain. This relates to a modulus of 1.3 kPa and 0.57 kPa for the maximum and minimum slopes presented in Fig. 62. Meanwhile the typical stiffness of Apligraf tissue is around 20-30 kPa depending on how dry the sample is. These numbers are much closer than the previous CPT calculation, but still a full order of magnitude off of expected values.

This method has several problems, such as the fact that it ignores the multilayered structure that is vibrating and generates only one value and does not account for the difference between

linear movement and the 3D motion of the circular plate. The one benefit of this experiment, however, is that it does show a clear linear relationship between the applied pressure and the displacement at such low pressures, validating the simulation's linear-elastic model. It is possible that this pressure-variation method may prove more fruitful if developed in the future, but a method would first need to be found to separate the non-tissue displacement from the tissue displacement.

4.1.3.6. Surface alterations

The objective of using DH as a full field of view measurement is to measure the full sample at once to extract properties at various properties within the tissue in one measurement as though measuring multiple points at once. Thus, an experiment was created to alter the surface of the sample to observe mode disruptions at a certain point. Measurements were taken as in standard methodology, but a small mark was made on the sample. The tissue was observed and imaged freshly out of the package and modes were located, then a Section of the Apligraf's epidermal layer was peeled off using the edge of a blade. The tissue was imaged again at the same frequencies, the scar was doubled in size, then the tissue was imaged a final time. One sample yielded some visible differences to the fringe at the area of scarring.

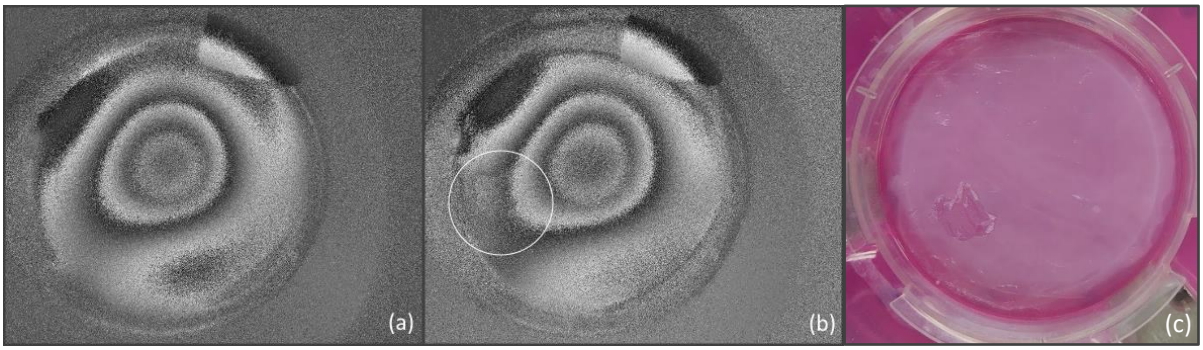

Fig. 62 Images for removal of tissue's epidermal layer: (a) optical phase image of fundamental mode of a normal surface with no damage; (b) optical phase image of fundamental mode of damaged surface with a 1 × 1 cm section of epidermal layer removed; (c) camera image of 1 × 1 cm section of epidermal layer removed.

The second sample on which this experiment was performed, however, did not yield visible results. It is difficult to tell whether the observed result in Fig. 62 was due to a mode disruption by the scarring or whether the scarring modified the amount of light reflected into the camera and thus appeared different due to optical differences and not mechanical differences. The final scar, however, was 1.5 cm^2, at which point the difference was easily observable to the naked eye and a complex system to image a slight difference was redundant. As the objective was to identify singular points of defect by imaging the entire system, any defect significant enough to be able to be measured by a technician or even a color camera was too great for this system to be useful.

An additional experiment was performed in which displacement of Apligraf was measured on air in the packaging, scarred a first time in a 1 × 2 cm section and measured, then scarred a second time to make a 2 × 3 cm scar. The resulting displacement is plotted for two modes in Fig. 63. Here the difficulty of identifying modes of vibration for the transwell disc exposed to air was particularly noticeable. The first mode shows solid results with a steady decrease in the displacement resulting from the scarring, while the second mode seems more erratic. Here it is difficult to be sure the second image was measured correctly. There was an attempt to measure a

third mode, but it could not be properly identified at all. This experiment suggests that the amount of scarring does noticeably affect the displacement amplitude, but it is difficult to know whether this is the result of the actual scarring or the result of the tissue drying while being scarred.

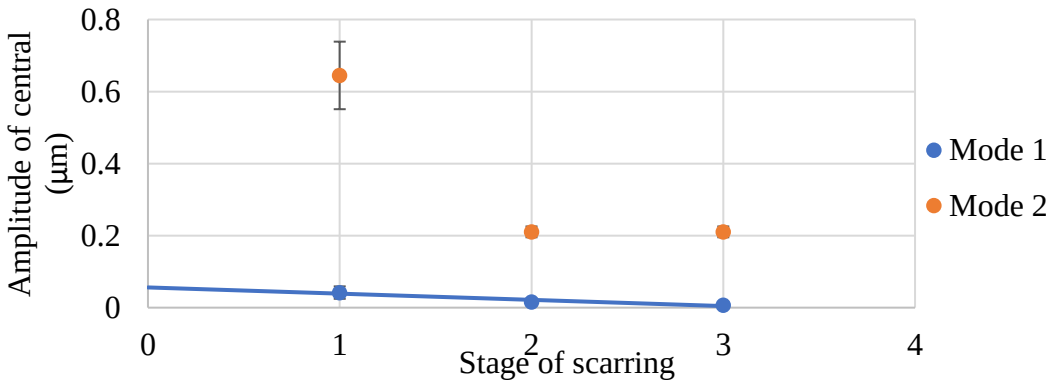

Fig. 63 Max displacement of transwell disc on air: (1) no damage to tissue; (2) 1 × 2 cm section of epidermis removed; (3) 2 × 3 cm section of epidermis removed.

From this experiment, it is concluded that while DHV can measure the full field-of-view of Apligraf, the complexity of the structure and the larger depth that controls vibration maintain a homogeneous vibration characteristic. The sample's vibrations might modify slightly with surface modification, but DHV measures the sample as whole and whatever conclusions the machine learning algorithm is able to draw will be bulk properties. The use of vibration at such lower frequencies does not produce an image full of individual measurements but instead one single measurement. Expansion of this method to higher frequencies may yield different results.

4.1.4. Machine Learning

The machine learning component of this research is still in progress. It is performed by a data science and computer engineering lab by Ziyang Gao (PhD candidate, cs) and Professor Dmitry Korkin. These individuals built a 3D shape classification model based on Pointnet [75].

They trained it using pointcloud files from the FE simulation to classify stiffness and thickness of the epidermal and dermal layers. They analyzed three equidistant radial lines on the circle, Fig. 64, and selected all datasets where these lines were symmetric, indicating 0^{th} order vibration modes. This resulted in 1440 simulated files, which were randomly split by a 0.33 ratio for training and testing. Each pointcloud contained 1763 nodes with *x*, *y*, and *z* coordinate values representing each point of the tissue. Then the FE simulation results were extracted for corresponding 0^{th} order modes. The labels of the sample were encoded according to the mean value of that property, where a 1 was encoded for values greater than the mean and a 0 was encoded for values less than the mean.

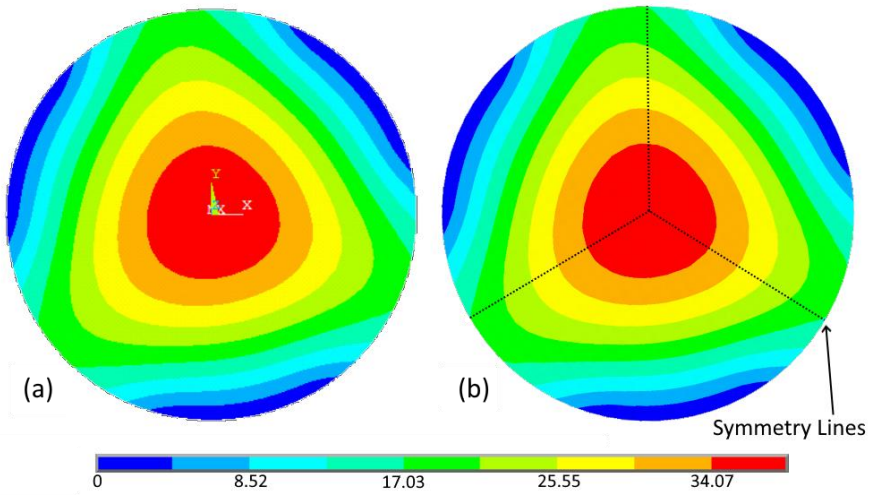

Fig. 64 FE modal analysis results for the Apligraf model: (a) Fundamental mode shapes calculated by the FE simulation; (b) overlaid symmetry lines used for identification of 0^{th} order modes.

The architecture of Pointnet was applied and the hidden layer nodes were modified to fit the FE simulation data better, Fig. 65. The input transformer network (T-net) links the input layer with the first primary MLP, and the feature transformer network links two primary MLPs together. The global feature was generated by maxpooling the second MLP output, and later the input

frequencies were concatenated as an additional feature. The overall features were processed by the final MLP to generate the output class.

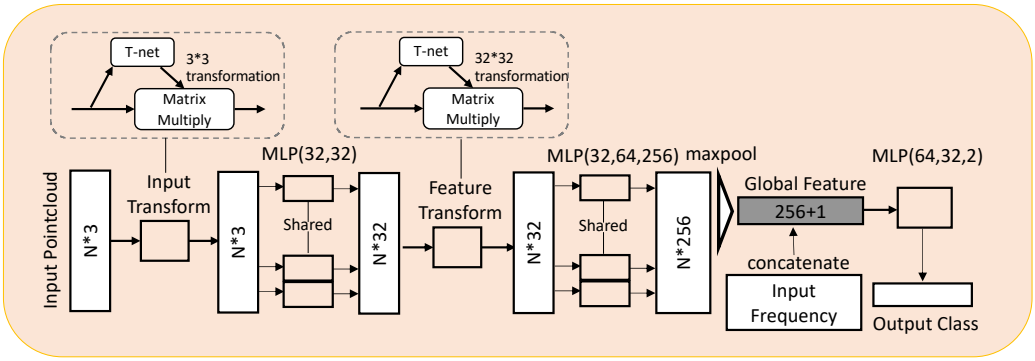

Fig. 65 Architecture of the Pointnet based 3D classification model with frequency input [Korkin's group].

The resulting algorithm was trained to classify the stiffness and thickness of the epidermal and dermal layers based off of the mode shapes (table 5). It showed a decent accuracy in three of the categories but a lower ability to classify the stiffness of the dermal layer. Subsequent testing uses the added input of the frequency values.

Table 6 Accuracy of Pointnet 3D classification model for the stiffness and thickness of the epidermal and dermal layer based off of FE generated mode shapes.

-	Modulus	Thickness
Epidermis	0.767	0.710
Dermis	0.494	0.773

This forms the training step of the machine learning process. Next, the point clouds from real data sets will be integrated with the supervised learning algorithm. Several different samples have been measured with real displacement patterns and real stiffness measurements. This will

allow for a semi-training classification step where the algorithm will learn to associate the measurements with simulated models so that it can predict real properties without known values.

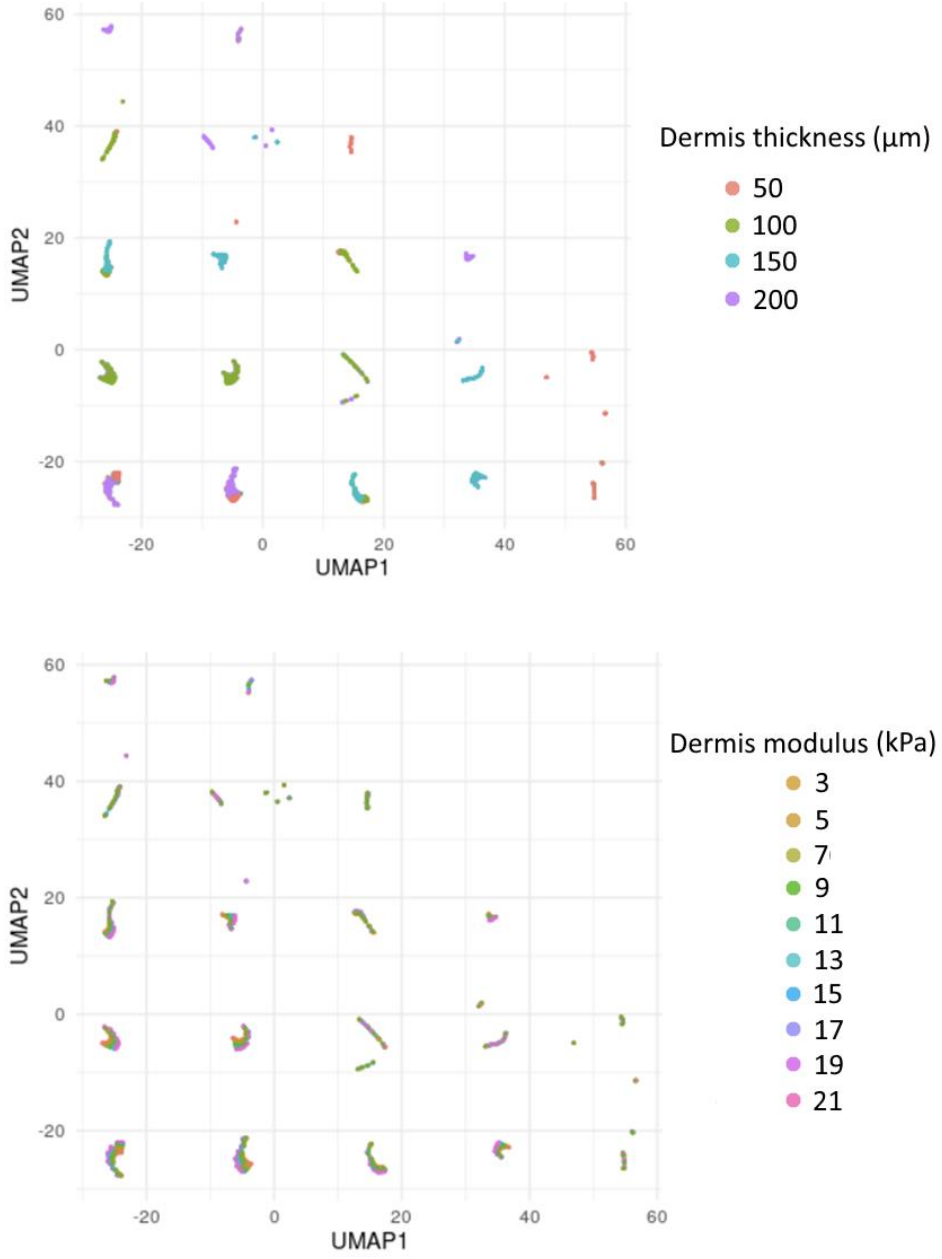

Fig. 66 UMAP dimensional reductions of FE model data. Each point represents one model that is input into the neural network. This shows the clustering of the data according to the shape and frequency data according to the thickness of the dermal layer (top) and the modulus of the dermal layer (bottom) [Korkin's group].

4.1.5. Apligraf conclusions

The system clearly demonstrated a low sensitivity to the vibration of Apligraf specifically. Part of the problem is that the system is very complex and multilayered. Vibration could be seen with the plastic membrane when no tissue was present. It is thus partly the plastic membrane underneath which affects the vibration.

Furthermore, the agar layer underneath the tissue influenced the vibration. The agar itself cannot be imaged as it does not scatter enough light into the camera. When it is covered in a layer of spray paint, however, its fundamental mode appears to have a vibrational pattern identical to what is seen with the tissue, Fig. 66. At the same time, the second vibrational mode of the agar, Fig. 67b, exhibits a similar but different vibration as is seen with the tissue, Fig. 67a.

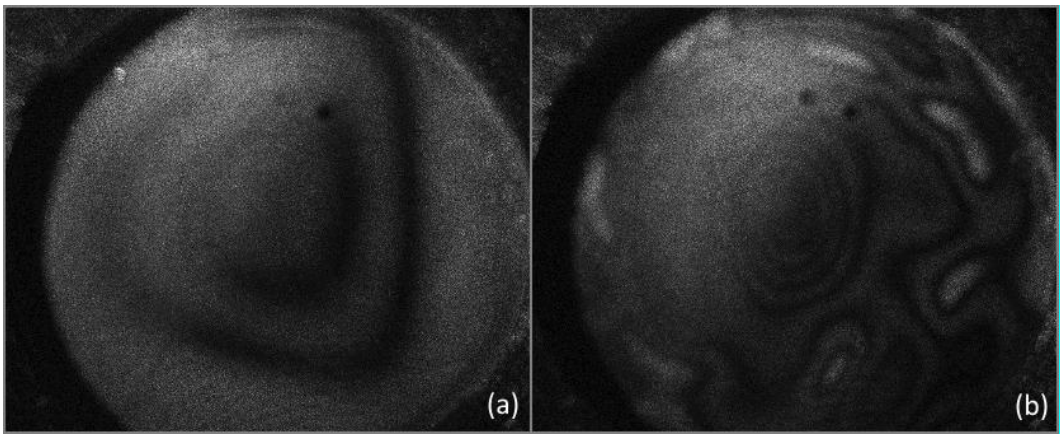

Fig. 67 Time average fringes for only agar layer covered with spray paint film: (a) the fundamental mode of vibration; (b) the second mode of vibration.

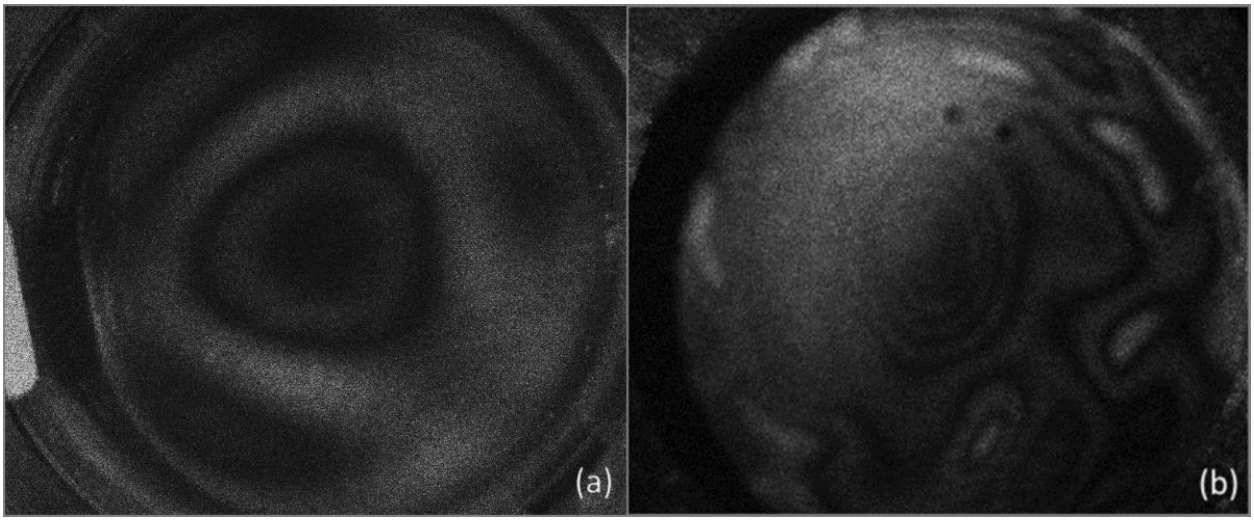

Fig. 68 Second modes of vibration found by DHV: (a) vibration found in tissue resting on top of agar; (b) vibration found in only agar with no tissue.

It is this multilayered structure that made Apligraf very difficult to model mathematically and difficult to image. It is still possible, however, that as the machine learning algorithm progresses with real data, a clearer prediction method will be found.

There are several other issues of note. The system is extremely sensitive to external vibrations. The penetration of light through the tissues rather than pure reflection off the surface lowers the quality and clarity of fringes. These, combined, with non-uniformity in some layers of the system has resulted in difficulty of locating vibration modes. Whether the modes do not always occur, or they just change shape enough to be difficult to identify sometimes, the single greatest reduction to reliability was in misidentification of modes.

It is also inherently difficult to measure Apligraf in a deterministic manner. The tissue's properties change as it dries and as it ages. To control for this, most tissues were purposefully measured as freshly as possible without removing the lid. Obtaining reliable information of the mechanical properties to train the ML algorithm was difficult though as the sample would dry as the indentation measurement took place.

4.1.6. Alternative methods for future exploration

Future work has been discussed that needs to be performed to complete and refine the methods related to DHV. Two alternative methods, air puff fringe projection (APFP) and high-speed holography, are briefly assessed that have the potential to add to DHV measurements or may more accurately determine the mechanical properties of tissues. They are discussed here compared to the complexity of the Apligraf system and packaging that inhibits simple characterization with DHV.

4.1.6.1. Air Puff Fringe Projection

Air puff fringe projection (APFP) was discussed in the background as a precursor to the development of DHV. There are several pieces of information that the APFP method did not account for, so a cursory reproduction of this method has been developed to assess more details and ascertain its viability. The original work on APFP did not account for the complexity of Apligraf's layers. It treated its estimations as if it were a single layer and as such it did not provide any information about the effect of this complexity on the measurement capabilities.

The CHSLT labs at WPI contain a fringe projector created by post-doctoral fellow and used for a variety of applications. It covers a larger area than the fringe projector created for the original APFP method and is not integrated with puff control so the application of force for this air puff was a continuous flow of air activated by a manual valve for the duration of the image. This device also required separate calibration to derive *z*-axis displacements, so the results shown are comparative, though still informative. The sample was held upright, and the lid was removed to allow for air application, Fig. 69.

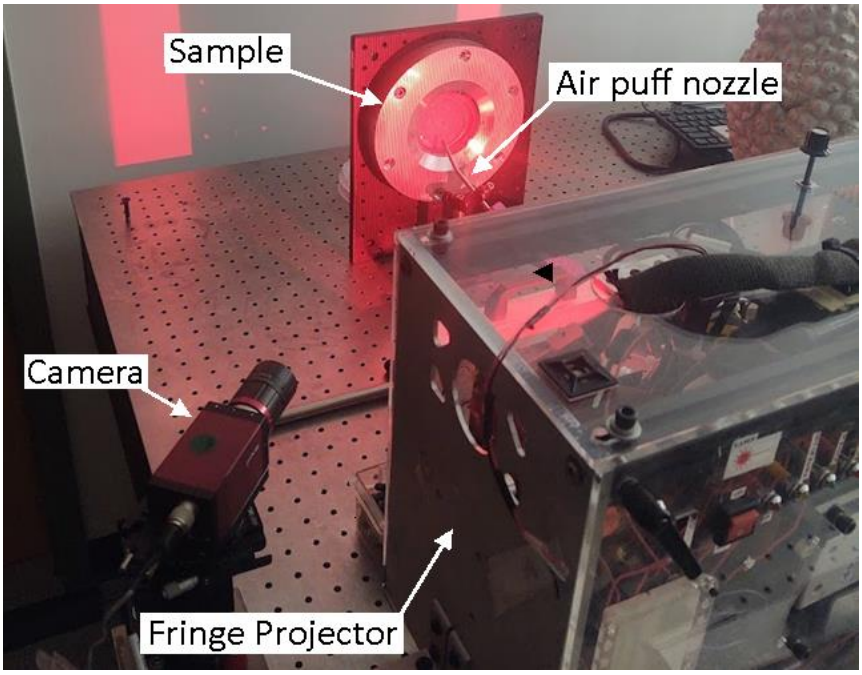

Fig. 69 Image of APFP with Apligraf tissue in imaging area.

An air pressure regulator was used to set the pressure to 60 psi and 100 psi. The air was manually activated via a valve and the Laserview program was used to take a single image of the indented sample. The sample was replaced by a different transwell disc from which the Apligraf tissue had been removed, leaving only the plastic membrane and the agar, and the images were taken again.

As shown in Fig. 70, for both pressures, the indentation level with Apligraf was greater than the level without Apligraf. This definitively demonstrates that a measurable amount of the displacement occurs within the tissue itself. A subtraction of the plastic measurement from the tissue measurement allows for an estimation of the deformation that occurs purely within the tissue, Fig. 71.

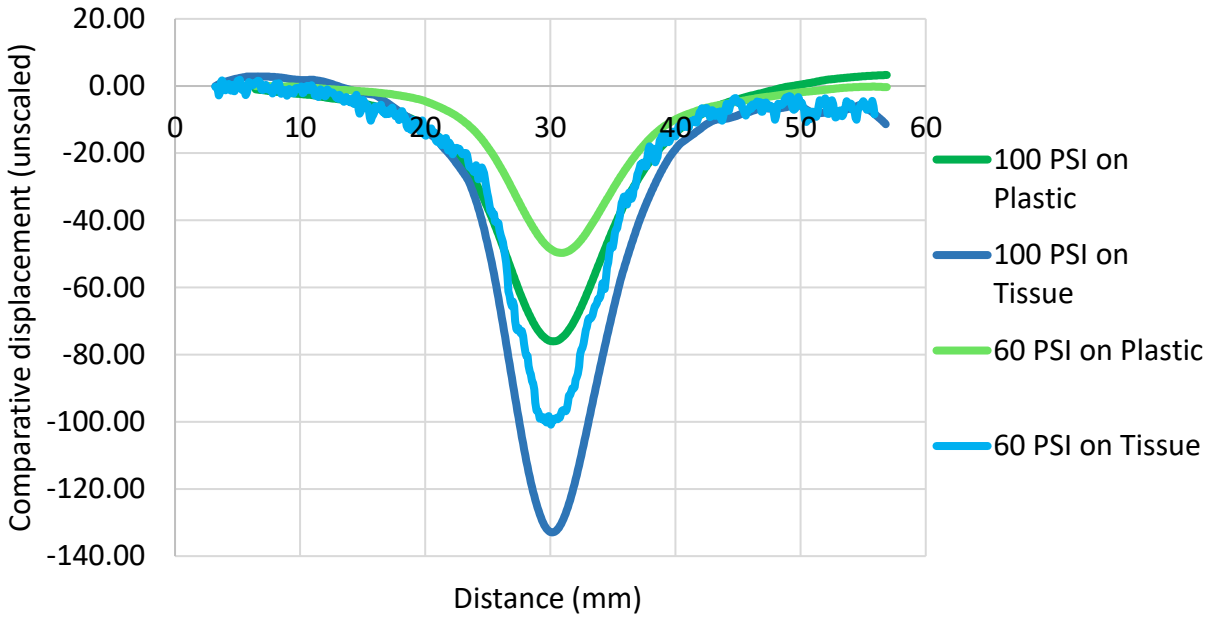

Fig. 70 Cross-sections of measured deformations on Apligraf tissue and plastic membrane during APFP. Deformations are measured by two different pressures, 60 and 100 psi. Pressure and deformation can be used to extract mechanical properties of tissues.

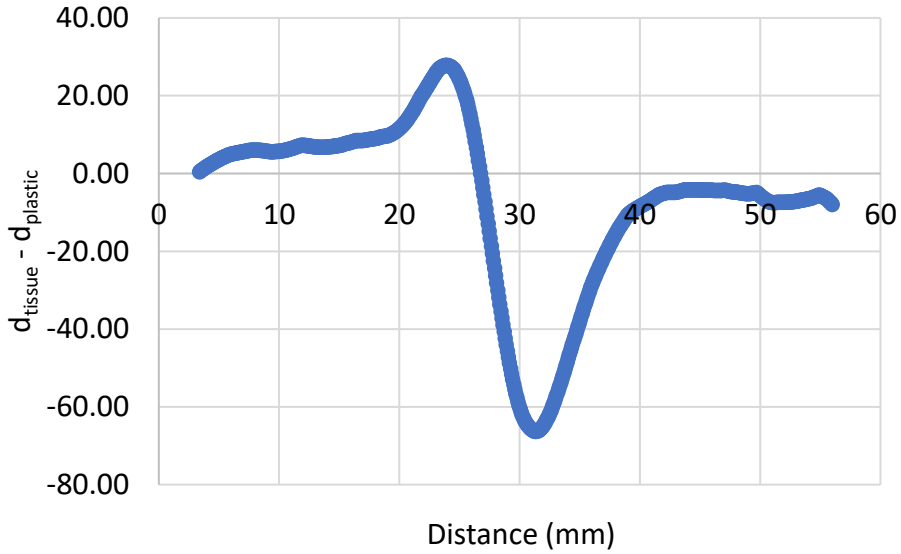

Fig. 71 Difference in deformations between tissue and plastic membrane at 100 psi. This difference can be used to isolate the mechanical behavior of the tissue from the layers beneath it.

The APFP method shows more reasonable estimates of Apligraf properties. Several agar/plastic membrane measurements without tissue would have to be taken to prove the reliability of assuming it's indentation value or else they would have to be imaged every time. The measurement showed a clear difference between tissue layers and plastic layers, though it is uncertain if the positive wave to the left of the indentation shown in Fig. 71 is due to the non-normal force produced by the angle nozzle or from a lack of optimization.

The greatest concern with this method is the application of a large amount of air. This method uses a large quantity of pressurized air, which holds the potential to dry the tissue and change its properties. This is also a large amount of pressure that can harm the tissue itself and can only measure one area at a time. The camera and fringe projector used in this were general purpose and a higher resolution image could easily be produced with a specialized system, which could require a smaller air pressure or smaller area of pressure. This could further connect this method to a nanoindentation method where air pressure could be applied at multiple locations where the effect of the plastic membrane might differ, or the tissue's properties might differ.

The air puffing method is likely to be as effective as nanoindentation but significantly faster if developed further. One notable area of concern and limitation of this technology is the resolution limit. Even a high-resolution camera will reach a limit due to tissue properties. The light from the laser penetrates into the tissue and reflects back, creating significantly fuzzier boundaries of fringes than with more reflective surfaces. This limits the fringe density which can be applied. Furthermore, the fringe projection method has a larger minimum measurable unit than the holographic interferometry presented in this paper, with the latter holding a resolution within tens of nanometers and the particular fringe projector used in this Section within tens of microns of scale. Ultimately, it is advisable to pursue fringe projection for larger and more complex tissue

systems where application of air is not as damaging to the tissue, and application of fringe projection to simpler and more sensitive tissues.

4.1.6.2 High speed imaging of ultrasonic waves\

The CHSLT lab has developed a high-speed holographic method that is capable of measuring vibrations in eardrums of live chinchillas in response to an acoustic chirp [51]. This technology was combined with an ultrasonic piezoelectric shaker to measure the wave speed propagating through the tissues. A sample of Apligraf was selected an the piezo was attached to the plastic membrane on the opposite side of the tissue with Loctite superglue. The sample was placed into the aluminum clamp developed for DHV and placed sideways to be aligned with the camera lens, Fig. 72.

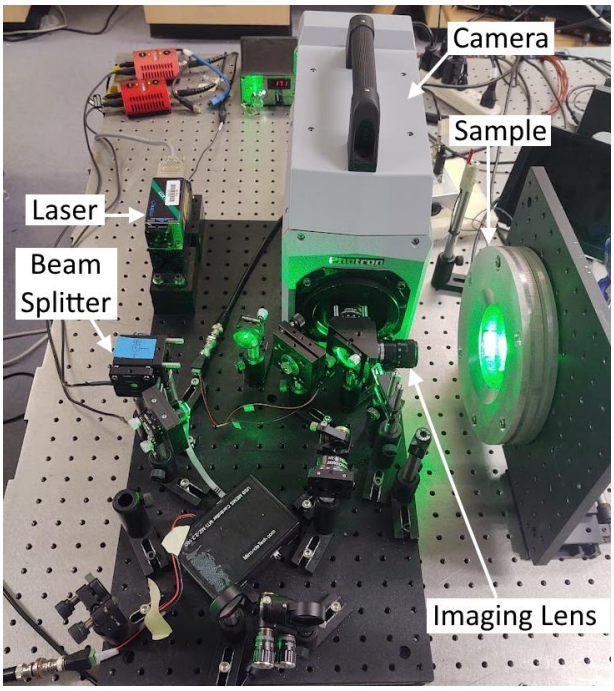

Fig. 72 High-speed holography setup. Labeled are critical components including the laser, beam splitter, imaging lens, sample, and camera.

A 14 kHz signal was sent to the shaker and the shear wave response was measured by the high-speed holographic sensor. The camera acquired images at 67200 fps. And measuring the distance travelled by wave fronts in multiple frames produced a calculated wave velocity of 7.3 ± 1.4 m/s. The high standard deviation recorded is due the high signal to noise ratio blurring the edges of waves and the curvature of wave fronts at some points as can be seen in Fig. 73.

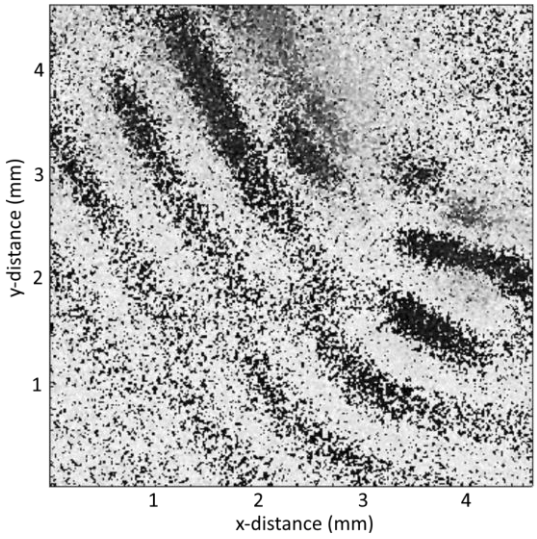

Fig. 73 Optical phase image acquired by the high-speed holography of waves propagating through the tissue, induced by a 14 kHz piezo. The distance between fringes is related to the speed of wave propagation, which relates to mechanical properties of the tissue.

Still, this value is reasonable as literature reports speeds of approximately 3 m/s for shear waves with a frequency of approximately 1kHz with a direct relationship between the wave speed and frequency [76]. The wave speed is directly related to the mechanical properties of the tissue as in Eq. 35 [77], which relates the velocity, v, with the stiffness, E, and the density, ρ. This equation becomes more complex for a viscoelastic tissue, but the observed measurements showed low deformations with a maximum of one fringe (equivalent to 42 nm for 532 nm wavelength light) visible. This suggests that the applied force was low enough to use a simplified

equation such as in Eq. 35 which applied to standard linear-elastic materials. Given a density of 997 kg/m^3, the stiffness is thus 53 -18/+22 kPa.

$$v = \sqrt{\frac{E}{\rho}} \tag{35}$$

The normal stiffness of the Apligraf tissue is expected around 20 kPa. However, the tissue used in this sample was exposed to air during measurement as the wires connecting to the piezo required an open lid during attachment of the piezo and measurement. Thus, it is reasonable that the tissue was dried and thinned and thus exhibited a higher stiffness. As such this calculation of 53 kPa is the most reasonable of the methods presented in this Thesis.

This measurement method has room for future development. The high-speed holographic system used is setup to image tympanic membranes. Reproduction of the system with a direct intent of application to general bioengineered tissues would allow for more optimization. For example, the field-of-view is small and lacks the ability to image larger tissue areas without modifying the lens or camera resolution. However, the frame rate is affected by the camera resolution so for a larger field-of-view either a spatial or temporal resolution may decrease.

The image acquisition presently only captures the optical phase, but time average measurement may provide fringes with a larger signal-to-noise ratio. The measured shear wave, propagation, however, is already connected to mechanical properties through elastography so with further development this method is likely to accurately predict mechanical properties of tissue. If further development is pursued, a more complex analysis will have to be performed to account for the effect of the viscous properties of the tissue.

The high frequency shear wave propagation method is, however, more invasive than both DHV and APFP. The placement of the piezo actuator will require significant refinement for future viability. Initial attempts to place the piezo on the side of the transwell disc did not yield

measurable waves so the location was moved to underneath the plastic membrane. At this location, the ultrasonic waves were mildly destructive to the tissue. The heat from the piezo or possibly damaged or dried some of the closest tissue segments as a ring was observable around the piezo's location where the tissue's appearance was inconsistent with healthy tissue. Additionally, the piezo was attached to the plastic membrane with glue, which clearly alters the integrity of the packaging and invalidates FDA approval. As such, application of this method requires identification of a method in which the shear waves are produced from outside of the packaging or without a physically attached piezo.

4.2. Ligaments

The second type of tissues that this Thesis seeks to test with the DHV sensor is a ligament. A partner of BioFabUSA [78] is currently developing bioengineered bone-on-bone ligaments and BioFabUSA itself is developing a mass-manufacturing method for these ligaments. Though details from this company's ligaments are proprietary, the concept of measuring ligaments to determine their readiness is a logical next step. The function of ligaments is to hold two pieces of bone from pulling apart, and thus the tensile strength and stiffness form crucial components of their functionality. This Section explores the application of the DHV sensor to strings as they are geometrically very similar to ligaments. This stands as a proof of concept that the system can measure vibrational modes within a string. Future work will stand to hone the method to work on ligaments in their actual casing, Fig. 74.

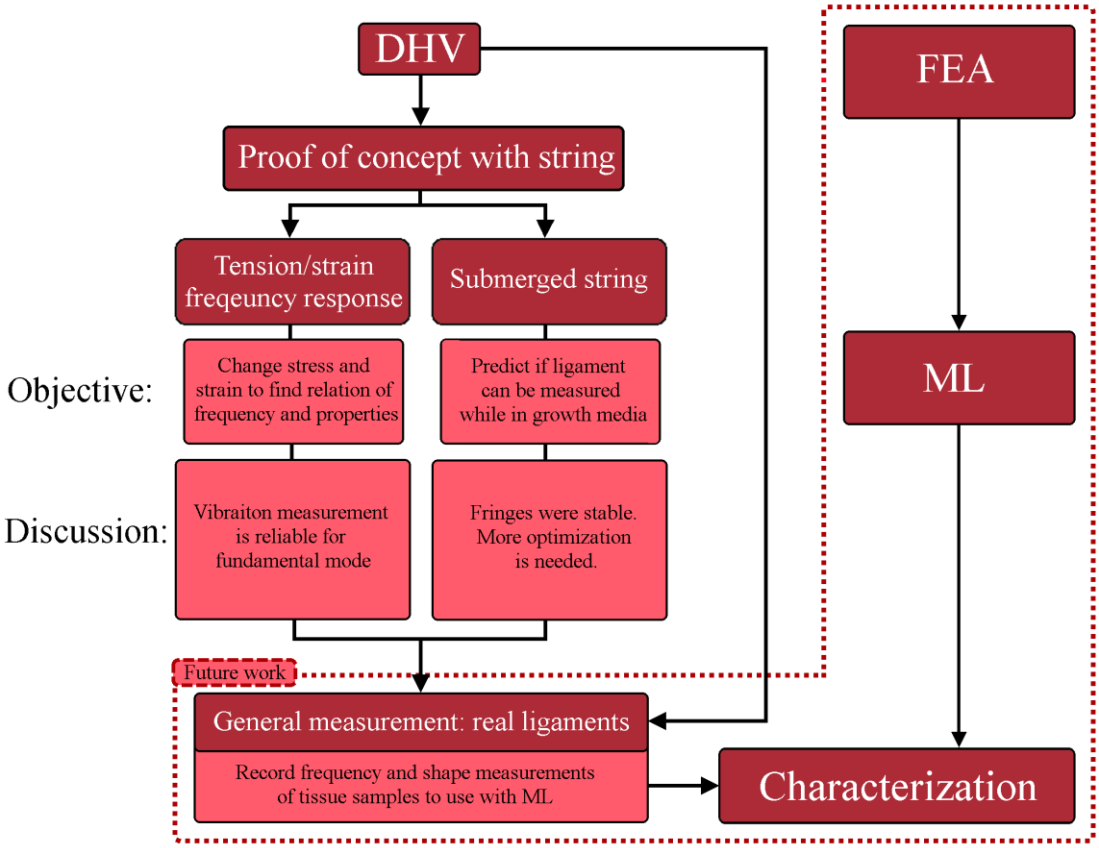

Fig. 74 Flowchart of application of DHV to string proof-of-concept. DHV measurement of real ligaments remains as future work with FE models and ML integration also being future work if deemed necessary

4.2.1. Ligament and string construction

A ligament forms a long thin strand. Like a string, it cannot be compressed without crumpling and instead operates in tension. Ligaments are made mostly of collagen. The growth of the ligament under development by BiofabUSA has two parts, but the basic growth method is that bone tissue is created at two posts, and then a petri dish is seeded with ligament cells. As these cells grow, they form a line between the two bone components. As this develops, the tension and stiffness in this line increases, transforming the dish of cells into a ligament. When the ligament meets necessary geometric properties such as proper thickness, and the stiffness of the ligament is

sufficient, its growth is complete. Thus, measurement of mechanical properties can determine readiness and is of particular importance for ligaments.

4.2.2. Principles of string vibration

As the DHV sensor operates by vibrating a sample, an understanding of the vibration of strings is necessary. String vibration analytical models draw their roots back to the ancient greeks. Vibration of strings is most easily related to musical instruments, where a tensed string vibrates at certain natural frequencies, making noise within the audible realm. Changing the tension on the string changes the natural frequency of vibration. Similarly, changing the length of the string, such as by applying pressure at a guitar fret, changes the frequency of vibration. Mathematically information comes from equations for the velocity *v* of a wave on a string, Eq. 36.

$$v = \sqrt{\frac{T}{\mu}} = f\lambda \tag{36}$$

Here *T* is the tension on the string and μ is the mass per length of string [79]. The wave velocity also relates to the frequency *f* multiplied by the wavelength λ. When the wavelength fits into the length of the string, it achieves a standing wave, Fig. 75. If the string is fixed on both ends, it must fit by a whole number, such that the fundamental frequency occurs at $\lambda = 2L$.

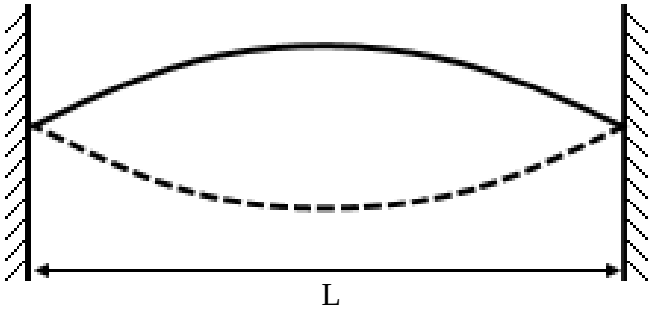

Fig. 75 The fundamental mode of a standing wave in a vibrating string.

To find the modulus instead, the tensile stress can be replaced with the modulus and the strain, Eq. 37. Here the strain has been simplified to the change in length over the length ($\Delta L/L$).

$$f = \frac{\sqrt{\frac{E\Delta L}{m}}}{\lambda} \tag{37}$$

When measuring bioengineered tissues, however, the length or the tension within the tissue is not a controllable factor. The tension thus remains as an unknown. A machine learning approach is suggested similar to that seen for the Apligraf application that can classify the properties based off of the observed vibrations.

4.2.3. String experiments

Several experiments were performed in which the vibration of a string was analyzed. First the string was vibrated and measured to establish that DHV presented measurement capabilities, then the string was submerged into a tub of water and imaged again to establish whether the string needed to be in open air during vibration.

4.2.3.1. String experimental setup

The string was bound at both ends such that it had fixed boundary conditions, Fig. 76. This both emulated normal mathematical estimations and real growth conditions for the ligament. One end of the string was held in place by a screw and the other end was attached to a force sensor Thorlabs, HFV002 [80]. In turn, the force sensor was attached to a movable plate controlled by a motor with nanometer resolution.

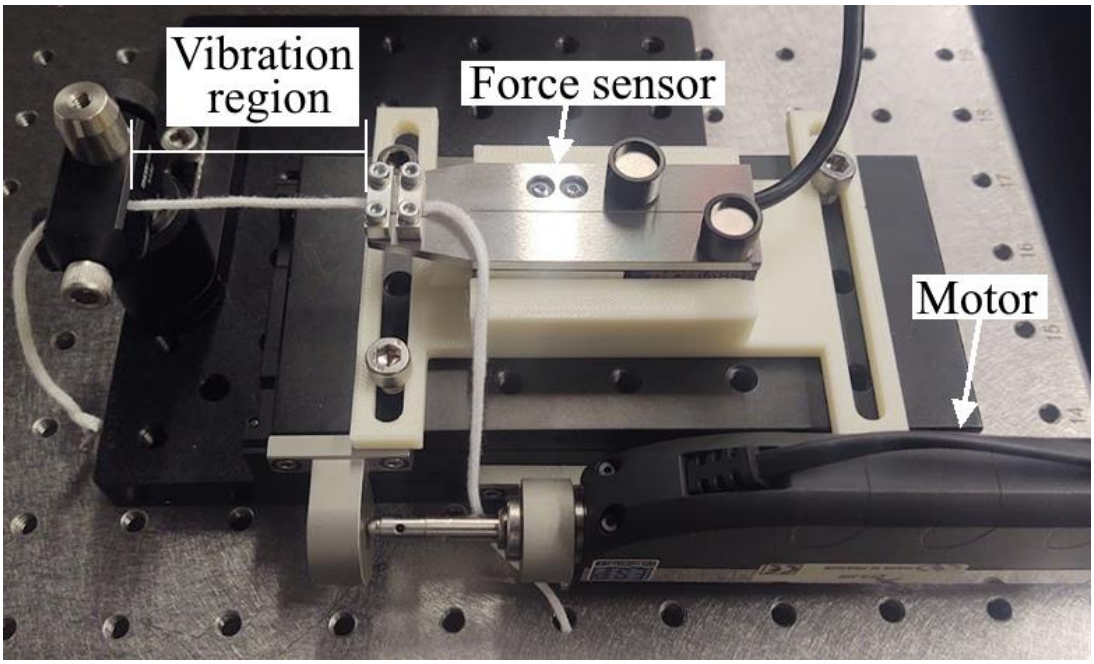

Fig. 76 Mounting system the string used as a proof-of-concept for the ligament. The left side is anchored to the table while the right side is attached to a strain gauge sitting on a motorized platform.

The string used was a normal cotton string found from a conference nametag, with a diameter of 2.0mm and a mass of approximately 0.05g. The experimental setup, combined with the string properties, allows for identification of every necessasry variable in the mathematical models.

4.2.3.2 String vibrations in air

The string was found to vibrate with clear vibrations at 182 Hz. Even in air the fringes are clear and stable, Fig. 77, and contains vibration paths expected of the fundamental mode once unwrapped, Fig. 78. Only the fundamental mode was located, but modification of the tension through the motorized stage did alter the frequency at which the vibration was measured, Fig. 79.

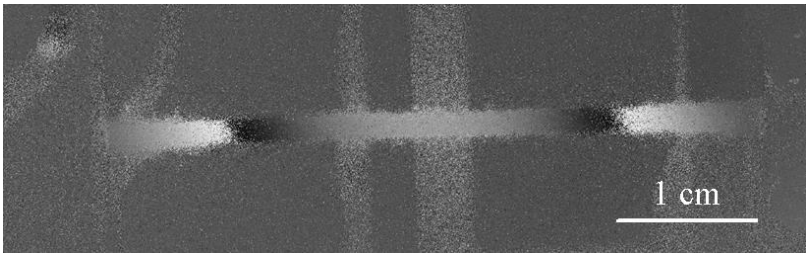

Fig. 77 Double exposure image of the string vibrating at its fundamental frequency. Fringes shown are clear and stable.

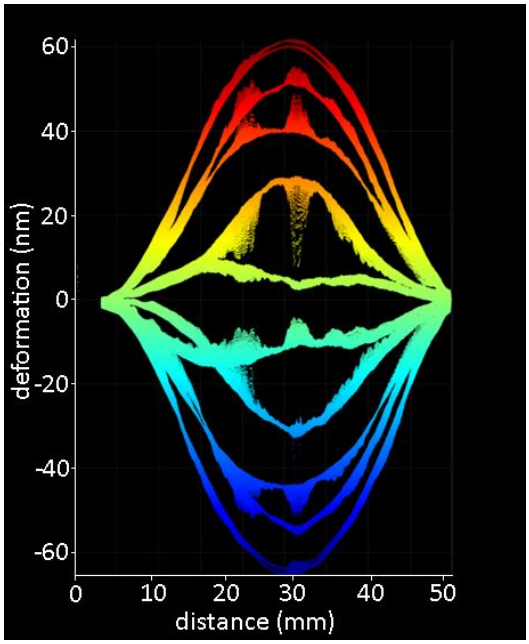

Fig. 78 Composite of string shape at multiple times in the vibration cycle of the fundamental mode. Deformations are on the nanometer scale so the *z*-axis is at 100000x scale for visibility.

By creating a normal stress-strain curve it was estimated that the string has a modulus around 3 MPa. This should be able to predict the likely frequencies of vibration or the modulus with Eq. 37. The modulus estimation predicted by this is 20 Pa, which is far lower than the 3 MPa value found experimentally. The frequency value predicted by this is 109 kHz. Both of these estimations are well off of reasonable values as well as experimentally inconsistent. The string presented a vibration of 176 Hz, at which point fringes displayed a vibration pattern as seen in Fig.

77, which is the fundamental mode of vibration, when the motor and force sensor bother were zeroed. At this point, mathematically, there was zero strain or stress which would result in no vibration. Clearly the equations must thus be modified to account for the natural tension within the string and those created by gravity. Lastly it is possible that the measured stiffness was actually a measure of friction within the threads of the string. As the string stretched the diameter decreased by a significant portion. This either suggests a large Poisson's ratio or that the effective density of the string is changing, and the components are rearranging rather than actually stretching out, which further limits the use of the equations.

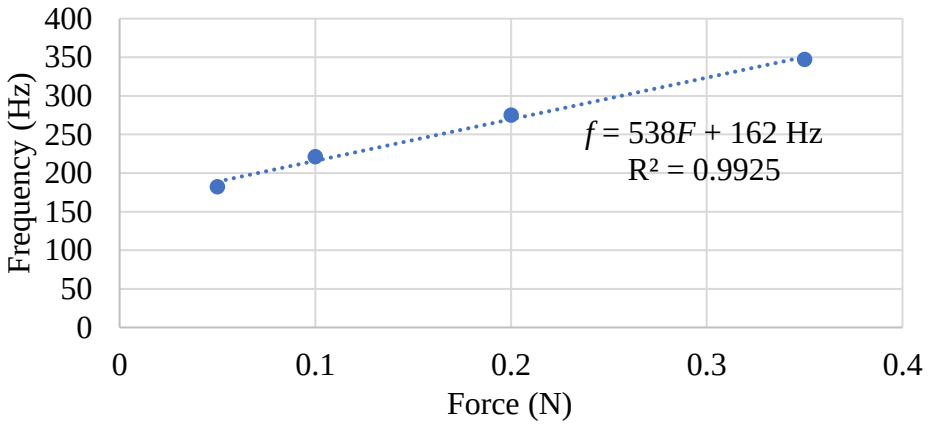

Fig. 79 Change in frequency of string vibration according to tension (0 - 101 kPa) and strain change (0 - 0.05) as measured by DHV.

4.2.3.3 String vibrations in water

Similar to Apligraf, ligaments are grown in liquid culture medium. To measure the ligament during its growth it is thus desirable to be able to measure the ligament while it is submerged in a liquid. An experiment was performed where the string had a slight tension applied manually and was submerged in water, Fig. 80. When imaged with DHV, there were some fringes and disruptions observed in the water and water container as neither were secured to the table and

thus were free to vibrate from the speaker's sound pressure. Still, fringes were observed in the string which were clearly not related to the movement of the water, Fig. 81. The fringes still need some optimization to account for the refractive disruption of the water, but this establishes that even in water the string's vibration resulting from the speaker can be measured.

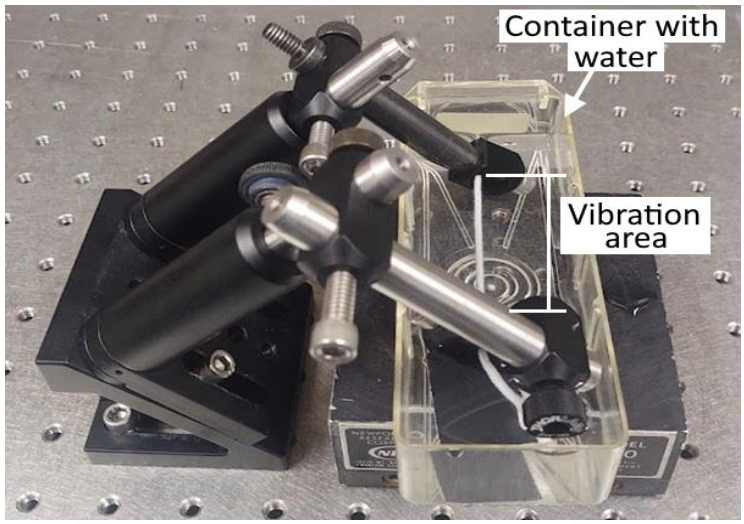

Fig. 80 Reproduction of the method by which the string was held while submerged in water.

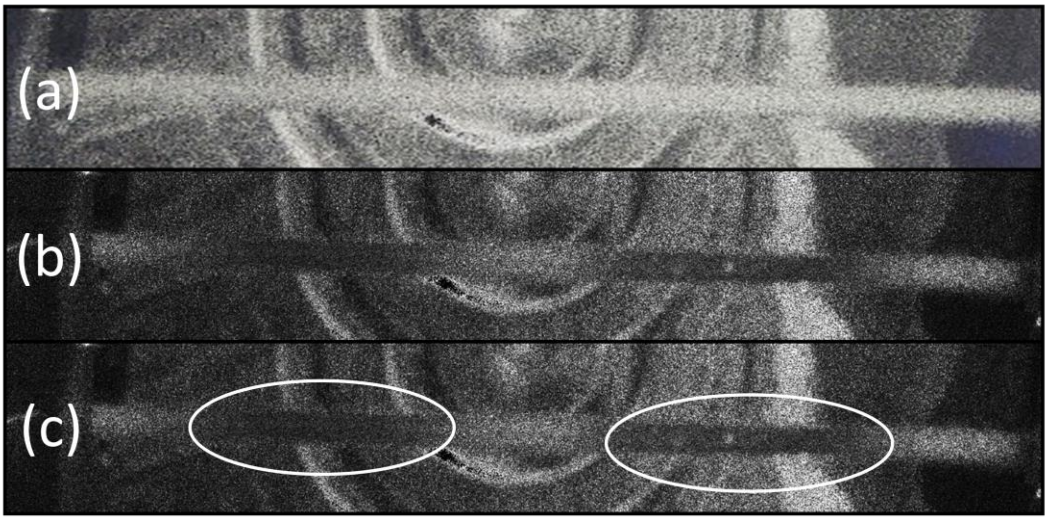

Fig. 81 Vibration of a string in water: (a) no fringes;
(b) fringes observed at frequency 176 Hz; (c) circled fringes.

4.2.4. String conclusions

Despite the problems with determining the mechanical properties of the string, there is clearly a linear relationship between the amount of force applied and the frequency of vibration, Fig. 79. The exact nature of this relation and its effect on mechanical properties must be able to be determined. Additionally, the string's vibration was stable and easy to measure. Finally, the string and the ligaments it represents are far simpler than the layered Apligraf model. It is thus appropriate to conclude that this vibrometric analysis must be capable of deriving the mechanical properties given more time. As the pressures are well below a pascal as shown in Section 3, this would remain a noninvasive method with a high promise to yield results. This study was performed on a string, but given the similarity in geometry and tension dependence between a string and a ligament, it is expected that DHV will be a successful measurement method for bioengineered ligaments.

A final experiment was performed to analyze the effectiveness of OCT with string vibration. The fundamental mode was located with DHV then the entire system was moved to a nearby OCT. Both doppler vibrometry and standard B-scan imaging did not yield any results to suggest that the string was vibrating. This is likely because the DHV measures sub-nanometer displacements in the string and the OCT used has difficulty measuring exact features below 10 microns.

5. Conclusions and recommendations

DHV holds promise as a tool in the quality control step of tissue manufacturing. It non-invasively applies a very low pressure that vibrates the tissue in ways related to the mechanical properties of the tissue. However, for a complex tissue with multiple layers and vibrating systems, such as in the case of Apligraf, the effect of the tissue on the vibration is very small compared to other more dominant features. It thus requires a significant amount of work to integrate a machine learning model and measure many samples to ascertain what the relation of properties to vibration is. Despite this long front time, once fully developed, the system holds promise to work very quickly and reliably. Furthermore, it can measure the tissues without removal from growth chambers, reducing both the labor time and disruption to the growth cycle normally necessary for quality control measurement.

The system has been shown to work well with the simpler structure of a string and shows much promise to work with ligaments. It is particularly possible with such simpler tissues that the viscoelastic response of the tissue could be determined. A dynamic force or possibly a relaxation time could be measured with a camera faster than the one used in this setup. This could provide information more in line with standard viscoelastic determination models.

It is also possible that DHV can measure product readiness without determination of mechanical properties. It may be true that certain vibrational patterns occur at different stages in the tissue's growth. In this way observation of a particular pattern could indicate product readiness, particularly for a tension dependent material such as a ligament. However, determination of this feature requires controlled experimentation on tissues throughout their growth cycle which is significantly more costly than experimenting on excess product that has already finished its growth as was used in this paper.

DHV does present several limitations. It is very quick in respect to the amount of time it takes to measure the material compared to normal measurement methods, but it is slow compared to the vibrations it is measuring. The nature of its nanoscale resolution makes it very sensitive to external vibrations and significant expense must be applied to minimizing vibrations or increasing the speed of data acquisition so that environmental vibrations do not have time to affect the measurement quality. The best way to limit the effect of this is to use a polarizing camera that can detect the necessary phase shifts at once, eliminating the temporal dependence of the measurements. DHV is also limited by the ability to identify vibrational modes. In this paper it was all conducted manually but in the future mode detection should occur automatically. The modes are not always ideal, however, and differences in the membrane, tissue, or even agar could decentralize the mode, which could complicate the identification process.

It is appropriate that the DHV system be miniaturized. If it is made to fit on a movable cart and the sensitivity to environmental vibrations is reduced, it could be easily integrated into manufacturing facilities where a larger scale of measurements could be produced. Engineers could simply roll out the system every time there was a culture media change, quickly gathering large amounts of data to be analyzed by ML algorithms to determine what the properties are. As it stands, the DHV system has a very large potential to be miniaturized and readied for fast scaled measurements.

Finally, it is recommended to tissue engineering companies in general to simplify future packaging to the greatest extent possible. Every additional layer and material complicate the measurement process, and overall simplification can increase the prospects of efficient measurement for in-line quality control.

6. Future Work

The next steps to further the current work should focus on the machine learning (ML) integration. First the algorithm training should be expanded to incorporate a wider range of data. The current training data used only a range of vales expected of the Apligraf tissue but should also incorporate values outside the expected range. For example, the modulus of the dermal layer was measured at least once with indentation to be outside of the FE simulation range, but it was believed that this was a result of the dermal layer drying, thinning, and stiffening as the indentation measurement was taken. Second, the ML algorithm should be integrated with existing data of the Apligraf tissue as it has currently only classified simulated data.

The next set of future work involves measuring actual ligaments in place of the string. It is uncertain at this moment if a FE simulation and ML integration is necessary for the model of a string or ligaments, so future work should determine if they are necessary before applying them. The FE and ML steps would be expected to take significantly less time due to the simpler structure of the ligament, however, if applied.

It is also recommended that future work integrate the DHV method with OCE. This will create the possibility for non-invasive acoustically induced optical coherence elastography of these tissues. Current exploration into this method suggests higher frequencies would be required and that modal vibration frequencies around 70-400 Hz would not produce useful elastography methods. It is questionable, however, whether this method will work as the scale of the tissue deformations from acoustic forces is still below the resolution of the OCT.

Appendices

Appendix A.

This appendix shows an exemplary set of images and the associated information paired with them as was given to the ML algorithm. Each displayed image is a single measurement taken by DHV after being unwrapped. Each row represents a full cycle of data with the first image having a phase of 0 and the 12th image having a phase of 330. Multiple rows are displayed as multiple data sets are taken to average results and ensure repeatability. The number of data sets (rows) imaged depends on the time available.

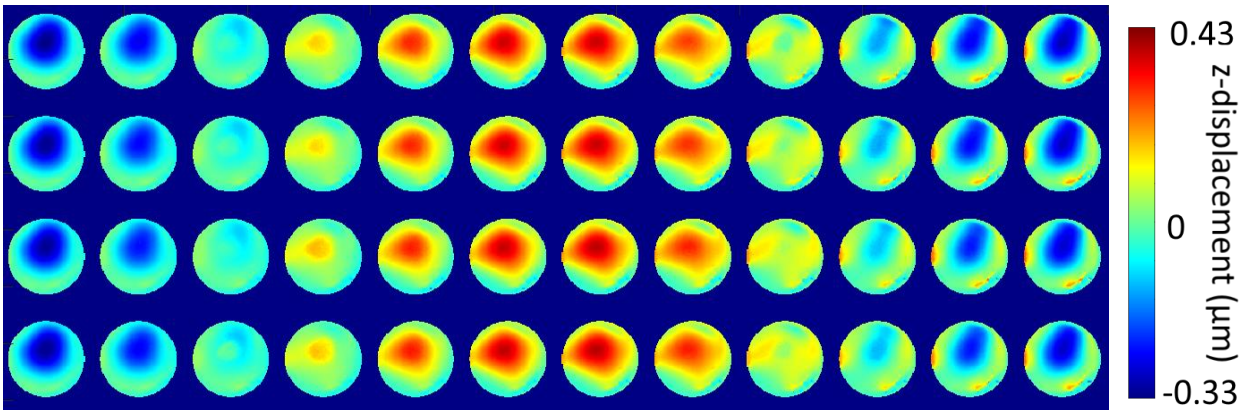

Heat-map of displacement for vibration at 167 Hz

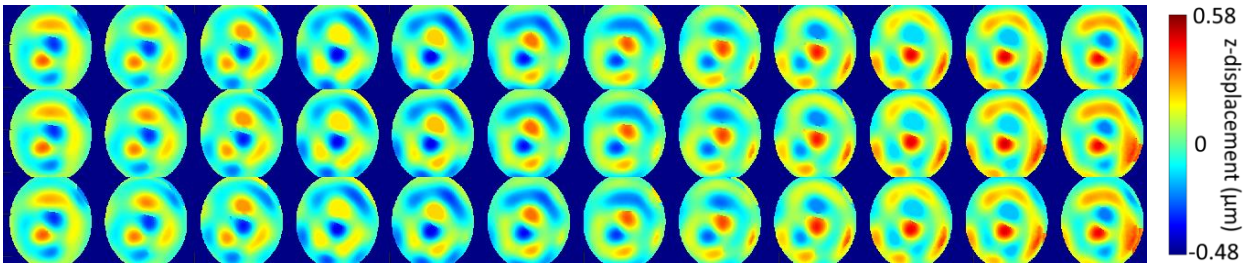

Heat-map of displacement for vibration at 248 Hz.

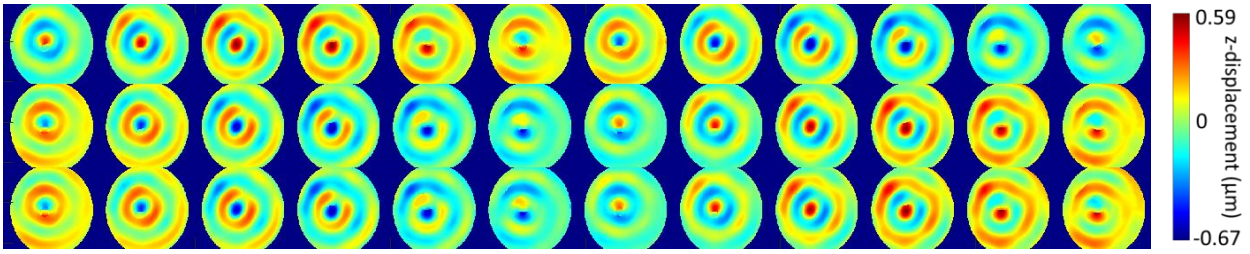

Heat-map of displacement for vibration at 284 Hz

Appendix B.

This appendix will outline the Ansys APDL script used to create the finite element simulation. APDL instruction code has been removed to leave only the elements specific to the model and simulation itself. Sections have been defined to reflect the critical component in Fig. 26 and are identified in bold. Any code text starting with an exclamation '!' is a comment that explains the commands but does not alter the APDL input.

Create Geometry

```
CYL4,0,0,0.0375
```

Element Type

```
ET,1,SHELL281
```

Lines for Boundaries

```
LDIV,2,,,9,0
LDIV,1,,,9,0
LDIV,3,,,9,0
LDIV,4,,,9,0
```

Mesh

```
MSHKEY,0
CM,_Y,AREA
ASEL,,,,    1
CM,_Y1,AREA
CHKMSH,'AREA'
CMSEL,S,_Y
!*
ESIZE,,2
!*
AMESH,_Y1
```

Set Parameter Values

```
mat1 = ii*3-2
mat2 = ii*3-1
mat3 = ii*3

!Thickness:meters
ThickEpi = 0.00005  +(.00005*(ii-1))            !range from .00005 to .0002
ThickDerm = 0.00005 +(.00005*(i2-1))   !range from .00005 to .0002
ThickPlast = 0.00002
```

```
!Modulus: Pa
ModEpi = 20000        +(5000*(i3-1))          !range from 20000 to 60000
ModDerm = 3000 +(2000*(i4-1))    !range from 3000 to 20000
ModPlast = 2300000

!Density: kg/m^3
DenEpi = 997
DenDerm = 997
DenPlast = 1000

!Poisson's Ratio
PoisEpi = 0.48
PoisDerm = 0.48
PoisPlast = 0.33

!!Agar
AgStiff = 100000
AgStiffTang = AgStiff
PinballRadius = 0.001


!*
MPTEMP,,,,,,,,
MPTEMP,1,20
MPDATA,EX,mat1,,ModPlast
MPDATA,PRXY,mat1,,PoisPlast
MPTEMP,,,,,,,,
MPTEMP,1,20
MPDATA,DENS,mat1,,DenPlast
MPTEMP,,,,,,,,
MPTEMP,1,20
MPDATA,EX,mat2,,ModDerm
MPDATA,PRXY,mat2,,PoisDerm
MPTEMP,,,,,,,,
MPTEMP,1,20
MPDATA,DENS,mat2,,DenDerm
MPTEMP,,,,,,,,
MPTEMP,1,20
MPDATA,EX,mat3,,ModEpi
MPDATA,PRXY,mat3,,PoisEpi
MPTEMP,,,,,,,,
MPTEMP,1,20
MPDATA,DENS,mat3,,DenEpi
!*

sect,1,shell,,
```

secdata, ThickPlast,mat1,0.0,3
secdata, ThickDerm,mat2,0.0,3
secdata, ThickEpi,mat3,0.0,3
secoffset,MID
seccontrol,,,,,,,

Fixed Boundaries

FLST,2,9,4,NOOR,9
FITEM,2,4
FITEM,2,9
FITEM,2,10
FITEM,2,11
FITEM,2,14
FITEM,2,15
FITEM,2,16
FITEM,2,28
FITEM,2,29
!*
/GO

DL,P51X,,UZ,0
!DL,P51X,,ROTZ,0

Elastic Support

Used as in reference [56]

Modal Analysis

MODOPT,SUBSP,60,0,1000,,OFF
RIGID,
SUBOPT,STRMCHK,0
SUBOPT,MEMORY,AUTO

Solve

Save *X* and *Y* nodal data

*get,node1,node,0,num,minD
*get,nodeL,node,0,num,maxD

*cfopen,ALLNODES%ii%,txt !###
*do,nn,node1,nodeL,1
nsel,s,node,,nn,nn
*get,x,node,nn,LOC,X
*get,y,node,nn,LOC,Y

```
*vwrite,x,y
(4F16.5)
*enddo
```

Save *Z* nodal data

```
*get,modenum,active,0,set,nset
*do,howmanyfiles,1,modenum,1
/POST1
SET,1,howmanyfiles,,0,,,, !defines data set to be read from results file !!loops through
every output data set with each set represented by the parameter ‘howmanyfiles’
ALLSEL,ALL,NODE
/OUTPUT,ZDISP_Thickness_%ThickEpi%_%ThickDerm%_Mod_%ModEpi%_%Mod
Derm%_%howmanyfiles%,txt
PRNSOL,U,Z !prints the nodal solution results
/OUTPUT
*ENDDO
```

Save frequency data

```
/POST1
/OUTPUT,FREQUENCYP_Thickness_%ThickEpi%_%ThickDerm%_Mod_%ModEpi
%_%ModDerm%_%ii%,txt
SET,LIST
/OUTPUT
```

References

[1] Savoji H., B. Godau, M. S. Hassani, M. Akbari, (2018) "Skin Tissue Substitute and Biomaterial Risk Assessment and Testing," *Front. Bioeng. Biotechnol.* https://doi.org/10.3389/fbioe.2018.00086

[2] Dahl S. L. M., C. Rhim, Y. C., Song, L. E. Niklason, (2008) "Mechanical Properties and Compositions of Tissue Engineered and Native Arteries," *Ann Biomed Eng.* 35(3):348-355

[3] https://apligraf.com/ (last accessed 23 March 2022)

[4] https://www.armiusa.org/about-us (last accessed 23 March 2022)

[5] Mao A. S., D. J. Mooney, (2015) "Regenerative medicine: Current therapies and future directions," *Proceedings of the National Academy of Sciences,* 112(47): 14452-14459

[6] Han, F., J. Wang, L. Ding, Y. Hu, W. Li, Z. Yuan, Q. Guo, C. Zhu, L. Yu, H. Wang, Z. Zhao, L. Jia, J. Li, Y. Yu, W. Zhang, G. Chu, Z. Chen, B. Li, (2020) "Tissue Engineering and Regenerative Medicine: Achievements, Future, and Sustainability in Asia," *Front. Bioeng, Biotecchnol,* https://doi.org/10.3389/fbioe.2020.00083

[7] Chan B. P., K. W. Leong, (2008) "Scaffolding in tissue engineering: general approaches and tissue-specific considerations," *Eur Spine J.* 17(Suppl 4): 467-479

[8] Vijayavenkataraman S., Z. Shuo, J. Y. J. Fuh, W. F. Lu. (2017) "Design of Three-Dimensional Scaffolds with Tunable Matrix Stiffness for Directing Stem Cell Lineage Specification: An In Silico Study," *Bioengineering*, 4(3); 66

[9] Zhu Y., Q. Zhang, S. Wang, J. Zhang, S. Fan, X. Lin, (2021) "Current Advances in the Development of Decellularized Plant Extracellular Matrix, *Front Bioeng. Biotechnol.* https://doi.org/10.3389/fbioe.2021.712262

[10] Kacarevic Z. P., P. M. Rider, S. Alkildani, S. Retnasingh, R. Smeets, O. Jung, Z. Ivanisevic, M. Barbeck, (2018) "An Introduction to 3D Biopringint: Possibilities, Challenges and Future Aspects," *Materials (Basel),* 11(11): 2199

[11] Jeong J., H. Nam, J. Jang, S. Lee. (2020) "3D Bioprinting Strategies for the Regeneration of Functional Tubular Tissues and Organs." *Bioengineering*. 7(2), 32: https://doi.org/10.3390/bioengineering7020032

[12] https://my.clevelandclinic.org/health/articles/10978-skin (last accessed 23 March 2022)

[13] Lagali, N. (2019) "Corneal Stromal Regneration: Current Status and Future Therapeutic Potential." *Current Eye Research*. DOI: 10.1080/02713683.2019.1663874

[14] Sekine W., Y. Haraguchi, T. Shimizu, A. Umezawa, T. Okano, (2011) "Thickness limitation and cell viability of multi-layered cell sheets and overcoming the diffusion limit by a porous-membrane culture insert," *J Biochip Tissue chip,* S1:007 doi:10.4172/2153-0777.S1-007

[15] Negrini N. C., N. Toffoletto, S. Fare, L. Altomare, (2020) "Plant Tissues as 3D Natural Scaffolds for Adipose, Bone and Tendon Tissue Regeneration," *Front. Bioeng. Biotechnol.* https://doi.org/10.3389/fbioe.2020.00723

[16] Shelah O., S. Wertheimer, R. Haj-Ali, A. Lesman, (2021) "Coral-Derived Collagen Fibers for Engineering Aligned Tissues," *Tissue Eng Part A.* 27(3-4):187-200

[17] Wakuda Y., S. Nishimoto, S. Suye, S. Fujita, (2018) "Native collagen hydrogel nanofibers with anisotropic structure using core-shell electrospinning," *Sci Rep,* 8, 6248

[18] Biggs L. C., C. S. Kim, Y. A. Miroshnikova, S. A. Wickstrom, (2020) "Mechanical Forces in the Skin: Roles in Tissue Architecture," *Journal of Investigative Dermatology,* 140(2):284-290

[19] Lehoux S. A. Tedgui, (1998) "Signal Transduction of Mechanical Stressing in the Vascular Wall," *Hypertension,* 32:338-345

[20] Juncosa-Melvin N., K. S. Matlin, R. W. Holdcraft, V. S. Nirmalanandhan, D. L. Butler, (2007) "Mechanical stimulation increases collagen type I and collagen type III gene expression of stem cell-collagen sponge constructs for patellar tendon repair," *Tissue Eng.* 13(6):1219-1226

[21] Lopez-Guerra E. A., A. D. Solares, (2014) "Modeling viscoelasticity through spring-dashpot models in intermittent-contact atomic force microscopy," *Beilstein J Nanotechnol.* 5:2149-2163

[22] Young, W. *Roark's Formulas for Stress & Strain*. McGraw-Hill Book Company. Sixth Edition.

[23] Grygorowicz M., E. Magnucka-Blandzi, (2016) "Mathematical modeling for dynamic stability of sandwich beam with variable mechanical properties of core," *Applied Mathematics and Mechanics,* 37: 1361-1374

[24] Royston T. J., Z. Dai, R. Chaunsali, Y. Liu, Y. Peng, R. L. Magin, (2011) "Estimating material viscoelastic properties based on surface wave measurements: A comparison of techniques and moddeling assumptions" *J Acoust Soc Am,* 130(6):4126-4138

[25] Bouchefry, K. E., S. d. Rafael. (2020) "Chapter 12 – Learning in Big Data: Introduction to Machine Learning" from Knowledge Discovery in Big Data from Astronomy and Earth Observation. *Astrogeoinformatics.* 225-249

[26] https://stanford.edu/~cpiech/cs221/handouts/kmeans.html (last accessed 24 April 2022)

[27] Xing W., and D. Du (2018) “Dropout Prediction in MOOCs: Using Deep Learning for Personalized Intervention.” *Journal of Educational Computing Research*. 57(3):547-570. doi:10.1177/0735633118757015

[28] Emmert-Streib F., Z. Yang, H. Feng, S. Tripathi, M. Dehmer. (2020) “An Introductory Review of Deep Learning for Prediction Models With Big Data.” *Front. Artif. Intell*. https://doi.org/10.3389/frai.2020.00004

[29] Saha, Sumit. (2018) “A Comprehensive Guide to Convolutioanl Neural Networks.” *Towards Data Science*. https://towardsdatascience.com/a-comprehensive-guide-to-convolutional-neural-networks-the-eli5-way-3bd2b1164a53 (last accessed 04 April 2022)

[30] Garcia-Ordas M. T., J. A. Benitez-Andrades, I. Garcia, H. A. Moreton. (2020) “Detecting respiratory pathologies using convolutional neural networks and variational autoencoders fro unbalancing data.” *Sensors*, 20.

[31] Biled, B. (2011) “Coupled viscoelastic-viscoplastic modeling of homogeneous and reinforced thermoplastic polymers.”

[32] Guillonneau G., G. Kermouche, S. Bec, J. Loubet, (2012) “Determination of mechanical properties by nanoindentation independently of indentation depth measurement,” *Journal of Materials Research*, Cambridge University Press (CUP), 27, pp.2551-2560. ff10.1557/jmr.2012.261ff. ffhal-00826308

[33] Kohn J. C., D. M. Ebenstein, (2013) “Eliminating adhesion errors in nanoindentation of compliant polymers and hydrogels,” *Journal of the Mechanical Behavior of Biomedical Materials,* 20: 316-326

[34] Utke I., J. Michler, R. Winkler, H. Plank (2020) “Mechanical Properties of 3D Nanostructures Obtained by Focused Electron/Ion Beam-Induced Deposition: A Review” *Micromachines*. 11(4):397

[35] Vahabi S., B. N. Salman, A. Javanmard, (2013) “Atomic Force Microscopy Application in Biological Research: A Review Study” *Iran J Med Sci*. 38 (2): 76-83

[36] Yu H., (2020) “Scanning acoustic microscopy for material evaluation” *Applied Microscopy*, 50, 25

[37] Akhtar R., J. K. Cruickshank, Z. Zhao, B. Derby, T. Weber, (2015), “A pilot study of scanning acoustic microscopy as a tool for measuring arterial stiffness in aortic biopsies,” *Artery Research*, 13, 1-5

[38] Yu H. (2020) “Scanning acoustic microscopy for material evaluation.” *Appl. Microsc.* 50(25)

[39] Lallemant-Dudek P., C. Vergari, G. Dubois, V. Forin, R. Vaille, W. Skalli. (2021) “Ultrasound shearwave elastography to characterize muscles of healthy and cerebral palsy children.” *Sci Rep* 11, 3577

[40] *https://pbc-society.ca/mre-magnetic-resonance-elastography/* (last accessed 04 April 2022)

[41] Kim, W., Ferguson, V.L., Borden, M., (2016) “Application of Elastography for the Noninvasive Assessment of Biomechanics in Engineered Biomaterials and Tissues,” *AB Eng*, 44(3): 705-724

[42] Ozturk A., J. R. Grajo, M. Dhyani, B. W. Anthony, A. E. Samir, (2018) “Principles of Ultrasound Elastography” *Abdom. Radiol.* 43, 773-785

[43] Aumann S., A. Donner, J. Fischer, F. Muller, (2019) “Optical Coherence Tomography (OCT): Principle and Technical Realization” *High Resolution Imaging in Microscopy and Ophythalmology*. 59-85

[44] Gabriele M. L. et al. (2011) “Optical Coherence Tomography: History, Current Status, and Laboratory Work” *Invest Ophthalmol Vis Sci*. 52(5): 2425-2436

[45] https://www.mayoclinic.org/tests-procedures/magnetic-resonance-elastography/about/pac-20385177#:~:text=Magnetic%20resonance%20elastography%20(MRE)%20is,inflammation%20in%20chronic%20liver%20disease. (last accessed 23 March 2022)

[46] Sun C., B. A. Standish, V. X. D. Yang (2011) *J. of Biomedical Optics*, 16(4)

[47] Castro-Carrion, W., (2020) “Opto-mechanical Characterization Methods to Understand Physical and Mechanical Properties of Bioengineered Tissue.” Thesis, Worcester Polytechnic Institute

[48] Tang H., P. Psota, J. J. Rosowski, C. Furlong, J. T. Cheng (2022) “Analyses of the Tympanic Membrane Impulse Response Measured with High-Speed Holography,” *Hear Res*, 410:108335

[49] https://www.engineeringtoolbox.com/sound-pressure-d_711.html (Last accessed 18 March 23)

[50] https://www.oxxius.com/products-2/advanced-features-for-lasers/ (last accessed 23 March 2022)

[51] https://www.alliedvision.com/en/camera-selector/detail/stingray/f-504/ (last accessed 23 March 2022)

[52] https://www.ni.com/en-us/shop/hardware/products/multifunction-io-device.html?modelId=124933 (last accessed 23 March 2022)

[53] https://www.tek.com/en/products/signal-generators/arbitrary-function-generator (last accessed 23 March 2022)

[54] https://www.jensentone.com/vintage-ceramic/c8r (last accessed 23 March 2022)

[55] https://www.crownaudio.com/en/products/xli-800 (last accessed 23 March 2022)

[56] Smith C. (2022) GoldsteinUnwrap2D_r1, (https://www.mathworks.com/matlabcentral/fileexchange/29497-goldsteinunwrap2d_r1), MATLAB

[57] https://www.thorlabs.com/thorproduct.cfm?partnumber=TEL321 (last accessed 23 March 2022)

[58] https://www.optics11life.com/products/chiaro-nanoindenter/ (last accessed 23 March 2022)

[59] Efremov Y. M., D. V. Bagrov, M. P.l Kirpichnikov, K. V. Shaitan. (2015) "Application of the Johnson-Kendall-Roberts model in AFM-based mechanical measurements on cells and gel." *Colloids and Surfaces B: Biointerfaces*. 134; 131-139

[60] https://www.liquidinstruments.com/product/mokulab/?utm_term=mokulab&utm_source=adwords&utm_medium=ppc&utm_campaign=Google_Search_Brand_Product_Alpha&hsa_net=adwords&hsa_grp=131882574882&hsa_mt=e&hsa_tgt=kwd-1464926001509&hsa_kw=mokulab&hsa_src=g&hsa_acc=3915257392&hsa_cam=15390021528&hsa_ver=3&hsa_ad=570981755446&gclid=CjwKCAjwrqqSBhBbEiwAlQeqGnmtVBi6eoaha-T_NgKaaQRuQTcuk9gdSSG9qjQJl_olHQZtH_M2jhoCjuQQAvD_BwE (last accessed 04 April 2022)

[61] Kuppers et al. (2006) "Dynamic characterization of AFM probes by laser Doppler vibrometry and stroboscopic holographic methods," DPIE digital library.

[62] Chopade, J. (2013) "Free Vibration Analysis of Fixed Free Beam with Theoretical and Numerical Approach Method," *IJIET* 2:1

[63] Granta EduPack 2021 R2- [Metal Universe:\Metals and alloys]Non-ferrous], Aluminum alloys (last accessed 19 March 2022)

[64] https://www.polytec.com/us/vibrometry/products/single-point-vibrometers/vibroflex (last accessed 23 March 2022)

[65] https://apligraf.com/ (last accessed 20 March 2022)

[66] Curran, M., Plosker, G., (2002) "Bilayered Bioengineered Skin Substitute (Apligraf ®) A review of its Use in the Treatment of Venous Leg Ulcers and Diabetic Foot Ulcers," ADE

[67] https://apligraf.com/apligraf-overview/ (last accessed 20 March 2022)

[68] Bauer, H. and Eidel, W., (2004) “Approximate Natural Frequencies of Circular Plates with Mixed Boundary Conditions” Forschungsbericht: LRT-WE-9-FB-1

[69] Leissa. (1969), *Vibration of Plates*. NASA SP-160. Office of Technology Utilization. Library of Congress Catalog Card Number 67-62660

[70] Li, C., Guan, G., Reif, R., Huang, Z., Wang, R., (2012) “Determining elastic properties of skin by measuring surface waves from an impulse mechanical stimulus using phase-sensitive optical coherence tomography” *J of RS,* 9(70): 831-841

[71] Yu Shann-Chewn and Huang Shyh-Chin (2001) “Vibration of a three-layered viscoelastic sandwich circular plate,” *International Journal of Mechanical Science,* 43, 2215-2236

[72] https://simutechgroup.com/normal-and-tangential-elastic-foundations-in-mechanical (last accessed 22 March 2006)

[73] https://www.thermofisher.com/order/catalog/product/14190144 (last accessed 24 April 2022)

[74] https://www.fishersci.com/shop/products/fisher-scientific-isotemp-general-purpose-heating-drying-ovens/p-4935382#?keyword=isotemp

[75] Qi, Charles R., et al. (2017) “Proceedings of the IEEE conference on computer vision and pattern recognition”

[76] Zheng, Y., X. Chen, A. Yao, H. Lin, Y. Shen, Y. Zhu, M. Lu, T. Wang, S. Chen. (2013) “Shear wave propagation in soft tissue and ultrasound vibrometry.” *Wave Propagation: Theories and Applications.* London: IntechOpen, DOI: 10.5772/48629

[77] Sigrist R. M. S., J. Liau, A. E. Kaffas, M. C. Chammas, J. K. Willmann. (2017) “Ultrasound Elastography: Review of Techniques and Clinical applications.” *Theranositcs*. 7(5); 1303-1329.

[78] https://www.manufacturingusa.com/institutes/biofabusa (last accessed 10 April 2022)

[79] http://hyperphysics.phy-astr.gsu.edu/hbase/Waves/string.html (last accessed 22 March 2022)

[80] https://www.thorlabs.com/thorproduct.cfm?partnumber=HFV002 (last accessed 23 March 2022)